

“Mechanics of Intermediate Filament Networks”

zur Erlangung des akademischen Grades eines
DOKTORS DER INGENIEURWISSENSCHAFTEN (Dr.-Ing.)

der Fakultät für Chemieingenieurwesen und Verfahrenstechnik des
Karlsruher Institut für Technologie (KIT)

genehmigte
DISSERTATION

von
Dipl.-Wirtschaftschem. Paul Pawelzyk
aus Schwalbach (Saar)

Referent: Prof. Dr. Norbert Willenbacher

Korreferent: Prof. Dr. Harald Herrmann-Lerdon

Tag der mündlichen Prüfung: 7. März 2014

Acknowledgements

First and foremost, I would like to thank Prof. Dr. Norbert Willenbacher. He not just gave me the financial support and the freedom to realize my ideas but was also a role model far beyond the scientific work. It was a pleasure to work in the open, international, and inspiring atmosphere he created in his group.

I also deeply acknowledge my co-referee Prof. Dr. Harald Herrmann. He had the idea for the project and motivated me to discover the interesting and complex world of intermediate filaments. His enthusiasm and the collaborations promoted by him were a personal gain and pushed me personally as well as the project in a very positive direction. I wish to express my thanks to Dr. Norbert Mücke. The discussions with him, his thorough corrections and his critical comments helped to improve the scientific value of this work significantly. My gratitude is also going to Tanja Tourgaidis and Monika Mauermann for teaching me different biochemical techniques and the steady supply with proteins.

I really appreciate the support of Ines Martin, Paul Walther and the staff at the electron micrograph facility at the University of Ulm for taking the scanning electron micrographs of my samples.

I acknowledge Dr. Claude Oelschlaeger for many helpful discussions, his supervision in microrheology, and as co-adviser of Frank Bossler. Frank Bossler deserves sincere acknowledgement for his tireless efforts to tackle the filament gels in extensional flow.

Many thanks are going to my internship student Magda L. Toledo. Her independent way of work made it possible to realize my ideas on a completely different field of research.

Prof. Dr. Nienhaus, Per Niklas Hedde, and Stefan Winheim are acknowledged because of their help in the preliminary experiments to image the samples using fluorescence microscopy.

I deeply appreciate Dr. Erin Koos for corrections and her help in using MatLAB, Illustrator, or LaTeX. My thanks are also going to my friend Frank Feinauer for the correction of this thesis. Last but not least, I would express my thanks to all my colleagues for the good, collaborative, and creative atmosphere as well as for all the fun in the breaks or after work.

1	Introduction.....	1
1.1	The cytoskeleton.....	1
1.2	Intermediate filaments.....	4
1.3	Mechanics of cytoskeletal filament networks.....	7
1.4	Aims and scope of this thesis.....	13
2	Polymer dynamics.....	16
2.1	Single polymer conformation.....	16
2.2	Relaxation behavior of polymer networks.....	18
2.3	Scaling of the plateau modulus.....	21
2.4	Swelling of polymer gels.....	24
2.5	Theories for the non-linear network response.....	27
3	Materials and methods.....	32
3.1	Materials.....	32
3.2	Protein preparation.....	33
3.3	Measurement of the protein concentration.....	33
3.4	SDS polyacrylamide gel electrophoresis.....	34
3.5	<i>In vitro</i> assembly of intermediate filaments.....	35
3.6	Electron microscopy.....	36
3.7	Sedimentation assay.....	37
3.8	Rotational shear rheometry.....	37
	3.8.1 <i>Linear oscillatory rheology</i>	37
	3.8.2 <i>Non-linear rheology</i>	40
3.9	Oscillatory squeeze flow.....	41
3.10	Microrheology.....	42
	3.10.1 <i>Particle preparation</i>	43
	3.10.2 <i>Particle tracking</i>	44
	3.10.3 <i>Diffusing wave spectroscopy</i>	46
4	Results and discussion.....	47
4.1	Network formation of K8/K18.....	47
4.2	Network architecture of K8/K18 networks.....	51

4.3	Measurement of the shear rheological properties of K8/K18 networks	57
4.3.1	<i>Influence of the measuring conditions</i>	57
4.3.2	<i>Measurement of the non-linear properties</i>	60
4.4	Viscoelastic properties of pure K8/K18 networks	70
4.4.1	<i>Results</i>	70
4.4.2	<i>Discussion</i>	79
4.5	Influence of magnesium chloride on K8/K18 networks	84
4.5.1	<i>Results</i>	84
4.5.2	<i>Discussion</i>	87
4.6	Influence of the non-ionic surfactant Triton X-100 on the viscoelastic properties of IF networks.....	89
4.6.1	<i>Results</i>	89
4.6.2	<i>Discussion</i>	99
5	Open questions and outlook	106
5.1	Influence of cross-linking agents on IF networks	106
5.2	Influence of the pH on the plateau modulus of K8/K18	107
5.3	Imaging of IF networks	108
6	Summary	110
7	Zusammenfassung	116
8	Appendix	123
8.1	Complementing experimental results	123
8.2	List of symbols and abbreviations.....	125
9	References	129
10	Curriculum Vitae	140
11	Publications	141
12	Conferences	141

1 Introduction

1.1 The cytoskeleton

The cytoskeleton is a three-dimensional network of protein filaments and associated proteins within the cytosol of cells. Unlike cells of plants, bacteria, and fungi, cells in multicellular animals, which are classified as metazoans, lack cell walls to stabilize cells and tissue. In metazoan cells the cytoskeleton provides cell morphology and functions such as mechanical stability, intracellular transport, and cell motility. Hence, the cytoskeleton has to be elastic to facilitate stability against external mechanical stresses and simultaneously highly flexible for essential cell functions such as crawling, invasion, and division. Metazoan cells contain three different types of cytoskeletal filaments: Microfilaments, microtubules, and intermediate filaments (IFs) (Fig. 1.1).

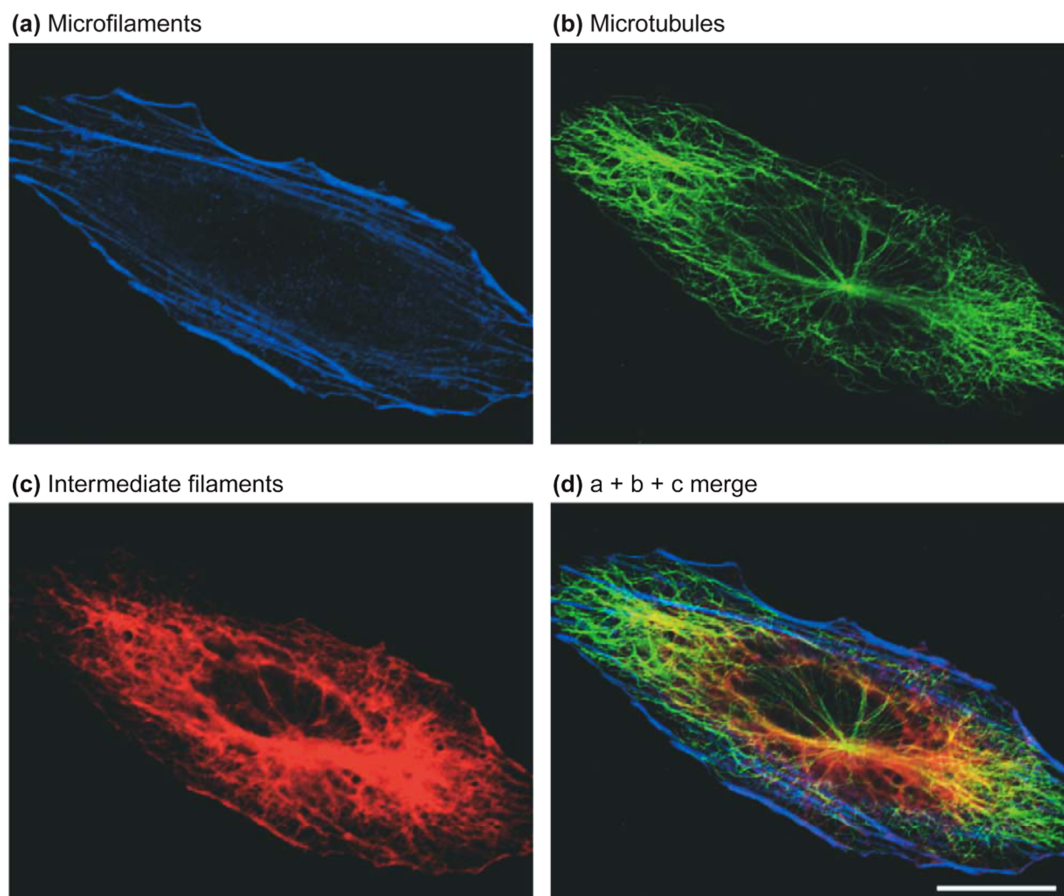


Fig. 1.1 Fluorescence image of a liver cell stained for the major parts of the cytoskeleton: a) microfilaments (blue), b) microtubule (green), and c) intermediate filaments from keratin 8 and 18 (red). The scale bar is 10 μm . Image taken from (Omary et al., 2006).

Historically the nomenclature of these protein filament families originates from the filament diameter, which can be easily distinguished on electron micrographs. Microfilaments have a diameter of 7 nm and are formed from the polar and globular protein G-actin. Filamentous actin (F-actin) is involved in cell motility and active changes of the cell shape in muscle cells. All monomers within the filaments have the same orientation. This polarity is necessary for the dynamic functions of F-actin by treadmilling, which is based on filament growth at one end and shrinkage at the other end, or as track for molecular motor proteins such as myosin. In addition to molecular motors, there are numerous other actin associated proteins such as the cross-linker proteins as α -actinin and filamin, end capping proteins, etc. (Weeds, 1982).

Microtubules consist of globular tubulin molecules, which arrange in hollow tubes with a diameter of 25 nm with a distinct polarity. All filaments originate from a central microtubules organization center (Fig. 1.2b). The main functions of microtubules are the structural organization and the intracellular transport during cell division.

Intermediate filaments have a diameter of 10 nm and consist of fibrous proteins, which belong to a family of molecules including 70 different cell-type specific members (Szeverenyi et al., 2008). This is in stark contrast to the other cytoskeletal filaments, which are formed from the evolutionary highly conserved proteins tubulin and actin. In addition, the proteins are symmetrical and lack polarity. Hence, they are not directly involved in cell motility and intracellular transport. Cytoplasmic intermediate filaments serve as mechanical stress absorber, as integrator of the cytoskeleton, and form transcellular networks through associated proteins at the cell junctions (Herrmann et al., 2007).

Defects in the cytoskeleton have been associated with many diseases including several cardiovascular diseases, neurodegenerative diseases such as Parkinson and Alzheimer, cancer, myopathies, liver cirrhosis, pulmonary fibrosis, and blistering skin diseases (Ramaekers and Bosman, 2004). Up to now 97 of these diseases have been directly associated with defects in the intermediate filament gene family (Szeverenyi et al., 2008). Among these disorders are the blistering disease epidermolysis bullosa simplex, liver-

diseases, skeletal and cardiac myopathies, neurodegenerative disorders, and cataract (Omary, 2009).

Even though intermediate filaments are the most diverse cytoskeletal protein family and involved in many diseases, most publications within the last decades concentrate on actin and microtubules (Fig. 1.2). As shown in the following, there are many unanswered questions about the properties of intermediate filaments, but the number of publications on intermediate filaments is stagnating at a level of about 550 publications per year since the end of the 1980ies. This might be due to the lower price and the improved commercial availability of kits and assays for the assembly and visualization of actin and microtubules, which facilitates research on this area and opens the area of research to experts with other backgrounds (e.g. physicists or engineers).

The project presented here was only possible because of the close collaboration with professor Herrmann's group at the German Cancer Research Center (DKFZ) in Heidelberg. Preparation, purification, and characterization of the investigated proteins were done by his group, which is leading in the field of intermediate filament research.

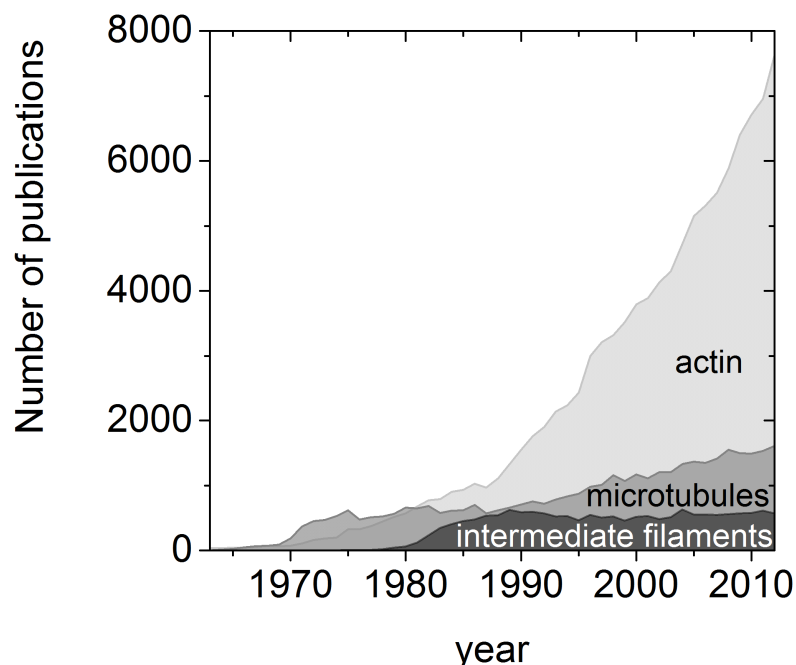


Fig. 1.2 Histogram of the publications on actin microtubules, and intermediate filaments between 1963 and 2012 (scopus, 2013).

1.2 Intermediate filaments

Intermediate filaments (IFs) are formed from a number of different proteins, which are subcategorized into five sequence homology classes (SHC) according to similarities in their protein sequence (Tab. 1).

Tab. 1 Sequence homology classes of different IF proteins.

Type (SHC)	Major representative	Distribution
I and II	Acidic and basic keratins e.g. K5/K14 and K8/K18	Epithelial cells
III	Vimentin Desmin	Mesenchymal cells Muscle cells
IV	Lamins	Nucleus of all cells
V	Neurofilaments	Neuronal cells

Keratins are the most diverse group of IF proteins. They consist of heterodimeric complexes from acidic type I and basic type II IF proteins. With respect to their biochemical function, they are distinguished as “soft” and “hard”, the former being expressed within cells and the latter constitute appendages like hair and nails. Soft keratins are found almost exclusively in epithelial cells that line external and internal surfaces of the body. According to the standard nomenclature, the acidic epithelial type I keratins are numbered 9-28, and the basic or neutral epithelial type II keratins have the numbers 1-8 and 71–80 (Schweizer et al., 2006). Intermediate filaments from keratin 5 (K5) and keratin 14 (K14) are found in the basal layer of the epidermis. Keratin 8 (K8) and keratin 18 (K18) are typical for cells in the one-layered, “simple” epithelium that lines the digestive, respiratory, and urogenital tracts. Type III IF proteins include desmin from muscle cells, the mesenchymal IF protein vimentin, and the glial fibrillary acidic protein (GFAP) found in astrocytes. The main representatives of type IV intermediate filaments are neurofilaments (NF) from neuronal cells. The lamins classified as type V are part of the nucleus. This work will concentrate on K8 and K18 two major representatives of group I and group II as well as on the type III protein vimentin.

The basic building blocks of IFs are dimeric or heterodimeric complexes, which consist of a central α -helical coiled coil interrupted by the linker L1 and L12 and non-helical head and tail domains (Fig. 1.3). The central rod domain is a common feature of the secondary structure of all IF proteins. The different IF proteins mainly vary in the amino acid sequence as well as the length of the head and the tail domains.

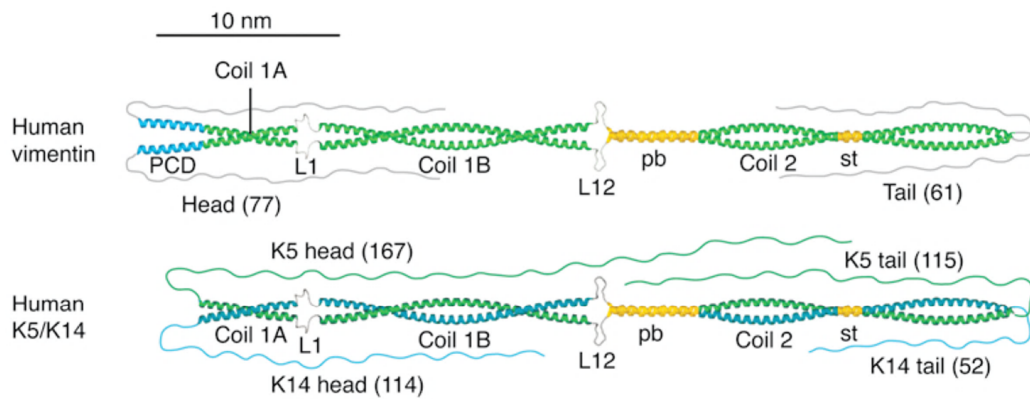


Fig. 1.3 Molecular structure of vimentin and K5/K14 (Herrmann et al., 2009).

Mutations in the genes of IF proteins, which are responsible for diseases such as the blistering disease epidermolysis bullosa simplex or heard diseases such as cardiomyopathies, are directly related to changes of the mechanical properties of the IF network (Bär et al., 2010; Ma et al., 2001). For curing of these diseases it is important to understand the underlying mechanisms. Hence, it is important to reveal in which way changes on the molecular level influence the macroscopic mechanical properties. Because of the complex, heterogeneous structures formed by IFs in many cells and because of the presence of associated “cross-bridging” proteins such as plakins, it has distinct advantages to study reconstitute networks *in vitro* (Kasza et al., 2007). This approach allows to study the structure property relationship of simplified model networks at well-defined buffer conditions using classical rheometry in order to validate the applicability of polymer network models.

The *in vitro* assembly of IFs is controlled by the pH and the ionic strength (Herrmann and Aebi, 2004). At high pH and low salt concentrations the IF proteins form soluble tetramers. These soluble complexes can be assembled into IFs by decreasing the pH or by increasing the salt concentration (Fig. 1.4). In the first step, tetramers form unit length

filaments (ULFs). The ULFs of K8/K18 consist of 6 tetramers, whereas vimentin is build up from ULFs consisting of 8 tetramers (Herrmann et al., 1999). These ULFs then anneal longitudinal to form filaments. The length of the filaments grows by head-to-head fusion between ULFs, between two filaments, or between filaments and ULFs.

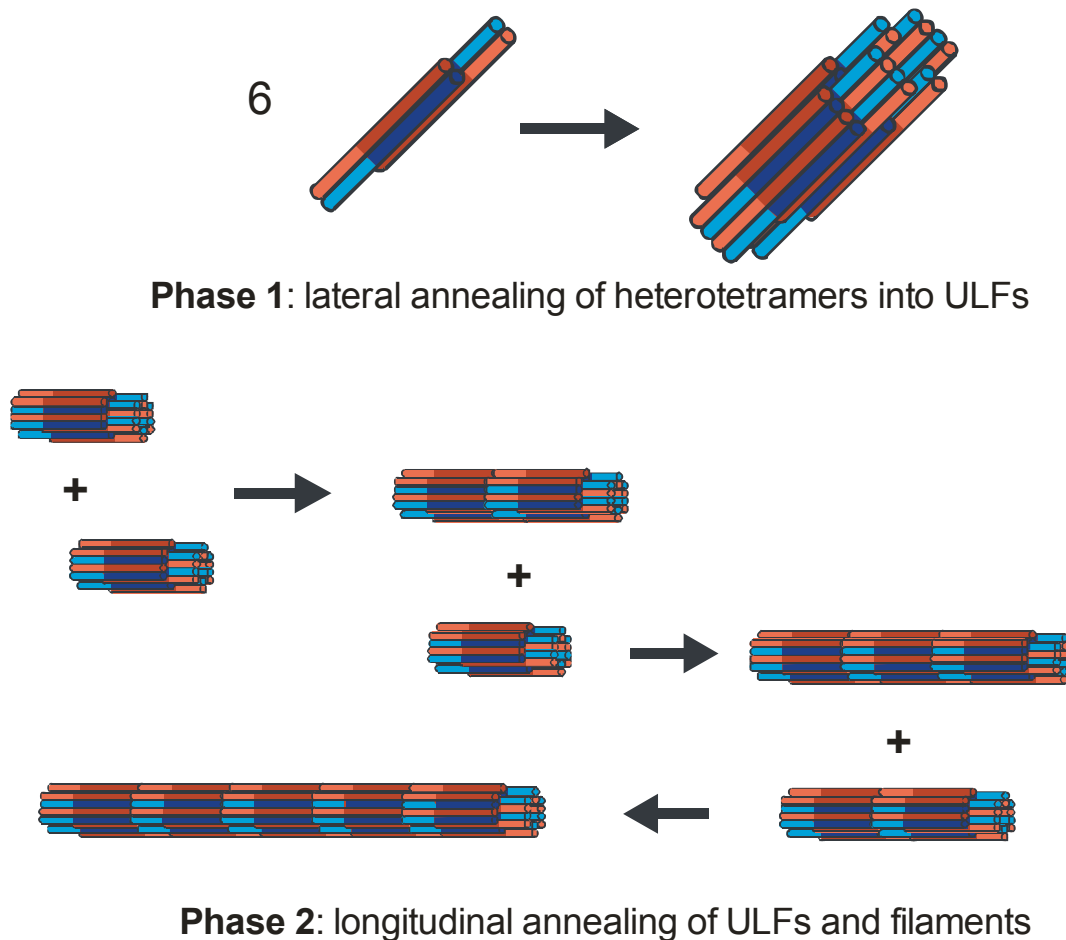


Fig. 1.4 *In vitro* assembly mechanism of keratin 8 and 18. Adapted from Kirmse et al. 2007.

The length of the filaments increases continuously. The association rate is only limited by the total number of filament ends (Portet et al., 2009). It is not possible to have exact control over network parameters such as the average filament length. The assembly kinetics of vimentin were characterized based on microscopic measurements of the length distribution of vimentin after different assembly times and for different protein concentrations (Kirmse et al., 2007). This study allowed to develop a quantitative model for filament assembly kinetics (Portet et al., 2009). A

major difference between vimentin and K8/K18 is that K8/K18 assembles more than 80 times faster than vimentin (Lichtenstern et al., 2012).

IFs start to form networks after exceeding a critical concentration, at which the filaments start to interact physically or chemically. Direct characterization of IFs on a network level by imaging methods is still difficult. Optical microscopy allows to image filaments in their natural environment. Up to now, confocal microscopy of *in vitro* IF networks is only possible at high salt concentrations at which the filaments start to form bundles (Kayser et al., 2012). Imaging of IF networks by electron microscopy has the disadvantage that the samples have to be dehydrated (Leitner et al., 2012) or frozen (Kirmse et al., 2010). Microscopy allows to characterize the length and flexibility of individual filaments as well as the network mesh size, but the interactions among IFs and the relation between filament stiffness and mesh size can only be answered by studying the mechanical properties of IF networks. Especially the non-linear mechanical response of IF networks provide physiologically important insights far beyond what simple imaging reveal. For desmin it was shown that proteins including alterations in the non- α -helical carboxy-terminal tail domain form apparently normal looking filaments in cells and *in vitro*, as revealed by electron micrographs, but strongly deviate in their mechanical properties at large stresses (Bär et al., 2010).

1.3 Mechanics of cytoskeletal filament networks

Cytoskeletal filaments, cross-linked polymers, concentrated polymer solutions or melts form cross-linked or entangled networks with mechanical properties, which are distinctly different to diluted solutions. Various models have been proposed to relate the macroscopic mechanical properties of these materials with the microstructure. The application of these models allows deriving network parameters such as the mesh size and the filament stiffness as well as the strength of the interactions among filaments or polymers. The classical theoretical concepts to describe the macroscopic mechanical properties of these networks were derived from

classical synthetic polymers (e.g. polyethylene) or elastomers (e.g. covalently cross-linked polybutadien) (de Gennes, 1979; Doi and Edwards, 1996; Treloar, 2009). A major difference between classical synthetic polymers and cytoskeletal filaments is the high stiffness, which can be characterized by the persistence length l_p . The polymer appears straight on the length scale of the persistence length. The structural and physical properties of different cytoskeletal filaments are illustrated in Fig. 1.5. The contour length characterizes the overall length of the individual polymer or filament. Depending on the ratio of the persistence length to contour length polymer molecules or protein filaments are characterized as rigid rod, semi-flexible, or flexible polymer. Microtubules behave as rigid rods because the persistence length of more than 5 mm (Gittes et al., 1993) is in most cases much larger than the contour length. F-actin is generally considered as semiflexible polymer because the persistence length of $\sim 17 \mu\text{m}$ (Gittes et al., 1993) is in the same range as the contour length. The length of the intermediate filament vimentin at a concentration of 0.1 g/l and an assembly time of 20 min ranges from 0.2 to 2 μm (Portet et al., 2009). Some authors describe intermediate filaments as semi-flexible (Lin et al., 2010b) other as flexible polymers (Käs et al., 1996). In contrast to semi-flexible polymers, flexible polymers such as polyethylene exhibit no long-range correlation between individual polymer segments. Their conformation can be described by a random walk, which results in a coil with a Gaussian distribution of polymer segments. Many physical properties of these classical polymers can be explained by the concept of self-similarity (de Gennes, 1979), i.e. each polymer chain can be divided into subunits with the same conformational properties as the complete chain.

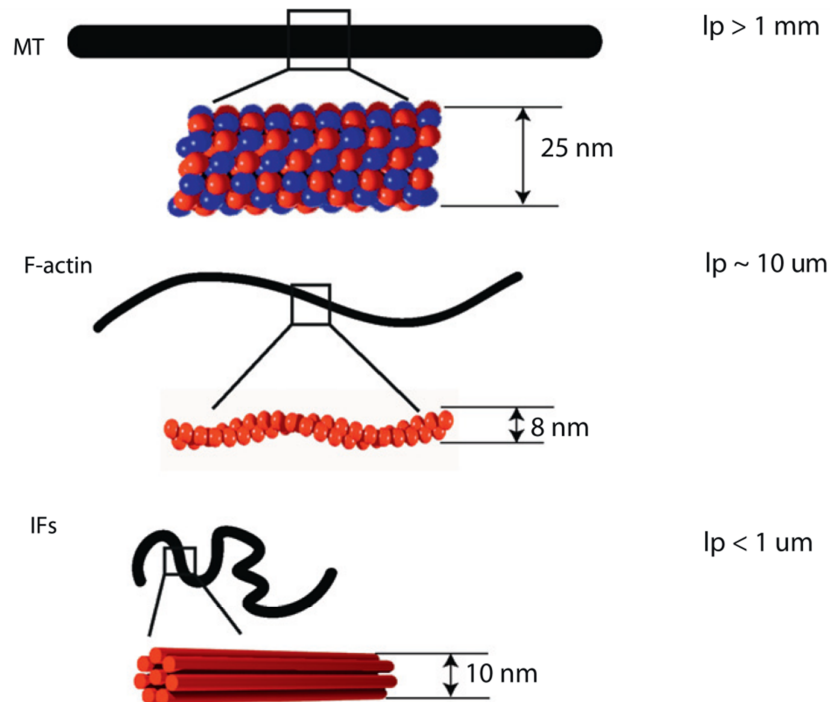


Fig. 1.5 Structure of microtubule (MT), F-actin and IFs. For comparison the contour length of $10 \text{ }\mu\text{m}$ is at the same length scale. Image taken from (Wen and Janmey, 2011).

Rheology studies the deformation and flow of these viscoelastic materials. A typical experiment is to shear a material between two parallel plates by a parallel motion of one of those plates. Such a shear deformation or strain can be created and the resulting stress response of the material can be easily detected by a rheometer. The typical shear rheological stress response of a biopolymer network in steady shear is shown in Fig. 1.6. In the linear regime the stress is proportional to the applied deformation. The network structure in the linear regime is unaffected by the macroscopic deformation. After exceeding a critical strain the stress response becomes non-linear. Generally, the slope of the stress-strain curve increases until the network ruptures at γ_{max} . This phenomenon is referred to as strain stiffening. The slope of the stress-strain curve is also termed differential modulus K . In the linear regime K equals the plateau modulus G_0 , which characterizes the elastic properties at small deformations. The increase of the differential modulus at large deformations quantifies strain stiffening of the network.

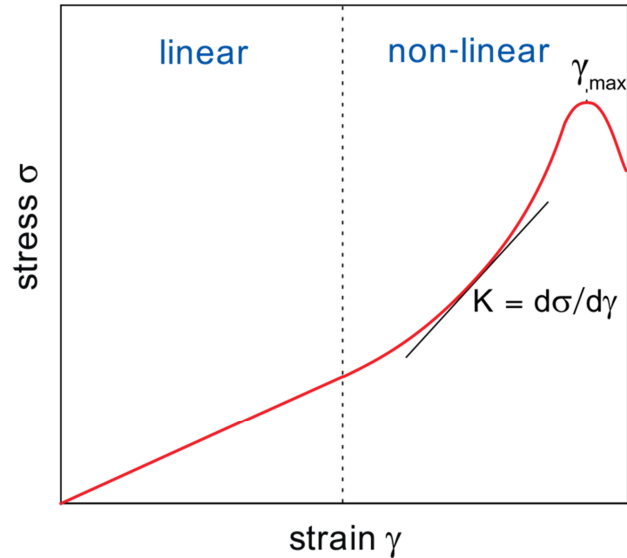


Fig. 1.6 Typical stress response of a biopolymer network. In the linear regime at small deformations the stress is proportional to the strain and K equals the plateau modulus G_0 . The increase of the slope in the non-linear regime is known as strain stiffening. The slope of the stress-strain-curve defined as the differential modulus $K = d\sigma/d\gamma$. The network ruptures at the maximum stress γ_{max} .

The scaling of G_0 with protein concentration can be described by the power law $G_0 \sim c^x$ with the characteristic scaling exponent x . Different models have been proposed to derive the x -value from the microscopic network properties. Model predictions and experimental results for different intermediate filament networks are comprised in Tab. 2. Rheological studies on neurofilaments and vimentin using high protein concentrations ($c \leq 1.5$ g/l) or in the presence of magnesium chloride agree with models for semiflexible filaments. The viscoelastic properties of K8/K18 also seem to match the theoretical predictions after treatment of the air liquid interface with phosphorlipids (Yamada et al., 2003). On the other hand many groups found scaling laws for keratins, vimentin, or desmin, with exponents much smaller than the theoretical predictions. It has been proposed that these deviations originate from bundling (Schopferer et al., 2009), direct interactions between IFs (Coulombe et al., 2000) or a strong contribution of the interfacial elasticity, which could be suppressed by phosphor lipids or other non-ionic surfactants (Yamada et al., 2003). *Up to now, there is no general explanation for the unusually weak concentration dependence of G_0 for IF networks.*

Tab. 2 Theory and experimental results for filament networks of different IF proteins for the scaling exponent x characterizing the influence of protein concentration c on the plateau modulus $G_0 \sim c^x$.

Filaments	Scaling exponent x	Reference
Theory	Ideal chains:	2.25 de Gennes 1979
	Semiflexible-chains:	
	Tube model:	1.4 Hinner et al. 1998
	Affine model:	MacKintosh et al., 1995
	Entangled filaments:	2.2
	Cross-linked rods:	2.5
K5/K14	0.5	Ma et al. 1999
K8/K18	0.25 or 1.5 after treatment with phosphorlipids	Yamada et al. 2003
Vimentin	0.5	Janmey et al. 1991; Schopferer et al. 2009; Ma et al. 1999
	1.3 and 2 with $MgCl_2$	Lin, Broedersz, et al. 2010
Desmin	0.7	Schopferer et al. 2009
NF	1.3	Rammensee et al. 2007
	2.5 with $MgCl_2$	Lin, Yao, et al. 2010

A multitude of rheological methods has been used here to characterize their linear viscoelastic properties to get a better understanding of the linear viscoelastic properties of IF networks. These methods vary in the frequency range and the length scales probed by the measurements. Macrorheological methods are based on the deformation of the bulk network by shear or by squeezing. Oscillatory shear rheometry is standard method and studies the mechanical properties by application of a well-defined oscillatory shear deformation and measurement of the resulting stress. The method is limited by the accessible frequency range due to the inertia of the rotating rheometer parts at high frequencies. Oscillatory squeeze flow, applied here using a piezo-driven axial vibrator (PAV), expands the frequency range accessible by mechanical rheometry up to 10 kHz. Microrheological

approaches rely on the thermal motion of added tracer particles. The displacement of individual tracer particles depends on their microenvironment. Multiple particle tracking (MPT) simultaneously follows the motion of up to several hundred individual tracer particles e.g. by video microscopy. This method provides information about the heterogeneity of the sample. Variation of the particle diameter allows for a direct determination of the network mesh size. The time dependence of particle motion is characterized by the mean square displacement (MSD). After a Laplace transformation the linear viscoelastic modulus can be calculated from the MSD (Mason et al., 1997). For homogeneous networks and tracer particles, which are larger than the mesh size, the viscoelastic properties from microrheological measurements should match with bulk mechanical measurements (Crocker et al., 2000; Schnurr et al., 1997). The accessible frequency range of MPT experiments is limited by the frame rate of the camera. Diffusing wave spectroscopy (DWS) is a microrheological method, which measures the temporal fluctuations of the light scattered by tracer particles (Oelschlaeger et al., 2009). From the intensity autocorrelation function of the scattered light the MSD and hence the viscoelastic moduli can be calculated (Mason and Weitz, 1995). A broad frequency range from 0.1 Hz – 10 kHz is accessible with this technique. *This is the first time that the linear viscoelastic properties of an IF network have been characterized using all these rheological methods.*

The most prominent feature of cytoskeletal protein filament networks is their non-linear stiffening behavior at large deformations or stresses (Bär et al., 2010; Janmey et al., 1991; Lin et al., 2010a, 2010b; Rammensee et al., 2007; Schopferer et al., 2009; Wagner et al., 2007). Strain stiffening is of special physiological relevance, since strain stiffening is reduced for IF mutations related to the blistering disease epidermolysis bullosa simplex (Ma et al., 2001), or severe skeletal and cardiac myopathies (Bär et al., 2010). In general, strain stiffening is a feature expected for cross-linked biopolymer networks (Storm et al., 2005). For actin filament networks it was shown that strain stiffening is tightly related to the crossbridging of filaments induced by external cross-bridging proteins (Gardel et al., 2004a; Kasza et al., 2009). IF networks exhibit strain stiffening even in the absence of external crossbridging factors such as divalent cations (Lin et

al., 2010b). Most theories about the strain stiffening behavior of protein filament networks predict the functional form of the differential modulus K (Broedersz et al., 2010a; Gardel et al., 2004a; Semmrich et al., 2007). The differential modulus can be obtained from the slope of the stress-strain curve measured at a constant strain rate (Fig. 1.6). An alternative method measures the complex differential modulus K^* by superimposing a small amplitude oscillatory shear stress and a larger steady pre-stress. Both protocols to measure the differential modulus have not been used yet to characterize networks of the IF proteins K8 and K18. This data are necessary to gain a better understanding of the interactions between these filaments and the physical origin of strain stiffening because the slope of the differential modulus is a measure for the strength of the interactions among filaments (Kroy and Glaser, 2007). The results for vimentin and neurofilaments characterized by the differential modulus measurements suggest that these filament networks behave similar as strongly cross-linked actin gels (Lin et al., 2010a, 2010b). *The origin and the strength of attractive interactions among filaments as well as the protein section contributing these attractions is still not known for IF filaments.*

1.4 Aims and scope of this thesis

There are still no general explanations for the influence of the protein concentration on the linear viscoelastic properties in terms of the plateau modulus G_0 or strain stiffening of IF networks. The aims of this thesis are:

1. The use of various macro- and microrheological methods to characterize the bending stiffness, the mesh size, and the homogeneity of K8/K18 filaments and networks. The results are compared with structural investigations of K8/K18 networks using e.g. electron microscopy.
2. The characterization of the linear and non-linear shear rheological properties of IF networks assembled from vimentin, K8/K18 as well as tailless K8 and tailless K18 (K8 Δ T/K18 Δ T) at different buffer conditions with the intention to find the origin and the strength of the proposed attractive interactions among filaments responsible for the

weak concentration dependence of G_0 and for strain stiffening. This includes the identification of the protein section contributing these attractions.

The relevant theoretical concepts for the physical properties of flexible and semi-flexible polymers and polymer networks are introduced in Chapter 2. This is important to understand the underlying assumptions behind the theories for IF networks, which will be referred to in the discussion. In addition to the existing models, a simple model for the elasticity of cubic networks of rigid filaments will be developed. Chapter 3 focuses on the used materials and methods. The experimental results will be presented and discussed in chapter 4. This main part of the thesis is subdivided into six parts.

The first part of the results and discussions (chapter 4.1) describes the kinetics of the formation of networks from the IF proteins K8 and K18 using different rheological methods. The results will be compared with previous studies about the formation of desmin and vimentin networks (Schopferer et al., 2009).

Chapter 4.2 elucidates the structure of these networks in terms of the filament diameter, the mesh size and the solubility determined by electron microscopy, multiple particle tracking and the protein solubility.

The methods used to characterize the linear and non-linear properties in oscillatory shear will be discussed in chapter 4.3. Effects of potential experimental artifacts are thoroughly examined here. This is necessary because the untypical high elasticity and the weak concentration dependency of K8/K18 networks were previously explained by a strong contribution of the interfacial elasticity (Yamada et al., 2003). In addition, there are many other artifacts in shear rheology such as wall slip or an irreversible damage of the sample during filling the sample into the rheometer. The relevance of these artifacts will be elaborated in 4.3.1 by characterizing the influence of different measuring parameters and surface treatments on the rheological properties of K8/K18 filament networks. The subchapter 4.3.2 concentrates on the method to characterize strain stiffening in the non-linear regime. The nonlinear properties of K8/K18 were already studied using standard large amplitude oscillatory shear

(Yamada et al., 2003). This study revealed no strain stiffening of K8/K18 at physiological pH values. The used method may be suited for qualitative comparison, but the interpretation of data and comparison to theories, as e.g. the glassy wormlike chain model is difficult. Methods based on an evaluation of the raw data or measurements of the differential modulus have been proposed characterizing the non-linear viscoelastic properties of biopolymer gels (Broedersz et al., 2010b; Ewoldt et al., 2008; Semmrich et al., 2008). The results of different experimental protocols to investigate the nonlinear viscoelastic network response will be compared in chapter 4.3.2.

The focus of chapters 4.4, 4.5, and 4.6 is on the linear and non-linear rheological properties of K8/K18 and how they are influenced by protein concentration, magnesium chloride concentration and the non-ionic surfactant Triton X-100, respectively. K8/K18 networks at different concentration as well as in the presence of Triton X-100 will be characterized by a multitude of rheological methods such as linear and non-linear oscillatory shear, steady shear, high frequency oscillatory squeeze flow, multiple particle tracking and diffusing wave spectroscopy. The results are the basis for a novel model describing the mechanical properties of these filament networks in the linear viscoelastic regime. High frequency measurements will be used to determine the persistence length of K8/K18 filaments as previously done for desmin and vimentin (Schopferer et al., 2009). The results for K8/K18 will be compared with IF networks from K8 Δ T/K18 Δ T and from the mesenchymal IF protein vimentin in chapter 4.6. The characterization of the non-linear mechanical properties of these IF networks provide information about the strength of the interactions among filaments and the location of the functional groups providing this strong attraction responsible for strain stiffening. Measurements on vimentin networks will be used to find out if the concepts derived from K8/K18 networks are a general feature of IF networks.

2 Polymer dynamics

2.1 Single polymer conformation

Different models have been suggested to describe the conformation of polymer molecules in solution. The *ideal chain model* (Doi and Edwards, 1996) is the simplest description for the conformation of a single polymer. The model assumes that there is no interaction between monomers and no favorable orientation. This assumption includes that two monomers can co-exist on the same place. The orientation of the individual bonds is completely random. Characteristic parameters to describe a polymer chain are the contour length of the polymer L and the end-to-end vector R between the ends of the chain. The contour length of a polymer L can be determined from the product of the number of monomers per chain N and the length of a monomer b , which results in $L = Nb$. In an ensemble of ideal chains the average end-to-end vector $\langle R \rangle$ is zero because the probability of R is the same in all directions, but the average mean square end-to-end distance $\langle R^2 \rangle$ does not vanish and is always positive. This quantity can be calculated from the scalar product of all bond vectors r_i and r_j , which describe the orientation of the individual monomers:

$$\langle R^2 \rangle = \sum_{i=1}^n \sum_{j=1}^n \langle r_i \cdot r_j \rangle = \sum_{i=1}^n \langle r_i^2 \rangle + \sum_{\substack{i,j=1 \\ i \neq j}}^n \langle r_i r_j \rangle. \quad 2.1$$

For an ideal chain only the bond vectors with $i = j$ have to be considered because there is no correlation between the individual bond vectors. Therefore, the term $\langle r_i r_j \rangle$ is zero if $i \neq j$. The length of the bond vector is equal to the monomer length b . The average end-to-end vector of an ideal chain can now be calculated by

$$\langle R^2 \rangle = \sum_{i=1}^N \langle r_i^2 \rangle = Nb^2 = bL. \quad 2.2$$

Usually flexible polymers exhibit a correlation between adjacent monomers because of a fixed bond angle and additional steric constraints by bulky side groups. These restrictions can be incorporated into the ideal

chain model by using the number of effective bonds N and an effective bond length b , which is also known as *Kuhn length*.

In so-called real chain models additional interactions among monomers far apart along the chain contour but close to each other are taken into account and this changes the fundamental relationship between N and $\langle R^2 \rangle$.

The end-to-end vector of real polymers in solution depends on the solvent quality. In a *poor solvent* the interactions between the polymers itself are preferred to polymer solvent interactions. The polymer tends to phase separate. In *good solvents*, the interactions between solvent molecules and the polymer are thermodynamically favorable. The coil starts to swell and the end-to-end distance exceeds the value predicted by the ideal chain model. The swelling is driven by an osmotic pressure on the polymer. The solvent quality is a function of temperature. The θ -*temperature* is the temperature at which the solvent quality changes from poor to good. At this temperature the energy of polymer-solvent-interactions and polymer-polymer-interactions is the same. Solvents at this characteristic temperature are also known as θ -*solvent*. The polymer chains in θ -solvents have ideal chain conformations as in polymer melts.

Protein filaments exhibit a strong limitation in the bond angle between adjacent subunits. This results in a strong correlation between adjacent segments. Such rigid polymers with small bond angles can be well described by the *wormlike chain model*, which is a special case of the ideal chain concept. The end-to-end vector of a wormlike chain can be expressed as follows:

$$\langle R^2 \rangle = 2l_p^2 (e^{-L/l_p} - 1 + L/l_p) \quad 2.3$$

with the persistence length l_p , which is a measure of the bending stiffness of the polymer. The persistence length is defined as the length at which correlations between bond vectors get lost. The ratio of the contour length to the persistence length defines whether the polymer can be described as flexible polymer, semi-flexible polymer or rigid rod. For flexible polymers with $L \gg l_p$ the end-to-end vector of a wormlike chain approaches a value of $\langle R^2 \rangle = 2l_p L$, which is equal to an ideal chain with $b = 2l_p$. If the contour length is in the same range as the persistence length, the polymer is

assigned as *semi-flexible polymer*. The end-to-end vector R is for example about 86 % of the contour length L if $l_p = L$. Polymers are defined as rigid rods if $l_p \gg L$. For rigid rods the wormlike chain model approaches a value of $\langle R^2 \rangle = L^2$.

2.2 Relaxation behavior of polymer networks

Materials such as concentrated polymer solutions, polymer melts and filament networks exhibit a characteristic relaxation behavior. The time-dependent relaxation behavior of these viscoelastic materials at small deformations can be quantified by the complex shear modulus $G^* = G' + iG''$ as a function of the angular frequency ω . The real part of the complex modulus is the storage modulus G' , which describes the elastic properties of the material. The imaginary part is called loss modulus G'' and describes the viscous material properties.

In concentrated polymer solutions or melts the polymer coils overlap and form entanglements. The relaxation behavior of these entangled systems deviate from cross-linked polymer networks at low frequencies. The characteristic relaxation behavior of entangled polymers is shown in Fig. 2.1. According to the *tube model* developed by Edwards (1967), each polymer is confined by topological constraints from surrounding chains. The surrounding polymer chains form a tube. At long time scales the polymer can move out of the tube by a movement called reptation and regain its original coiled conformation. In this so-called terminal flow regime, the viscoelastic properties are dominated by G'' and exhibit the characteristic scaling of $G' \sim \omega$ and $G'' \sim \omega^2$, which is characteristic for all viscoelastic liquids. The first cross-over at which $G' = G''$ appears at a characteristic reptation frequency ω_{rep} . The reciprocal value of this frequency is the reptation time $\tau_R = 1/\omega_{rep}$. This time characterizes the time of the polymer to diffuse out of the tube. The length of the tube is related to the average contour length of the polymer $\langle L \rangle$. With increasing polymer length ω_{rep} shifts to lower frequencies. Above ω_{rep} lateral diffusion of the polymer is limited and G' is larger than G'' . For monodisperse polymer solutions G' is getting frequency independent at this point. The frequency independent value of G' is known as the plateau modulus G_0 . The length

scale relevant in this frequency range is characterized by the average mesh size ζ or the average contour length of the polymer between cross-links or entanglements L_c . The viscoelastic properties of monodisperse entangled polymers in the plateau regime are similar to chemically cross-linked polymer networks. These networks are called gels if the ratio of G'/G'' is around 10. Permanent cross-links do not allow that the gel relaxes and the reptation time τ_R is consequently infinite. Recent considerations suggest that entangled polymers can be considered as gels even in the absence of chemical cross-links if the polymers are long, stiff and unbreakable (Raghavan and Douglas, 2012).

A second cross-over of G' and G'' is observed at entanglement frequency ω_e . Above the respective entanglement time $\tau_e = 1/\omega_e$ the time is too short for the polymer that the transverse fluctuations of the polymer can experience any confinement by entanglements or cross-links.

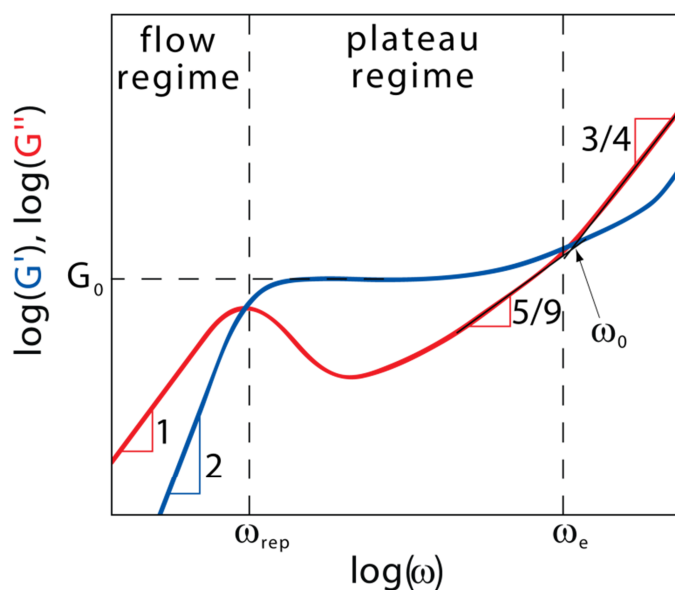


Fig. 2.1 Schematic representation of the relaxation behavior of a concentrated solution or melt of monodisperse linear polymer.

The polymer relaxation at higher frequencies is determined by the response of single filaments and short segments. First, the relaxation is dominated by Rouse-Zimm modes, which have wavelengths longer than the persistence length l_p . The Rouse model describes the polymer by a number of beads connected by springs. It considers the friction among chains and entropy elasticity but neglects hydrodynamic interactions. The Zimm model includes solvent interactions, by assuming that each chain

drags additional solvent molecules in its pervaded volume. The increase of the complex modulus in the Rouse-Zimm regime can be described by a power-law behavior of $G^* \sim \omega^a$, with exponents of $a = 1/2$ without considering hydrodynamic interactions, $a = 2/3$ for hydrodynamically interacting Gaussian chains and $a = 5/9$ for hydrodynamically interacting self-avoiding chains (Morse, 1998). At even higher frequencies the stress relaxation is determined by internal bending modes of the Kuhn segments, which are in the range of the persistence length. The complex viscoelastic modulus of semi-flexible polymers in this frequency range are dominated by viscous losses and follows a power law of $G^* \sim \omega^{3/4}$. The change in exponent from 5/9 to 3/4 occurs at the shortest Rouse-Zimm relaxation time, which is related to a critical frequency

$$\omega_0 = \frac{k_B T}{8\eta_s l_p^3}. \quad 2.4$$

Here, k_B is the Boltzmann constant, T the absolute temperature, and η_s the viscosity of the surrounding solvent (Willenbacher et al., 2007).

Gittes and MacKintosh (Gittes and MacKintosh, 1998) used a statistical approach to relate the complex modulus of the filament network at high frequencies with the length density of the filaments ρ , the friction coefficient ζ , and the bending stiffness $\kappa = k_B T l_p$:

$$G^* \approx \frac{1}{15} \rho \kappa l_p (-2i\zeta/\kappa)^{-3/4} \omega^{3/4} - i\eta_s \omega. \quad 2.5$$

According to Morse (Morse, 1998), the friction coefficient can be estimated as $\zeta \approx 2\pi\eta_s/\ln(\xi/d)$ with the filament or polymer diameter d .

The mesh size ξ and the length density ρ can easily be calculated by assuming a cubic network of rigid filaments. This assumption holds if $l_p \gtrsim \xi$. These geometric considerations result in

$$\rho = \frac{c}{\lambda_m} \quad \text{and} \quad \xi = \sqrt{\frac{3}{\rho}} \quad 2.6$$

with the polymer or filament concentration c and the mass of polymer per length unit λ_m . The mass per unit length for many protein filaments is well known. Here, the focus is on K8/K18 with a mass per length $\lambda_m = 19 \text{ kDa/nm} = 3.16 \cdot 10^{-11} \text{ g/m}$ (Herrmann et al., 1999). In contrast,

vimentin has a mass per length of $\lambda_m = 38 \text{ kDa/nm} = 6.32 \cdot 10^{-11} \text{ g/m}$ (Herrmann et al., 1999).

The persistence length l_p can be obtained from viscoelastic properties using equation 2.4 and ω_0 or alternatively from the modulus at high frequency if $G^* \sim \omega^{3/4}$ and the reduced loss modulus $G'' - \omega\eta_s$ scales linear with protein concentration using the equations 2.5 and 2.6.

2.3 Scaling of the plateau modulus

Different models have been proposed to describe the scaling of the plateau modulus G_0 with polymer concentration.

Statistical thermodynamics relates the free energy change of a system directly with the change in the degrees of freedom of the individual molecules. Each cross-link in a network reduces the conformational space of the polymer molecule. These so-called topological constraints increase the free energy of the network by $k_B T$. The plateau modulus G_0 is given by the number of constraints per volume ν , since it corresponds to the free energy density per volume:

$$G_0 = \nu k_B T. \quad 2.7$$

The *tube model* applies this fundamental physical law to entangled polymer solutions or melts. Neighboring polymers impose the same topological constraints on the polymer as a cross-link. The mesh size or tube diameter ξ is the distance between the entanglements or cross-links. The number of constraints ν is equal to the mesh size ξ^{-3} if the polymers are long and the contribution of dangling ends can be neglected. Then, the plateau modulus can be directly related to the average mesh size ξ of the network:

$$G_0 = \frac{k_B T}{\xi^3}. \quad 2.8$$

For flexible polymers the mesh size ξ is much smaller than the contour length between adjacent cross-links L_c or entanglements L_e . The polymer fraction between adjacent conformational constraints itself behaves as a polymer coil. The size of the coil in a good solvent is influenced by the

osmotic pressure. The osmotic pressure causes the polymer coil to swell. An increase in the concentration of the surrounding polymer decreases the osmotic pressure, which leads to a reduction of the coil diameter. This concept results in a scaling of the mesh size with polymer concentration of $\xi = c^{-3/4}$ in semi-dilute flexible polymer solutions in good solvent (Daoud et al., 1975). Accordingly, the *classical theory for flexible polymers* predicts that the plateau modulus follows a scaling of

$$G_0 \sim c^{2.25}. \quad 2.9$$

Scaling exponents of 2.25 ± 0.25 have been confirmed experimentally for many solutions of flexible polymers (Pearson, 1987).

Hinner and colleagues adapted the tube concept to entangled networks of semi-flexible polymers to predict the scaling exponent for the plateau modulus with concentration (Hinner et al., 1998). In flexible polymers the length scale of the tube diameter and the mesh size is the same. For semi-flexible polymers the mesh size characterizing the average distance of filaments and the tube diameter describing the distance between collisions with other filaments are different (Isambert and Maggs, 1996). The *tube model for semi-flexible filaments* derives number of constraints ν from the ratio of the length density of polymer ρ and the contour length between entanglements L_e . Equation 2.7 can now be rewritten: $G_0 = k_B T \rho / L_e$. After assuming a cubic grid of filaments with $\rho \sim \xi^{-2}$ (equation 2.6) the expression results in $G_0 \sim k_B T \xi^2 L_e^{-1}$. Statistics on the conformation of semi-flexible polymers connect L_e with the tube diameter by $L_e = d^{2/3} l_p^{1/3}$ (Odijk, 1983) and the tube diameter with the mesh size $d = \xi^{6/5} l_p^{-1/5}$ (Isambert and Maggs, 1996). Combining both relations results in $G_0 \sim k_B T \xi^{-14/5} l_p^{-1/5}$ and the corresponding scaling is

$$G_0 \sim c^{1.4} \quad 2.10$$

after using the cubic model to relate ξ and c as described by equation 2.6. The tube model for semi-flexible filaments agrees well with actin data without additional cross-linking agents (Hinner et al., 1998), neurofilaments (Rammensee et al., 2007) and vimentin at concentrations above 1.5 g/l (Lin et al., 2010a).

MacKintosh and co-workers have calculated the linear viscoelastic properties in the plateau regime from the extension of the end-to-end vector of the semi-flexible polymer strands between adjacent entanglements or cross-links beyond their equilibrium value (MacKintosh et al., 1995). The model assumes an affine deformation of the network, which means that the deformation of each network strand is the same as the macroscopic deformation. The *affine model for semi-flexible filaments* describes the entropically favorable curved conformation of semi-flexible filaments by a wave function with an amplitude, which is directly connected to the bending stiffness $\kappa = k_B T l_p$ of the filament. The force-extension derived from this wave function and statistics about the number of extended filaments in simple shear results in the following expression for the plateau modulus (Lin et al., 2010a):

$$G_0 = \frac{6\rho\kappa^2}{k_B T L_c^3}. \quad 2.11$$

In addition, the model relates the critical strain γ_{crit} at which the network response becomes non-linear with the end-to-end vector in thermal equilibrium. These considerations result in a linear relationship between γ_{crit} and the contour length between adjacent cross-links or entanglements L_c :

$$\gamma_{crit} \sim \frac{k_B T L_c}{\kappa}. \quad 2.12$$

The scaling exponent for the plateau modulus with concentration depends on the network structure. For a network of rigid cross-linked filaments the concentration dependency of G_0 can be assessed by assuming that $L_c \approx \xi$ and that ξ is equal as in a cubic grid of rigid filaments (equation 2.6). These assumptions result in

$$G_0 \sim \frac{\kappa^2}{k_B T \xi^5} \sim c^{2.5}. \quad 2.13$$

For entangled filament networks MacKintosh et al. estimated L_c from the probability function of a chain to interfere with another chain, which is $L_c \sim c^{-2/5}$ (MacKintosh et al., 1995). The predicted power law for these networks is

$$G_0 \sim c^{2.2}. \quad 2.14$$

The MacKintosh model has been used to explain the properties of vimentin and neurofilament networks in the presence of divalent cations (Lin et al., 2010b) as well as cross-linked and bundled actin networks (Gardel et al., 2004a; Shin et al., 2004).

A new approach to describe the scaling of the plateau modulus quantitatively is introduced in this work. In networks of semiflexible polymers or rigid rods L_c or L_e are close to the mesh size ξ because the persistence length l_p is in same range or larger than the mesh size. In this case the mesh size can be estimated by assuming a cubic grid of rigid filaments (equation 2.6). Combining the concentration dependency in a cubic network with the classical relationship between G_0 and ξ described by equation 2.8 then results in

$$G_0 = \frac{k_B T}{3^{3/2}} \rho^{3/2} \sim c^{1.5}. \quad 2.15$$

This *cubic grid model* has not been used before in literature. The difference between this simplistic cubic grid model and the scaling exponent of 1.4 (equation 2.10) is that the model of Hinner et al. considers the deviations between L_e and ξ . However, the difference in the scaling exponent is small. In this work the applicability of the *cubic grid model* will be tested for K8/K18 intermediate filament networks.

2.4 Swelling of polymer gels

Up until this point all models describing the scaling exponent for the plateau modulus assume that the filaments are in thermal equilibrium. A prominent feature of chemically cross-linked polymer gels is that they can change their volume after treatment with an appropriate solvent. The understanding of swollen polymer gels helps to assess whether the filaments in protein filament networks can equilibrate.

Swelling of gels results in a change of the cross-link density and the polymer concentration but the length of the polymer between cross-links remains constant. This causes a thermodynamically unfavorable stretched filament conformation, which leads to an additional contribution of the polymer strands to the free energy of these networks. Different models to

describe the influence of the swelling agent on the elasticity of these gels have been suggested. In swollen gels the polymer chains are not in thermal equilibrium as in the models described above. James and Guth developed an affine model for swollen gels of chemically cross-linked flexible polymers in θ -solvents (James and Guth, 1943). Later on the theory was extended to good solvents (Obukhov et al., 1994). In a swollen gel, polymers are stretched by a factor λ . The stretching factor can be expressed by the ratio of the volume V or volume fraction $\phi = c/\rho = V_{dry}/V$ in the swollen and the initial state of the gel:

$$\lambda = \left(\frac{V}{V_0} \right)^{1/3} = \left(\frac{\phi_0}{\phi} \right)^{1/3} = \left(\frac{c_0}{c} \right)^{1/3}. \quad 2.16$$

The free energy of a stretched ideal chain can be calculated by dividing the chain into blobs with a diameter ξ_b , which contains g monomers with the length b (Fig. 2.2).

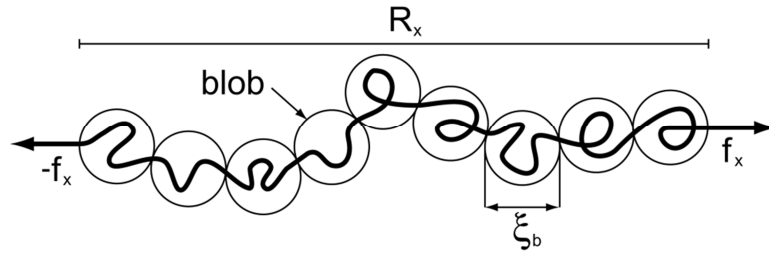


Fig. 2.2 Elongation of a chain consisting of individual blobs (de Gennes, 1979).

Each blob follows again ideal chain statistics because of the self-similarity the polymer chain:

$$\xi_b^2 \approx gb^2. \quad 2.17$$

The end-to-end distance of the whole chain containing N monomers is

$$R_x \approx \xi_b \frac{N}{g} \approx \frac{Nb^2}{\xi_b}. \quad 2.18$$

The combination of equation 2.17 and 2.18 leads to

$$\xi_b \approx \frac{Nb^2}{R_x} \text{ and } g \approx \frac{N^2 b^2}{R_x^2}. \quad 2.19$$

The blobs are forced to move in a particular direction during stretch. The degree of freedom becomes restricted and the free energy of a chain F

increases by $k_B T$ per blob. For a single stretched chain consisting of N/g blobs this results in a free energy of

$$F \approx k_B T \frac{N}{g} \approx k_B T \frac{R_x^2}{N b^2}. \quad 2.20$$

The additional elastic free energy of the stretched chain in a swollen gel can now be related to the polymer extension λ and the end-to-end distance in the preparation state R_0^2 as well as the squared end-to-end distance $R_{ref}^2 = N b^2$ expected if the strand would be a free chain in a diluted solution:

$$F \approx k_B T \frac{(\lambda R_0)^2}{R_{ref}^2}. \quad 2.21$$

In a θ -solvent the end-to-end distance in preparation state is equal to the end-to-end distance of the free chain and follows Gaussian chain statistics:

$$R_0^2 = R_{ref}^2 = N b^2. \quad 2.22$$

The elastic modulus is proportional to the elastic free energy of a chain segment between adjacent cross-links multiplied by the number constraints $G \approx \nu F$. The number of constraints is $\nu \sim c$ because the number of monomers between adjacent cross-links is constant. Combining these considerations with equation 2.21, 2.22, and 2.16 results in

$$G \approx \nu F \sim c F \sim c k_B T \lambda^2 \sim k_B T c^{1/3} c_0^{2/3} \sim c^{0.33}. \quad 2.23$$

In contrast, the end-to-end distance a free chain in a good solvent is given by $R_{ref} \sim b N^{1/2} c^{-1/8}$ (de Gennes, 1979). The use of this relationship in equation 2.21 results in

$$G \sim c F \sim c k_B T \frac{\lambda^2 R_0^2}{b^2 N c^{-1/4}} \sim c k_B T \frac{c_0^{2/3} R_0^2}{b^2 N c^{5/12}} \sim c^{7/12} \sim c^{0.58}. \quad 2.24$$

Scaling exponents close to 0.58 were found for example for swollen networks of polystyrene (Bastide et al., 1981) or polyurethane (Ilavský et al., 1989).

The scaling exponent of the elastic modulus with concentration in swollen networks containing stretched polymers is always below 0.58 whereas the exponent predicted by the theories for equilibrated polymer

networks are always above 1.4. This shows that the change in the polymer conformation due to stretching can explain very low scaling exponents. Until now, it was not considered that cytoskeletal filament networks may behave similar as swollen polymer gels.

2.5 Theories for the non-linear network response

The classical theory for rubber elasticity derives the macroscopic elasticity from an affine deformation of the individual network strands. The energy to stretch an individual chain at modest strains is $k_B T$ times the ratio of the squared end-to-end distance in the stretched state R_x^2 to the squared end-to-end distance of a Gaussian chain (equation 2.20). Then the change in free energy of n chains during an affine deformation of a three-dimensional cuboidal bloc can be expressed by the change of the average end-to-end distances of the polymers between cross-links in x , y , and z -direction after deformation and in equilibrium:

$$\Delta F \approx \frac{nk_B T}{Nb^2} [(R_x^2 + R_y^2 + R_z^2) - (R_{x0}^2 + R_{y0}^2 + R_{z0}^2)]. \quad 2.25$$

The extension of the end-to-end distance during deformation is defined by the stretch factor λ :

$$R_x = \lambda_x R_{x0}, R_y = \lambda_y R_{y0} \text{ and } R_z = \lambda_z R_{z0}. \quad 2.26$$

The average end-to-end distance in equilibrium of ideal chains follows Gaussian chain statistics:

$$R_{x0}^2 = R_{y0}^2 = R_{z0}^2 = Nb^2. \quad 2.27$$

Combining equation 2.25, 2.26, and 2.27 gives the free energy change of the network after deformation:

$$\Delta F \approx nk_B T (\lambda_x^2 + \lambda_y^2 + \lambda_z^2 - 3) \quad 2.28$$

Equation 2.28 can be used for any kind of deformation. The stretch factors in a uniaxial stretch of a rectangular block at constant volume in x -direction are given by

$$\lambda = \lambda_x \text{ and } \lambda_y = \lambda_z = 1/\sqrt{\lambda}. \quad 2.29$$

The free energy change of the network is then:

$$\Delta F \approx nk_B T \left(\lambda^2 + \frac{2}{\lambda} - 3 \right) \quad 2.30$$

The force f_x to stretch chains in a perpendicular block is the derivative of the free energy with respect to the macroscopic length in x -direction $L_x = \lambda L_{x0}$:

$$f_x = \frac{\partial \Delta F}{\partial (L_x)} = \frac{\partial \Delta F}{\partial (\lambda L_{x0})} \approx \frac{nk_B T}{L_{x0}} \left(\lambda - \frac{1}{\lambda^2} \right) \quad 2.31$$

The stress can be calculated from ratio of the force and the original cross-sectional area $L_{y0}L_{z0}$ of the rectangular bloc:

$$\sigma = \frac{f_x}{L_{y0}L_{z0}} \approx \frac{nk_B T}{L_{x0}L_{y0}L_{z0}} \left(\lambda - \frac{1}{\lambda^2} \right) = G \left(\lambda - \frac{1}{\lambda^2} \right). \quad 2.32$$

The equation shows that there is a non-linear relationship between stress and strain of entropy elastic materials consisting of ideal chains.

The force to stretch an individual ideal chain f_x is the derivative of the free energy of the chain (equation 2.20) with respect to the end-to-end vector of the extended chain R_x :

$$f_x \approx \frac{\partial F}{\partial R_x} \approx k_B T \frac{R_x}{Nb^2}. \quad 2.33$$

Hence, the correlation between the force f_x and the end-to-end distance R_x of an ideal chain is linear and obeys Hooke's law with the spring constant $k_B T / (Nb^2)$. The affine model illustrates that the force-extension of the bulk material is non-linear even though there is a linear relation between polymer extension and force at modest extensions.

At larger extensions of the polymer chain the distribution of monomers in the subsections of the stretched chains (blobs) starts to deviate from Gaussian statistics. A statistical solution for the force-extension curve of a wormlike chain has been derived (Bustamante et al., 1994):

$$f_x \approx \frac{k_b T}{l_p} \left[\frac{1}{4} \left(1 - \frac{R_x}{L} \right)^{-2} - \frac{1}{4} + \frac{R_x}{L} \right]. \quad 2.34$$

Fig. 2.3 shows the force-extension curve assuming Gaussian statistics and the force-extensions wormlike chain as well as experimental data for a

DNA molecule. The ideal chain model and the wormlike chain model agree up to an end-to-end distance of $R_x = 10 \mu\text{m}$, which is more than five times larger than the end-to-end distance of the equilibrated molecule using the parameters given in the figure capture (equation 2.3). Beyond this value the force needed for a further extension of the DNA chain increases strongly and approaches infinity as R_x approaches L .

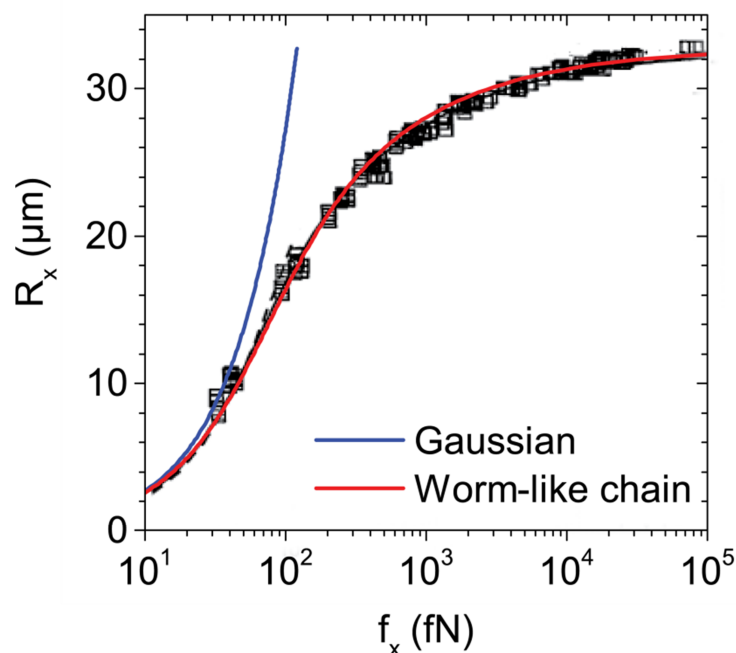


Fig. 2.3 Force-extension curve of a single DNA molecule with a contour length of $L = 32.8 \mu\text{m}$, a persistence length of $l_p = 53.4 \text{ nm}$ at a temperature of $T = 310 \text{ K}$ from experiments (Bustamante et al., 1994), for a Gaussian chain (equation 2.33) and for a wormlike chain (equation 2.34).

The non-linear force-extension curve results in a characteristic property of chemically cross-linked gels or vulcanized rubber. These materials are getting more viscoelastic when large external mechanical strains or stresses are applied. A property referred to as "strain stiffening". Strain stiffening is also a typical property of biopolymer networks (Storm et al., 2005). Different affine models for the non-linear response of biopolymer networks have been proposed (Gardel et al., 2004a; Storm et al., 2005). The underlying assumption of these models is that the filaments in these networks are cross-linked. In contrast to conventional rubber, the strain response of cytoskeletal filament networks is getting non-linear at much smaller strains (Storm et al., 2005). This characteristic results from the large persistence length of these filaments because the difference between

the maximum extension of the filament between adjacent cross-links and the equilibrated end-to-end vector is smaller than for flexible polymers.

Gardel et al. (2004) obtained a simple power law for increase of the differential modulus K with increasing stress σ from the stress-strain relation of individual wormlike chains:

$$K(\sigma) \sim \sigma^{3/2}. \quad 2.35$$

This scaling has been measured for vimentin and neurofilament networks (Lin et al., 2010a, 2010b) as well as for bundled and cross-linked actin networks (Gardel et al., 2006, 2004a).

The glassy wormlike chain model (GWLC) has been developed to describe biopolymer networks introducing reversible breakable cross-links so-called sticky contacts. A schematic representation of the interaction between filaments is shown by the asymmetric double well potential in Fig. 2.4. The bond strength of such cross-links is determined by the stickiness parameter ε . The difference in the inner energy of the bound state and the unbound state U determines the fraction of bound filaments in thermal equilibrium. To unbind or to bind a filament an energy barrier ε or $(\varepsilon - U)$ has to be overcome. The binding and unbinding dynamics are characterized by the transition rates k_- and k_+ , which are directly related to the parameters ε and $(\varepsilon - U)$.

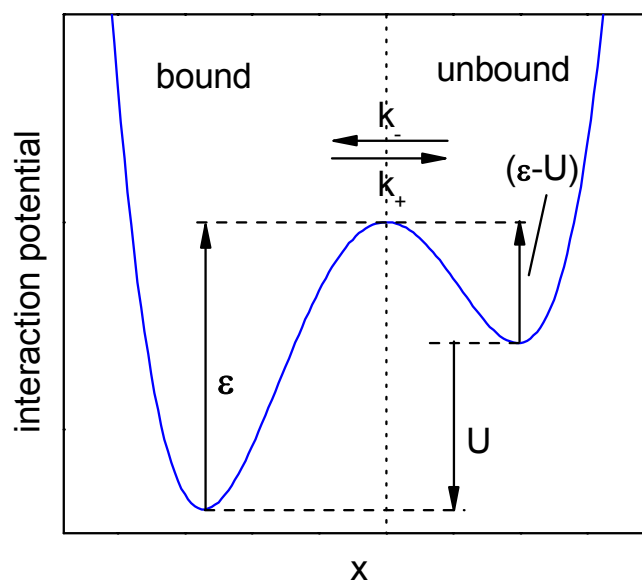


Fig. 2.4 Schematic presentation of sticky interactions among IFs. The fraction of closed bounds depends on the free energy difference U and the dynamics between the unbound and the bound state on $(\varepsilon - U)$. Adapted from (Wolff et al., 2010).

Parameter studies of the GWLC model in Fig. 2.5 show that the slope of the differential modulus as a function of deformation in the stiffening regime decreases if the stickiness parameter ε is getting smaller (Semmrich et al., 2007). The differential modulus calculated by the GWLC model results in a slope of $K(\sigma) \sim \sigma^{3/2}$ as predicted by equation 2.35 if ε approaches infinity, e.g. for covalently cross-linked networks.

The GWLC model has been used to explain the strong influence of small changes in parameters such as protein concentration, filament length, salt concentration, or temperature of actin solutions on the slope of the differential modulus (Semmrich et al., 2007).

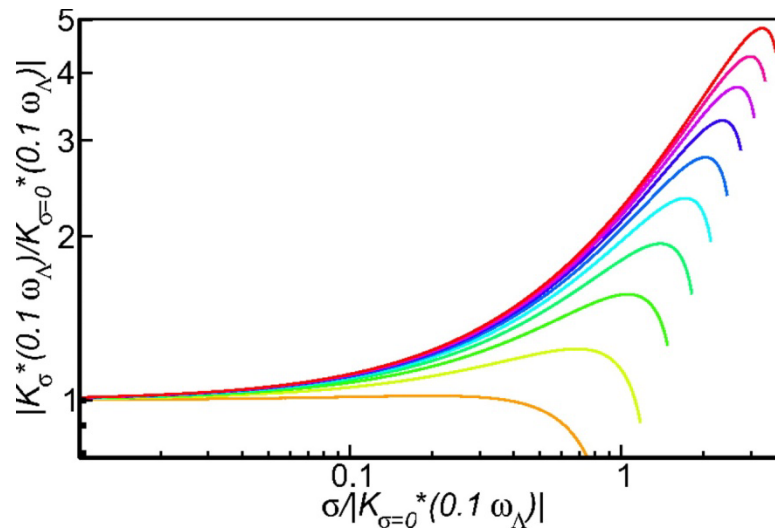


Fig. 2.5 Complex differential shear modulus K^* as function of pre-stress σ as calculated from the glassy wormlike chain model. The stickiness parameter ε increases from 4 to 40 from bottom to top. Figure taken from Semmrich et al. 2007.

3 **Materials and methods**

3.1 **Materials**

All chemicals were provided by Carl-Roth (Karlsruhe, Germany) as well as Sigma-Aldrich (Taufkirchen, Germany) and were used without any further purification. Ultrapure water, referred to as double-distilled water, was used in all experiments and was taken from the ultrapure water systems Arium pro UV (Sartorius AG, Göttingen, Germany) or Millipore Direct-Q 3 UV-R (Merck KGaA, Darmstadt, Germany). 10 M Urea solutions were freshly prepared before use. Stock solutions of 1 M 2-Amino-2-hydroxymethyl-propane-1,3-diol (Tris) and 1 M MgCl₂ were stored at room temperature. Stock solutions of 1 M Dithiothreitol (DTT) were stored in 1.5 ml aliquots at -18 °C.

For dialysis, ZelluTrans dialysis tubes (Carl-Roth) from regenerated cellulose with a molecular weight cut-off (MWCO) of 6000–8000 Da and a flat width of 10 mm were used. Traces of sulfur and heavy metals were removed before use. This was done by heating and stirring the membranes in 10 mM NaHCO₃ at 80 °C. After 30 min the tubes were transferred into a solution of 10 mM ethylenediaminetetraacetic acid (EDTA) and 40 mM NaHCO₃ and soaked for another 30 min. In the last step, the tubes were stirred in double-distilled water at 80 °C for 60 min. The cleaned tubes were then stored in a 30 % (v/v) solution of ethanol in double-distilled water at 8 °C.

Materials for gel electrophoresis such as 1x Laemmli sample buffer, 10x Tris/Glycine/SDS running buffer, Precision Plus Protein Unstained Standards and precast gels with 10 wells containing 10 % acrylamide (w/v) in a aqueous buffer solution for SDS polyacrylamide gel electrophoresis were purchased from Bio-Rad and stored as recommended by the manufacturer. 27 mg DTT (350 mM) were added to 475 µl of the purchased Laemmli sample buffer. The mixture was aliquoted and stored at -18 °C.

3.2 Protein preparation

Human K8 and K18 as well as human tailless K8 (K8 Δ T) and tailless K18 (K18 Δ T) proteins were expressed recombinantly and purified as described in Herrmann et al. (1999). The work was conducted by Tanja Tourgaidis at the German Cancer Research Center (DKFZ) in Heidelberg. The proteins dissolved in 8 M Urea, 10 mM Tris-HCl (pH 7.5) were aliquoted and stored at -80°C . To increase the protein concentration some of the protein solutions were concentrated after defrosting by centrifugal ultrafiltration for 15 min at 15.000g using Vivaspin 500 concentrators (Sartorius) with a MWCO of 10 kDa. The concentration of the individual proteins was determined by a standard Bradford assay as described below. 1:1 mixtures of the concentrated K8 and K18 were renatured by dialysis against 8 M Urea, 2 mM Tris-HCl (pH 9.0), 1 mM DTT with stepwise reduction of the urea concentration (8 M, 6 M, 4 M, 2 M) to urea-free 2 mM Tris-HCl (pH 9.0) buffer containing 1 mM DTT. The duration of each dialysis step was between 20 and 30 min. The dialysis was continued over night at 4°C in 2 mM Tris-HCl (pH 9.0) with 1 mM DTT. Vimentin was prepared recombinantly, purified, and renatured by Monika Mauermann at the DKFZ as described (Herrmann et al., 1992). The dialyzed proteins were stored at 8°C and used within one week after dialysis.

3.3 Measurement of the protein concentration

The protein concentration was determined following the Bradford method (Bradford, 1976) using a Bio-Rad protein assay. The concentration determination is based on photometry. The essential ingredient of the protein assay is a concentrate, which contains the dye Coomassie Brilliant Blue-G250. The dye has different colors depending of the amount of net charges of the dye molecule. The dye concentrate has a pH around zero, which results in positive net charge of the dye. In this regime the dye appears red and has an absorption maximum at a wavelength of 470 nm. The dye reagent concentrate was filtered using folded filters and diluted with 4 parts of double-distilled water. The pH increases and the dye's net charge neutralize. The neutral dye has a green color with an adsorption maximum at a wavelength of 650 nm. In the presence of proteins the dye

reacts with basic amino acids of the protein resulting in a negative net charge on the dye. The negatively charged dye is blue and has an absorption maximum at 595 nm. There is a linear correlation of the absorption at 595 nm and the protein concentration. The concentration can be determined by comparison of the protein absorption with a calibration curve based on a protein standard with a known concentration. The method is sensitive to very low amounts of protein ($< 0.5 \mu\text{g/ml}$). The disadvantage of this method is that the absolute value of the concentration is influenced by the amino acid sequence of the protein.

In this work, bovine serum albumin at a concentration of 1 g/l was used as standard (Aldrich). Volumes between 1 and 7 μl of the standard solution were added in 1 μl steps to 1 ml of the dye solution and mixed by inverting the tube four times to obtain the calibration curve. The protein concentration was determined by adding 1 or 2 μl of the protein solution to the Bradford dye. Each measurement is based on at least 5 independent samples. After an incubation time of 5 min the mixtures were filled into semimicro disposable polystyrene cuvettes (VWR International GmbH, Darmstadt, Germany). The absorption was measured with a photometer at a wavelength of 595 nm. The protein concentration was calculated from the calibration curve. The random error in the protein concentration is below 10 %.

3.4 SDS polyacrylamide gel electrophoresis

SDS polyacrylamide gel electrophoresis (SDS-PAGE) according to Laemmli (1970) was used to assess the impurities due to protein degradation and for the analysis of the sedimentation assay. The method separates the proteins in mixtures based on their molecular weight.

First, an equal volume of 1x Laemmli sample buffer was added to samples. The samples were heated for 5 minutes at 95 °C. The heating process and the SDS denature the proteins. The added DTT breaks existing disulfide bonds. The negatively charged SDS molecules adsorb on the proteins. The charge density of the proteins due to SDS is much stronger than the charge of the amino acids and increases with the molecular weight of the protein. The proteins can now be separated by gel electrophoresis.

Here, 30 μl of the samples containing between 1 and 5 μg of the protein as well as 10 μl of the Precision Plus Protein Standard were loaded on the precast gels. The separation was completed after 60 min at 120 V using a Mini-PROTEAN Tetra Cell for Mini Precast Gels with the PowerPac Basic Power Supply (Bio-Rad). After the separation step, the proteins on the gel were visualized by staining with the Bio-Safe Coomassie Stain. This was done by gently shaking the gel for 60 minutes in the dye solution. The dye binds to the proteins. The excess of the dye was removed in the destaining step by rinsing the gel for 60 minutes with double-distilled water.

3.5 *In vitro* assembly of intermediate filaments

The assembly of K8/K18 was started by addition of an equal volume assembly buffer (ASB) consisting of 18 mM Tris-HCl (pH 7.0) to the solution with the renatured proteins, resulting in a final buffer condition of 10 mM Tris-HCl (pH 7.4). These are the used buffer conditions used unless not otherwise stated. Assembly buffer containing additionally 1–3 mM MgCl_2 or 0.002–0.2 % Triton X-100 (w/v) were prepared for the experiments with MgCl_2 and Triton X-100. Triton X-100 is a non-ionic octylphenol ethoxylate surfactant (Fig. 3.1). The length of the ethoxylate group is 9.5 in average. The critical micelle concentration (CMC) at which the surfactant starts to form micelles is 0.014 % by weight (0.22 mM) at room temperature (Tiller et al., 1984).

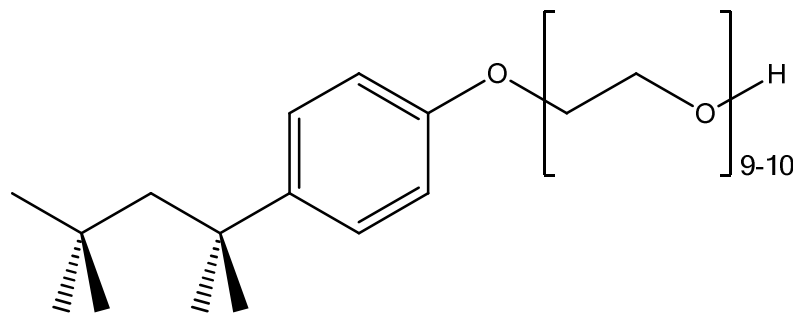


Fig. 3.1 Chemical structure of Triton X-100.

The assembly of vimentin was started by addition of 10x assembly buffer containing 1.6 M NaCl, 0.2 M Tris-HCl (pH 7.0) to obtain final concentrations of 25 mM Tris-HCl (pH 7.5) and 160 mM NaCl. The

assembly buffer for the experiments with surfactant contained additionally 1 % of Triton X-100 (w/v).

Protein solution and assembly buffer were mixed by pipette immediately after addition of the assembly buffer. Thereafter the networks were assembled *in situ* for 60 min at 20 °C. The time for addition of the assembly buffer, mixing and the transfer of the sample to the location of the measurement is about 10 seconds.

3.6 Electron microscopy

Transmission electron micrographs (TEM) were taken at the DKFZ in Heidelberg by Tanja Tourgaidis. Negative stained TEM is the standard method for imaging of intermediate filaments (Steinert et al., 1976). The stain contains heavy metal ions salts such as molybdenum, uranium, or tungsten and surrounds the filaments. The stain within the voids in between the filaments creates contrast because the heavy metal ions strongly scatter the electron beam. The result is a dark background with light-colored filaments. Sample preparation follows the procedure described by Mücke et al. (2004) and Kirmse et al. (2007). The filaments were assembled at a concentration of 0.4 g/l and diluted to 0.2 g/l by addition of assembly buffer containing 0.1 % glutaraldehyde (w/v) for fixation. Aliquots of 10 µl were absorbed for one minute on glow-discharged carbon-coated copper grids, washed with distilled water, and negatively stained with 2 % uranyl acetate (w/v). A Zeiss 900 transmission electron microscope (Carl Zeiss, Oberkochen, Germany) was used for visualization.

Scanning electron micrographs (SEM) of K8/K18 were conducted at the electron microscopy facility at the Ulm University. For SEM imaging, the keratin solutions were mixed with 2.5 µl dispersion of PS microspheres with a diameter of 1 µm (Thermo Scientific, Duke Standards) in double-distilled water at a concentration of 10 % (w/v) prior to assembly. The protein networks were assembled on a glass substrate, fixed with glutaraldehyde, critical point dried, platinum coated, and imaged as described by Leitner et al. (2012). When the three-dimensional network collapses after dehydration, the filaments settle on the glass substrate and the polystyrene beads. The networks were imaged using a secondary

electron detector. Secondary electrons are emitted from all surfaces. There is only one surface for filaments, which are attached on the glass substrate and three surfaces for filaments, which are not attached to a surface. Hence, the filaments between the beads and the glass substrate, which are not attached to a surface appear brighter and provide a good spatial impression of the network.

3.7 Sedimentation assay

The low speed sedimentation assay was used to assess the influence protein concentration of magnesium chloride concentration on the fraction of insoluble polymer. For this experiment 40 μl K8/K18 solutions were mixed with 40 μl assembly buffer by vortexing. 40 μl of the mixture were taken for control immediately after addition of the buffer. The remaining 40 μl were assembled for 60 minutes at 20 °C. After the assembly the mixture were centrifuged for 15 min at 21.380g with a table-top centrifuge (Universal 320; Hettich AG, Bäch, Swiss). The supernatant was removed by pipette and the pellet was redispersed in 40 μl double-distilled water. The control samples, the supernatants and the pellets were analyzed by SDS-PAGE.

3.8 Rotational shear rheometry

3.8.1 Linear oscillatory rheology

The macroscopic linear viscoelastic properties of the samples were measured with a stress-controlled rotational rheometer (Physica MCR 501; Anton Paar, Graz, Austria). The state-of-the-art control system of the device allows fast and accurate strain controlled measurements.

The concept of shear rheology is illustrated by the plate-plate model in Fig. 3.2a. The sample is placed between a fixed bottom plate and a moving parallel plate with the surface area A . A force F has to be applied in order to move the upper plate. The force per surface area is called shear stress σ . The deformation $\gamma = x/h$ is the ratio of the displacement of the upper plate x and the gap width between both plates h . The shear rate is the time

derivative of deformation $\dot{\gamma} = d\gamma/dt$. In rotational rheometers the sample is sheared between a fixed element and a rotating part. Stress-controlled rheometers measure the deformation angle φ of the rotating part at certain torque, which is supplied by the driving motor. The torque is directly proportional to the shear stress.

The measurement of the rheological parameters by a plate-plate geometry is shown in Fig. 3.2b. The deformation γ related to the resulting deformation angle φ is a function of the radius. This disadvantage can be avoided by using cone-plate geometries. For cone-plate geometries the gap height increases proportional to the distance from the axis and this results in a constant deformation γ . The main advantage of plate-plate geometries is that the gap width can be easily changed. In addition, the sample volume is homogeneously distributed within the gap, which ensures uniform temperature and assembly conditions.

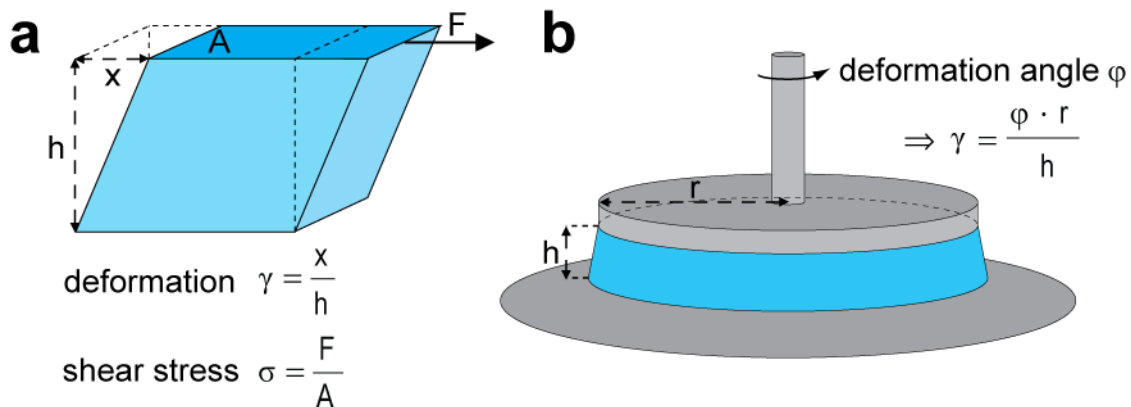


Fig. 3.2 a) Deformation γ and shear stress σ derived from the displacement x of the upper of two parallel plates with the area A by application of a force F . b) Determination of the deformation by rotational rheometry using a plate-plate geometry with the radius r and a gap width h .

Measurements in this work were performed with plate-plate geometries with diameters of 50 mm or 25 mm and a gap widths between 0.12 mm and 1.2 mm. In the following, all shear γ and shear rate $\dot{\gamma}$ data refer to the maximum value at the rim. Evaporation was minimized using a tempered hood and maintaining a moisture-saturated atmosphere. For long measurements at low gap width, the edges of the sample between the rheometer plates were additionally coated with low viscosity paraffin oil. Selected samples were characterized at a number of different plate

diameters, gap widths and surface treatments to make sure that these parameters do not influence the experimental results (chapter 4.3.1). Linear experiments with 0.01 % Triton X-100 were conducted at a gap width of 1.2 mm.

The linear oscillatory shear experiments were performed applying a sinusoidal deformation signal and measuring the stress response (Fig. 3.3). The storage modulus $G' = (\hat{\sigma}/\hat{\gamma}) \cos \delta$ and the loss modulus $G'' = (\hat{\sigma}/\hat{\gamma}) \sin \delta$ were calculated from the strain amplitude $\hat{\gamma}$, the resulting stress amplitude $\hat{\sigma}$ and the phase shift δ . The upper accessible frequency is determined by the inertia of the rheometer tools. The relative contribution of inertia to the measured signal is larger for samples with low viscosities than for samples with high viscosities. Therefore, the upper frequency limit shifts to higher frequencies for more viscous samples. The lowest accessible frequency is limited by the allowed measurement time because of structural changes of the sample e.g. due to solvent evaporation.

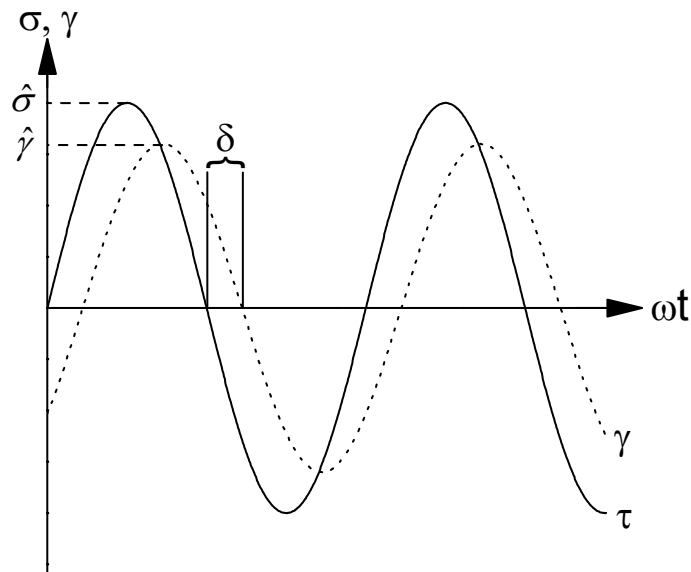


Fig. 3.3 Deformation and shear stress as function of time during an oscillatory shear experiment.

The frequency dependency of the viscoelastic properties were always measured in the linear-viscoelastic regime, which was determined in preliminary amplitude sweeps. For amplitude sweep experiments, the amplitude is increased at a constant frequency. The measured moduli are independent of the amplitude in the linear regime. The critical deformation

γ_{crit} at which the response signal becomes non-linear is defined by setting a tolerable deviation (e.g. 10 %) from linearity beforehand. Experiments were performed in the linear viscoelastic regime and the critical strain $\gamma_{crit} \lesssim 0.1$. The complex viscosity can be calculated from the moduli and the frequency: $|\eta^*| = \sqrt{G'^2 + G''^2} / \omega$. This quantity was used for the calibration of the squeeze flow device.

3.8.2 Non-linear rheology

Non-linear rheological properties were characterized by amplitude sweep experiments and differential modulus measurements. A detailed discussion of the results, the data evaluation and the advantages and limitations of the different methods will be given in chapter 4.3.2.

Amplitude sweep

Large amplitude oscillatory sweep (LAOS) experiments were conducted using a RheoScope 1 (Thermo Fisher Scientific, Karlsruhe, Germany) equipped with a cone-plate geometry (diameter 35 mm, cone angle 1°) or a MARS (Thermo Fisher Scientific, Karlsruhe, Germany) equipped with a plate-plate geometry (diameter 35 mm, gap width 0.21 mm). The stress amplitude was increased at a constant frequency of $\omega = 1$ rad/s. Each point is based on the data of a single oscillation cycle. The Lissajous figures were generated from the raw data by plotting $\gamma_{raw}(t)$ against $\sigma_{raw}(t)$. From the slope in the Lissajou plots the modulus at zero strain $G'_M = \left. \frac{d\sigma_{raw}}{d\gamma_{raw}} \right|_{\gamma_{raw}=0}$ and

the modulus at large oscillations $G'_L = \left. \frac{d\sigma_{raw}}{d\gamma_{raw}} \right|_{\gamma_{raw}=\hat{\gamma}}$ at the maximum strain $\hat{\gamma}$ were calculated (Ewoldt et al., 2008). The strain stiffening index is given by $S = G'_L / G'_M$ (Semmrich et al., 2008).

Differential modulus

The differential modulus was measured by two different protocols.

For the strain-ramp protocol the non-linear rheological properties were measured by application of a steady strain rate $\dot{\gamma} = 0.1 \text{ s}^{-1}$ and measurement of the resulting shear stress σ as a function of time, where γ is given by

$\gamma = \dot{\gamma}t$. Experiments were performed on the MARS or the Physica MCR501 rheometer using cone-plate geometry with a diameter of 35 mm and an cone angle of 1° or a plate-plate geometry with a diameter of 25 mm and a gap width of 0.12 mm, respectively. The differential modulus $K = d\sigma/d\gamma$ was calculated from the smoothed stress-strain curve using the smoothing spline or the cubic smoothing spline algorithm in MATLAB. The protocol was used especially for samples with low elasticities.

The pre-stress protocol measures the differential modulus K' by pre-stressing the sample with a steady stress σ_0 for 2 min and superposition of a small oscillatory stress $\partial\sigma \leq 0.1\sigma_0$ at $\omega = 6.3$ rad/s. The differential storage modulus $K' = (\partial\sigma_0/\partial\gamma_0) \cos \delta$ and the differential loss modulus $K'' = (\partial\sigma_0/\partial\gamma_0) \sin \delta$ were calculated from the oscillatory stress amplitude $\partial\sigma_0$, the strain amplitude $\partial\gamma_0$ and the phase shift δ of the superimposed signal. The complex differential or tangential modulus is given by $K^*(\omega, \sigma_0) = K' + iK''$. The measurements were done on the Physica MCR501 rheometer equipped with a 50 mm plate and a gap width of 0.12 mm using the standard protocol of the rheometer software. At least 10 oscillation cycles were performed for each measurement point. To probe the creep during the experiment additional creep-recovery experiments were performed at the same conditions.

3.9 Oscillatory squeeze flow

The frequencies dependency of G' and G'' between 10^1 and $3 \cdot 10^4$ rad/sec was measured by squeezing the sample at a very low deformation using a piezo-driven axial vibrator (PAV). The device illustrated in Fig. 3.4 consists of four piezo actuators and four piezo detectors, which were connected to a quadratic copper tube carrying the lower plate of the sample fixture. The cover lid defines the upper wall of the cylindrical sample fixture. Piezo actuators are driven and detectors are read out using a lock-in amplifier (SR850, Stanford Research Systems, Inc., Sunnyvale, California, USA). The PAV was built at the Institute for Dynamic Materials Testing (IdM) at the University of Ulm. G' and G'' were calculated from the phase shift and the detected voltage determined in experiments with and without sample in the measuring cell as described in Crassous et al. 2005. The

deformation of the sample during the measurements is so small that the resulting data is always in the linear viscoelastic regime. The gap can be changed by variation of the lid. Higher gap widths are more appropriate for samples with high viscosities. The exact gap width was determined from preliminary calibration with a Newtonian fluid with known viscosity. Here the silicon oil AK50 (Wacker, Burghausen, Germany) was used with a $\eta_{AK50} = 48 \text{ mPa s}$ at $25 \text{ }^\circ\text{C}$. The calibrated gap width d_{cal} was calculated as follows:

$$d_{cal} = d \cdot \left(\frac{|\eta^*|}{|\eta_{PAV}^*|} \right)^{1/3} \quad 3.1$$

with the gap d , which was set in the PAV software, and the complex viscosity of the calibration oil measured by oscillatory shear rheometry $|\eta^*|$ and by the PAV $|\eta_{PAV}^*|$.

The gap was always overfilled using a sample volume of $40 \text{ } \mu\text{l}$. The lid was attached by three screws to the bottom plate. The lid was pushed against the screw heads during the closing procedure to minimize external stress on the sample. All experiments were conducted at gap widths of 15 , 23 , and $39 \text{ } \mu\text{m}$. The results were assessed as reliable and reproducible as soon as the experiments with two different lids give the same result.

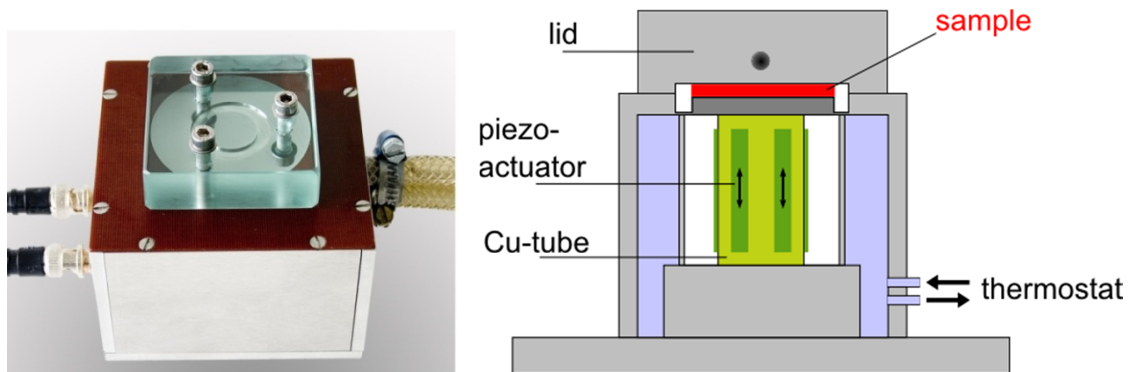


Fig. 3.4 Photo and graphical illustration of the piezo axial vibrator (Schopferer, 2010).

3.10 Microrheology

Passive microrheological methods are based on the measurement of the thermal motion of tracer particles added to the fluid to be investigated. The

motion of the particles as a function of the observation or lag time τ is characterized by the mean square displacement (MSD). The viscoelastic properties can be calculated from the MSD $\Delta x^2(\tau)$ and the tracer particle radius r applying a unilateral Laplace transformation and using the generalized Stokes-Einstein equation:

$$G^*(s) = \frac{k_B T}{\pi r s \langle \Delta x^2(s) \rangle} \quad 3.2$$

with the Laplace frequency s , the Boltzmann constant k_B , and the temperature T .

The microrheological data should agree with linear shear rheological data for homogeneous networks with a mesh size much smaller than the particle diameter and no interactions between the particles and the sample (Mason and Weitz, 1995). In order to investigate whether the particles interact with the IF networks, the results obtained by using particles with different surface functionalities were compared.

3.10.1 Particle preparation

Unfunctionalized particles were washed before use with double-distilled water. The particles were separated from the fluid by centrifugation. The supernatant was removed and the particles were redispersed in double-distilled water by vortexing. The procedure was repeated four times.

The polyethylene glycol (PEG) functionalized particles were coated according to the swelling based approach of Kim and co-workers (Kim et al., 2005). 100 μ l or 125 μ l of the particle suspensions were mixed with 1.6 ml of a Pluronic F127 (BASF) solution with a concentration of 1 % (w/w) and 10 droplets of toluene. Pluronic F127 is a triblock co-polymer of two PEG end groups and a central domain of polypropylene glycol (PPO) with the formula $\text{H}(\text{OCH}_2\text{CH}_2)_{106}(\text{OCH}(\text{CH}_3)\text{CH}_2)_{70}(\text{OCH}_2\text{CH}_2)_{106}\text{OH}$. The mixture was shaken overnight. Toluene swells the particles and allows the hydrophobic PPO block to penetrate into the particles. Toluene was removed by heating the open reaction tube to ~ 85 $^\circ\text{C}$ while shaking. The volume of the dispersion at the end of this step was always above 500 μ l. The particles were collected by centrifugation for 2 min at 8.000g and washed four times by centrifugation and redispersion in double-distilled

water. The final volume was adjusted to obtain final particle concentrations of 1 % or 10 % (w/v).

3.10.2 Particle tracking

Multiple particle tracking (MPT) is based on tracking of individual particles by optical microscopy (Mason et al., 1997) or by photodiodes (Gittes et al., 1997). For MPT experiments green fluorescent polystyrene tracer particles (Bangs Laboratories, USA) with a diameter of 0.19 μm , 0.52 μm , or 1.01 μm and different surface functionalities were used. An amount of 0.5 μl of tracer particles dispersed in dialysis buffer at a concentration of 1 % (w/v) was added to 20 μl protein solution and mixed by vortexing before addition of the assembly buffer in order to obtain a final particle concentration of 0.01 %. After addition of the assembly buffer, both solutions were mixed by pipette and filled in the self-build sample chamber, which was sealed using a UV curing optical adhesive (NOA63, Norland Optical Adhesive, USA). The average size of the sample chamber consisting of cover slips was 5 x 10 mm with a thickness of 160 μm . The thermal motion of the particles at a temperature of 20 $^{\circ}\text{C}$ was tracked with an inverted fluorescence microscope (Zeiss Axiovert 200) with C-Apochromate 40x objective and a CCD camera (Pike F100-B or Stingray F033B, Allied Vision Technologies, Stadroda, Germany) at a speed of 30 frames per second and at resolutions higher than 0.15 μm per pixel. The fluorescent particles were excited at a 470 nm wavelength using a Colibri LED illumination system (Zeiss). The particles emit light at a maximum wavelength of 520 nm. The optical resolution of the micrographs is limited by the Abbe diffraction limit $d = \lambda / (2 \text{ NA})$ with the wavelength of the emitted light λ and the numerical aperture of the used objective $\text{NA} = 1.2$. Hence, the maximum optical resolution of the microscope is ~ 220 nm. The particle diameters observed by the camera appear larger due to the scattering of the light emitted by the fluorophores. When the distance between individual particles exceeds the optical resolution limit, the position of each particle can be determined on a sub-pixel-scale by calculation of the center of the intensity distribution of the particle image (Bräuchle et al., 2009). For each measurement 5 sets of 300 s at randomly chosen positions were recorded. A measurement comprises between 37 and 135 particles. The images were filtered and analyzed by the software Image

Processing System (Viscometrics iPS). The filter process comprises smoothing using a Gaussian filter, contrast improvement with a clipping filter, and a background correction. The analysis software automatically identifies the center of mass of the single particles from the binarized images. The software Trace (Viscometrics) correlates the particle position information to generate trajectories, which reflect the paths of the moving particles. Two examples of the resulting particle trajectories are shown in Fig. 3.5. The trajectory on the left corresponds to a particle, which freely diffuses through the meshes of an IF network. In contrast, the trajectory on the right originates from a particle, which is confined by the IF network. In some cases the trajectories generated by the tracing software jump from one particle to another. These jumps were deleted manually. Only trajectories with a length of more than 100 frames were used. The MSDs, the moduli and the heterogeneity were analyzed using Enthought Microrheology Lab software (Austin, USA).



Fig. 3.5 Examples of trajectories of a particle, which freely diffuses through the meshes of the network on the left and a particle, which is trapped by surrounding filaments on the right. In both cases the length of the trajectory is 30 s. The scale bar is the same for both examples.

Errors in the absolute values of MPT experiments arise from static errors due to the exact determination of the particles position and dynamic errors due to the finite frame rate (Savin and Doyle, 2005). The static errors mainly originate from the signal to noise ratio of the setup. The error can be assessed by measuring the apparent motion of fixed particles. The software interprets the noisy signal as small particle movements and the resulting MSD appears higher than the true value. The dynamic errors arise from the uncertainty of the particle motion between two frames. This error leads to an underestimation of the MSD because the distance covered by the

particle is larger than the minimum distance between two successive particle positions used by the software.

3.10.3 Diffusing wave spectroscopy

Diffusing wave spectroscopy (DWS) measures the temporal fluctuations of the light scattered by tracer particles (Mason and Weitz, 1995). Sulfate functionalized particles with a diameter of 1.3 μm (Invitrogen Carlsbad, California, USA), which were coated with PEG as described above, were used as tracers. The coated particles were washed three times with dialysis buffer and mixed with the protein solution by vortexing prior to assembly. Immediately after addition of the assembly buffer the sample was filled into a cuvette. For the measurements 150 μl sample and cuvettes with a thickness of 1 mm (Hellma, Müllheim, Germany) were used. The final particle concentration was 1 %. The sample was illuminated with coherent laser light and the intensity fluctuations of the transmitted light due to the motion of the tracer particles were measured using a photomultiplier (Oelschlaeger et al., 2009). The intensity correlation function (ICF) obtained from the fluctuations of the scattered light is related to the MSD (Mason and Weitz, 1995). The measurements were conducted and analyzed using the DWS ResearchLab (LS Instruments, Fribourg, Swiss) with multi-tau correlator at an acquisition time of 270 s and echo duration of 5 s. The MSD can be calculated for lag times between 10^1 and 10^{-6} s with the setup used here. The MSD and G^* were calculated from the ICF of the sample and a blank measurement using the device software.

4 Results and discussion

4.1 Network formation of K8/K18

The dissolved tetrameric complexes of the IF proteins K8 and K18 start to assemble into filaments when the pH decreases from pH = 9.0 to pH = 7.4 (Hofmann and Franke, 1997). After an assembly time of 2 min a broad distribution of filaments ranging from 0.1 until 1 μm was observed for K8/K18 at concentrations ≤ 0.2 g/l (Lichtenstern et al., 2012). These filaments interfere with each other and form networks.

To determine the kinetics of the network formation, the viscoelastic properties were monitored by linear oscillatory rheology at a protein concentration of 0.5 g/l. The assembly was started by decreasing the pH by addition of an assembly buffer. Immediately after adding assembly buffer to the protein solution, both compounds were gently mixed by pipette and filled into the rheometer. The overall time from addition of the assembly buffer until recording of the first data point is completed is less than 2 minutes. During the measurement the deformation amplitude was kept in the linear viscoelastic regime at $\gamma = 1$ %. The time evolution of the storage modulus G' and the loss modulus G'' of K8/K18 at a temperature of 20 °C and at the physiological body temperature of 37 °C is shown in Fig. 4.1. The data shows that the moduli in the linear viscoelastic regime are not influenced by temperature. The qualitative evolution of the moduli at both temperatures is essentially the same as found for the assembly of desmin and vimentin (Schopferer et al., 2009). G' is larger than G'' even for the first data point taken about 1 min after closing the rheometer gap. Although the moduli quickly change in the initial period, this suggests that a network may have already existed when the gap closes. The overall increase of G' is by a factor of two during the measuring time of 60 min, but the increase gradually levels off. Even after 20 min at least 85 % of the final G' level obtained after 60 min was reached.

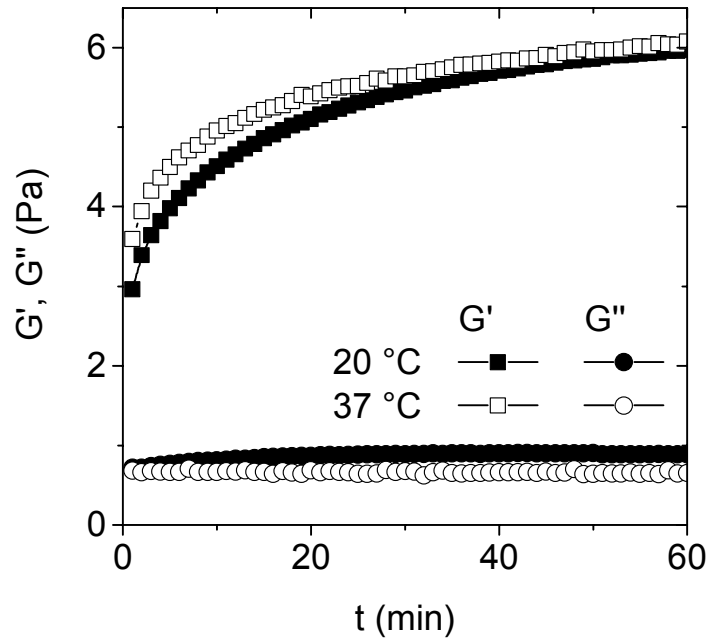


Fig. 4.1 Time evolution of G' and G'' during the assembly of 0.5 g/l K8/K18 at 20 °C and at 37 °C measured at a frequency of 1 rad/s.

In addition to the macrorheological measurements, the time evolution of the network response was followed by the microrheological methods DWS and MPT. Sample preparation and the time for the data acquisition of the first point was approximately 5 minutes for both methods. The intensity correlation function from DWS experiments in Fig. 4.2 shows that the scattering signal only changes at long lag times τ . This is due to the fact, that the longest lag time at which the intensity correlation function signal can be safely distinguished from the noise is 10^{-2} s. This corresponds to a measuring frequency of 100 rad/s. At these high frequencies the viscoelastic response is less dependent on filament length or cross-link density than at low frequencies applied in mechanical rheometry. The measured signal at these short lag times τ is approximately time independent after 20 min.

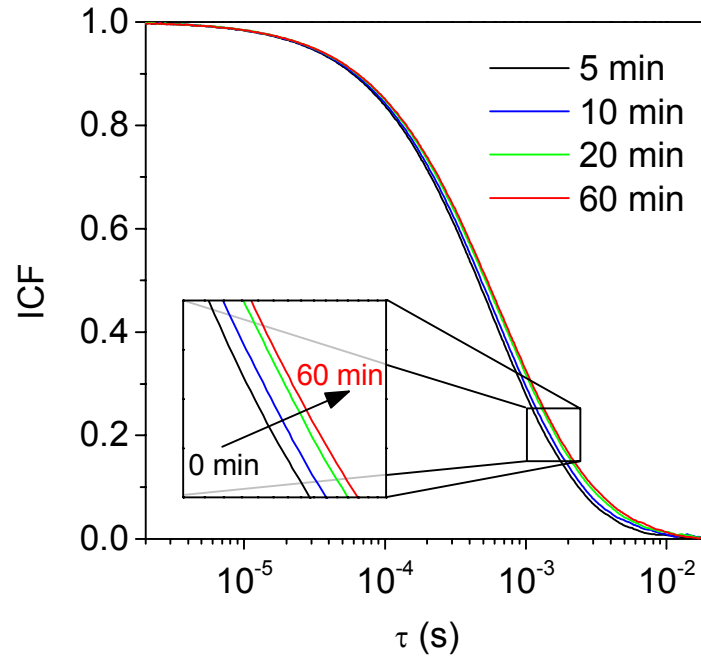


Fig. 4.2 The intensity correlation function (ICF) as a function of the lag time τ of 0.5 g/l K8/K18 measured by DWS after different assembly times.

The MSD was derived from the motion of the tracer particles in MPT experiments. The results from MPT experiments after different measuring times are shown in Fig. 4.3. The average MSD of the first set of tracked particles already levels off and approaches a constant plateau at long time scales. This is typical for particles, which are confined by a network. The network has already constituted itself as observed in the shear rheological measurements (Fig. 4.1). The change in the MSD at $\tau \rightarrow \infty$ within the first time period is nearly the same as the change in the second time period even though the time interval between the measurements increases from 5 min to 50 min. According to the inset of Fig. 4.3, the qualitative time evolution of the storage modulus derived from MPT data is the same as in shear rheological measurements.

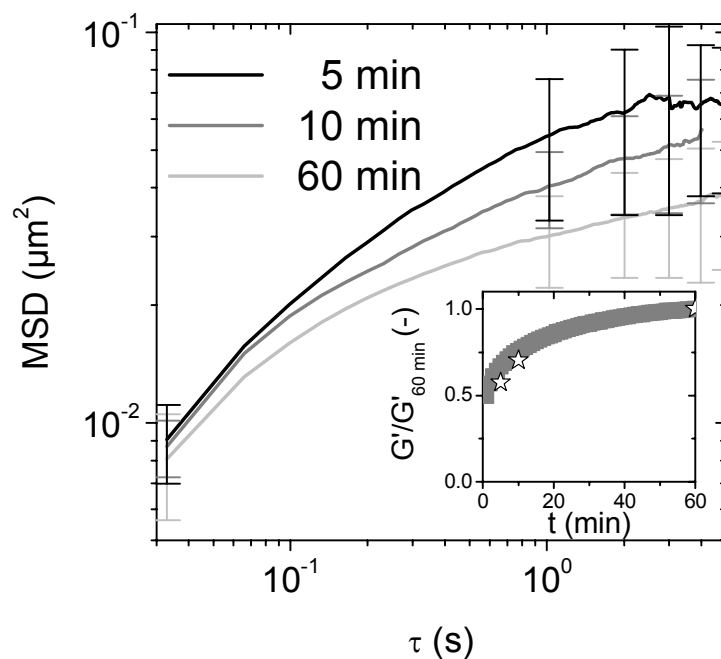


Fig. 4.3 The MSD after different assembly times measured by MPT using uncoated $0.52 \mu\text{m}$ particles at a protein concentration of 0.5 g/l K8/K18. The inset shows the time evolution of G' at $\omega = 1 \text{ rad/s}$ determined by shear rheology (grey squares) and by MPT (black stars) normalized by the G' after 60 min.

The increase in G' of the K8/K18 networks after 60 min is small enough that G' essentially stays constant on the time scale of all subsequent experiments. Therefore, a network formation time of 60 min at $20 \text{ }^\circ\text{C}$ was chosen for all following experiments.

4.2 Network architecture of K8/K18 networks

SEM images and MPT experiments of K8/K18 networks at different protein and magnesium chloride concentrations shown in Fig. 4.4 were used to assess the network structure.

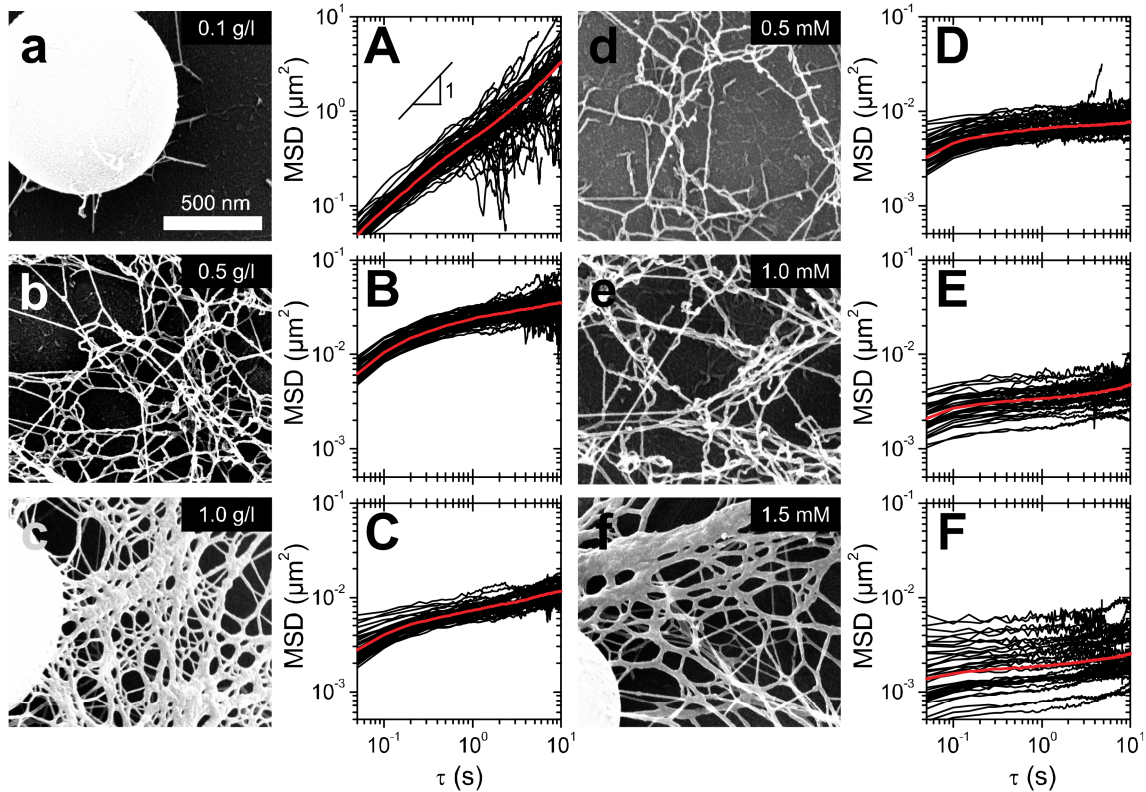


Fig. 4.4 SEM images (small letters) and MSDs of $1.01 \mu\text{m}$ PEG coated particles (capital letters) of K8/K18 networks without salt at different protein concentrations (a-c) and at different MgCl_2 concentrations and a protein concentration of 0.5 g/l (d-f). Scale bar is the same for all panels.

The micrograph representing a K8/K18 network at 0.1 mg/ml (Fig. 4.4a) shows no space filling network as only few bright filaments were found between the beads and the substrate. Most filaments, however, lay on the glass substrate. The images of networks encountered at a protein concentration of 0.5 g/l and magnesium ion concentrations between 0.5 and 1.0 mM (Fig. 4.4b, d, and e) appear fairly homogeneous and are similar to those extracted from epithelia cells as shown by Leitner et al. (2012). The filaments on SEM images seem to be more stretched as on TEM images from highly diluted filament solutions (Lichtenstern et al., 2012). This may reflect a stretched filament conformation in the network or may be an artifact from sample preparation. A stretched filament conformation was also found on cryo-TEM images of vimentin (Kirmse et al., 2010). For

cryo-TEM the samples are flash frozen in their native environment, so that artifacts from dehydration, fixation, and staining can be avoided. These findings indicate the existence of stretched filaments in IF networks. SEM images at a protein concentration of 1.0 g/l (Fig. 4.4c) and 0.5 g/l protein in combination with 1.5 mM magnesium chloride (Fig. 4.4f) show mainly bundled filaments with some single filaments as concluded from the apparent filament diameters. Whether these bundled filaments are characteristic for these networks or just an artifact from sample preparation will be discussed in the light of the results from MPT experiments.

The MPT experiments characterize the homogeneity of the networks in their natural aqueous environment (Valentine et al., 2001). At a protein concentration of 0.1 g/l the mean square displacements of particles with a diameter of 1.01 μm increase linearly with time, i.e. the particles diffuse freely in a purely viscous environment (Fig. 4.4A). Therefore, it can be concluded, that the mesh size ζ at 0.1 g/l is larger than 1.01 μm . This is consistent with an estimate of the mesh size assuming a cubic grid of rigid filaments (equation 2.6). This cubic model results in a value of $\zeta = 0.97 \mu\text{m}$ for 0.1 g/l K8/K18, which is close to the particle diameter. At K8/K18 concentrations of 0.5 g/l the MSDs approach a constant value indicating that the particles are trapped in an elastic environment (Fig. 4.4B). Consistently, the mesh size estimated from a cubic grid is $\zeta = 0.435 \mu\text{m}$ for K8/K18 (equation 2.6), which is significantly smaller than the particle diameter. The addition of magnesium chloride decreases the magnitude and slope of the MSDs (Fig. 4.4D, E, and F) indicating that the network becomes stiffer upon addition of divalent ions. Moreover, the distribution of MSD values at a given lag time τ broadens with increasing magnesium chloride concentrations demonstrating that the network inhomogeneity increases when salt is added. In contrast, the distribution of MSD values is fairly narrow for the samples without added salt independent of protein concentration.

The non-Gaussian parameter α_2 was calculated to analyze the heterogeneity of the samples quantitatively (Kegel and van Blaaderen, 2000). The parameter compares the forth and the second moment of the distribution of distances $\Delta x(\tau)$ particles travel within the time interval τ :

$$\alpha_2 = \frac{\langle \Delta x(\tau)^4 \rangle}{3\langle \Delta x(\tau)^2 \rangle^2} - 1. \quad 4.1$$

The α_2 -parameter is zero for a Gaussian distribution of MSDs expected for homogeneous samples and increases with increasing inhomogeneity of the environment explored by the tracer particles. Fig. 4.5 shows the results from five independent experiments with different particle diameters and different surface functionalities at an interval lag time of $\tau = 1$ s. The results illustrate that the heterogeneity increases with protein but even more with magnesium concentration. The heterogeneity of the sample with 1.0 g/l K8/K18 is similar to the sample with 0.5 g/l K8/K18 at a magnesium chloride concentration of 0.5 mM, which clearly shows no bundling on SEM images (Fig. 1d). Generally, bundling results in an inhomogeneous network structure (Apgar et al., 2000; Tseng and Wirtz, 2001). Since the α_2 values for the salt-free protein networks are close to zero, it can be assumed, that bundling for the 1.0 g/l K8/K18 sample appearing in Fig. 4.4c, is an artifact from sample preparation.

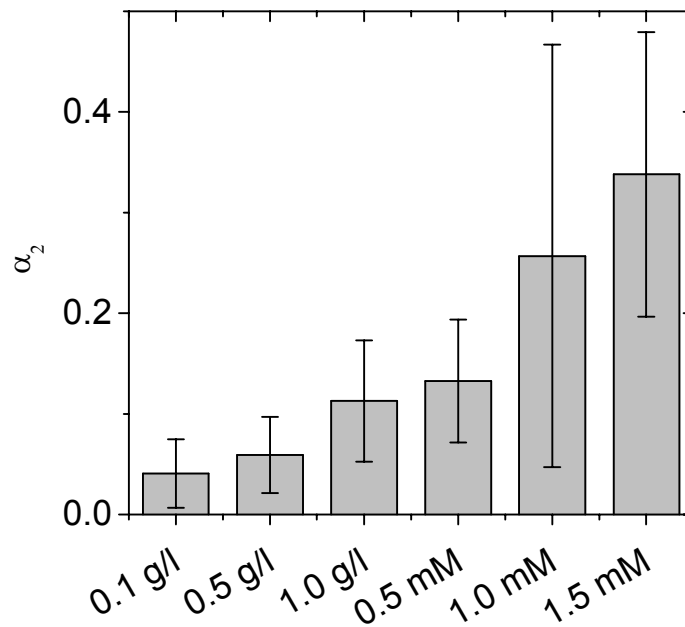


Fig. 4.5 Heterogeneity of the networks measured by the non-Gaussian parameter α_2 at a time interval of $\tau = 1$ s for samples with different K8/K18 concentrations and for samples with different MgCl_2 concentrations at a fixed K8/K18 concentration of 0.5 g/l.

A sedimentation assay at different protein and different magnesium chloride concentrations allows to assess the influence of these parameters

on the fraction of long filaments or bundles. Long filaments or bundles sediment at lower centrifugation speeds because of their higher mass.

Fig. 4.6 shows the amount of K8 and K18 in the supernatant and in the pellet after low speed centrifugation for 15 min at 21.380g. The size of the spots reflects the amount of protein in the respective fraction. The upper spot on each lane represents K8 because the molecular weight of K8 is higher than for K18. The results indicate that the fraction of protein in the supernatant and in the pellet without salt remains constant with increasing protein concentration. In contrast, the amount of protein in the pellet strongly increases after addition of magnesium chloride. At a salt concentration of 1.0 mM magnesium chloride almost all protein can be found in the pellet. Hence, the fraction of heavy species such as bundles increases with magnesium ion concentration.

The centrifugation assay confirm the results of the multiple particle tracking experiments showing that the structure without salt remains unchanged but that inhomogeneity increases upon addition of magnesium chloride.

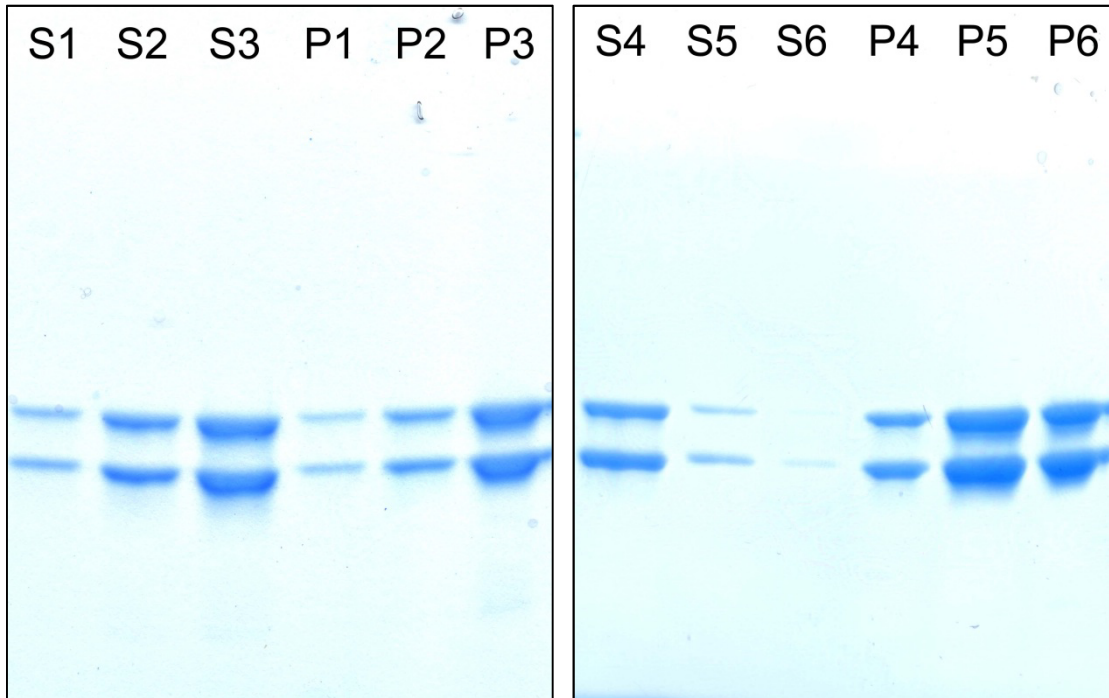


Fig. 4.6 Scanned images of SDS polyacrylamide gels with the supernatant (S) and the pellet (P) fraction after centrifugation. The sample numbers, 1, 2, and 3 correspond to K8/K18 concentrations of 0.1, 0.5, and 1.0 g/l, respectively. The numbers 4, 5, and 6 correspond to MgCl_2 concentrations of 0, 0.5, and 1.0 mM at a protein concentration of 0.5 g/l.

The mesh size of filament networks can be directly determined from MPT experiments by variation of the particle diameter at a constant protein concentration (Gardel et al., 2003; Köster et al., 2010). Here, the mesh size of K8/K18 at a concentration of 1.0 g/l was investigated using particles with diameters of 0.19 μm , 0.52 μm , and 1.01 μm . Fig. 4.7 shows the MSDs of randomly chosen particles with the respective diameters. The inset represents an example of a trajectory with a length of 3 s. The particles with a diameter of 0.19 μm diffuse freely through the meshes of the network and the MSD increases linearly with time as expected for a viscous fluid. At particle diameters of 0.52 μm or bigger the motion of the particles is confined by the network and the MSDs approach a constant value at long time scales. Accordingly, the mesh size is between 0.19 and 0.52 μm . The mesh size calculated assuming a cubic grid of K8/K18 filaments (equation 2.6) is $\xi = 0.35 \mu\text{m}$ at a protein concentration of 1.0 g/l. The result for a cubic grid agrees well with the mesh size determined by MPT. This good agreement shows that the model is appropriate to describe the network architecture. In this case the difference between the contour length of the filament between adjacent cross-links L_c and the mesh size ξ is small because the filaments are stiff. The persistence length l_p of K8/K18 determined from the curvature of filaments on micrographs is 0.3 μm (Lichtenstern et al., 2012) and hence $l_p \approx L_c$. Good agreement between the mesh size from MPT and the cubic model has also been reported for vimentin networks (Köster et al., 2010).

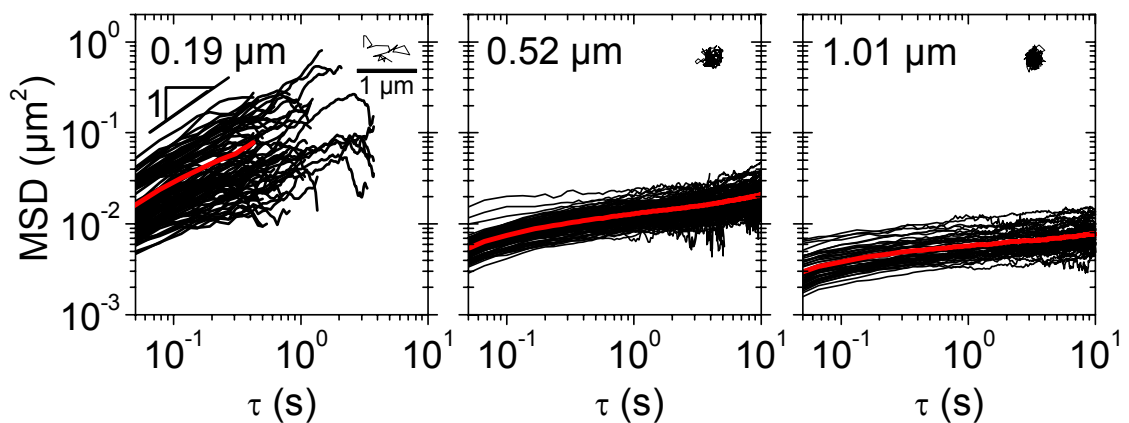


Fig. 4.7 MSDs against lag time τ and the individual trajectories after $\tau = 3 \text{ s}$ (inset) of microspheres with diameters of 0.19, 0.52, and 1.01 μm at a K8/K18 concentration of 1.0 g/l. The red line is the average MSD.

The good agreement between the mesh size determined from particle tracking and the theoretical value for a cubic network of individual filaments shows that the network consists of individual filaments and bundling is not relevant for pure K8/K18 networks without added salt. There is no indication for bundling as observed for IF networks from keratin 5 and keratin 14 (Bousquet et al., 2001; Ma et al., 2001), or K8/K18 at pH 7.0 (Yamada et al., 2003) or in the presence of salt (Kayser et al., 2012; Yamada et al., 2002). This is further supported by the low values of the non-Gaussian parameter α_2 . The results also demonstrate that the mesh size of these homogeneous K8/K18 networks can be assessed by assuming a cubic grid of filaments (equation 2.6).

4.3 Measurement of the shear rheological properties of K8/K18 networks

4.3.1 Influence of the measuring conditions

Small amplitude oscillatory shear experiments were performed using different surface treatments and different setups in order to judge the effect of experimental artifacts or secondary flow phenomena.

First, the influence of the surface treatment on the viscoelastic properties was determined. Yamada et al. 2003 suggested that the elastic properties of K8/K18 are dominated by a strong contribution of the air-liquid interface at the rim of the rheometer fixture. According to their results, these contribution could be suppressed by a coating with phosphor lipids (1,2-Dimyristoyl-rac-glycero-3-phosphocholine, Sigma-Aldrich) in chloroform. For long measurements at low gap width, the surface was coated with low viscosity paraffin oil to prevent evaporation of water.

The results of experiments of K8/K18 networks with different surface treatments in Fig. 4.8 show that the magnitude and the frequency dependency of the storage modulus G' and the loss modulus G'' in the linear viscoelastic regime at a concentration of 0.5 g/l deviate from each other by less than 18 %. The deviation in G' of seven independent measurements at the same conditions is about 25 %.

Surface effects are not relevant here as the data obtained with different surface treatment agree well within experimental error. Hence, the observations of Yamada and co-workers cannot be reproduced with our setup and the proteins used here. In addition, the results are not affected by paraffin oil coating of the air-sample interface at the rim of the rheometer plates.

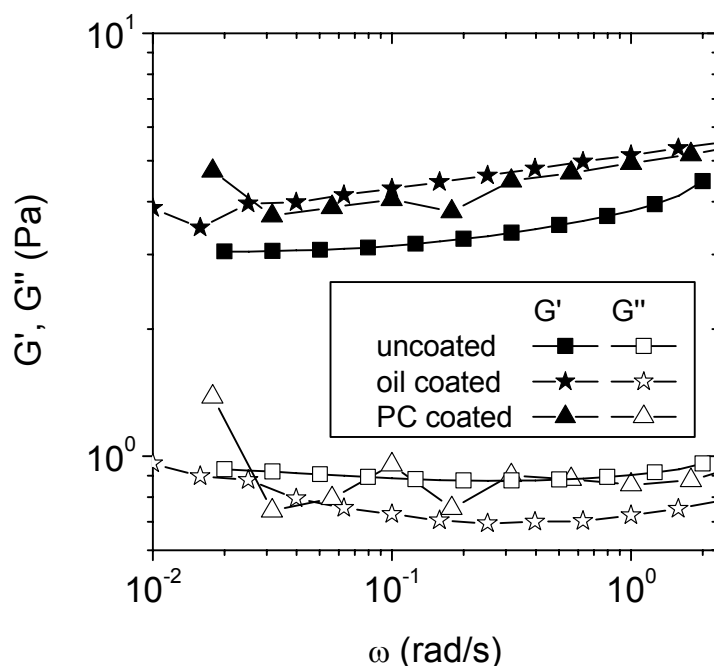


Fig. 4.8 Frequency dependency of the storage modulus $G'(\omega)$ and the loss modulus $G''(\omega)$ in the linear viscoelastic regime of K8/K18 filaments at 0.5 g/l without surface coating, with oil coated surface, and with phosphorlipid coating (PC).

In the second step, experiments using different rheometer setups were performed. All experiments were conducted at least for two different protein concentrations to make sure that the setup neither affects the absolute value of G' at a constant concentration nor the concentration dependency of G' .

In the first experiment, the diameter of the rheometer plate was changed from 50 mm to 25 mm at a constant gap width of 0.12 mm. As a consequence, the ratio of the air-liquid interface to sample volume increases by a factor of two. If the elasticity of the air-liquid interface would contribute significantly to the apparent bulk rheological properties as reported by Yamada and colleagues (Yamada et al., 2003), the modulus should increase with decreasing plate diameter. Changes of the bulk concentration due to aggregation at the air-liquid interface would be well below 1 % of the total protein concentration even if the interface would be densely packed with protein molecules (surface area per protein molecule 10 nm^2). Fig. 4.9 shows, that the elasticity of the air-liquid interface is not relevant here, as the G' data at 6.3 rad/sec obtained at different protein concentrations with different geometries agree well within experimental error.

Next, the gap width was changed from 0.12 mm to 1.2 mm at a constant plate diameter of 25 mm, i.e. the sample volume changes from 70 μl to 600 μl . The load on the sample while squeezing the droplet into the rheometer gap and the time to fill the rheometer gap increases drastically with decreasing gap width. Again no significant effect on the resulting modulus data is observed. Consequently, the gap width has no significant effect on the subsequent assembly and network formation. This is particularly remarkable since K8/K18 assembles more than 80 times faster than e.g. vimentin (Lichtenstern et al., 2012). Furthermore, measuring the shear moduli could be affected by wall slip. Then the apparent moduli should decrease with decreasing gap width, but the data shown in Fig. 4.9 do not indicate that this phenomenon is relevant here.

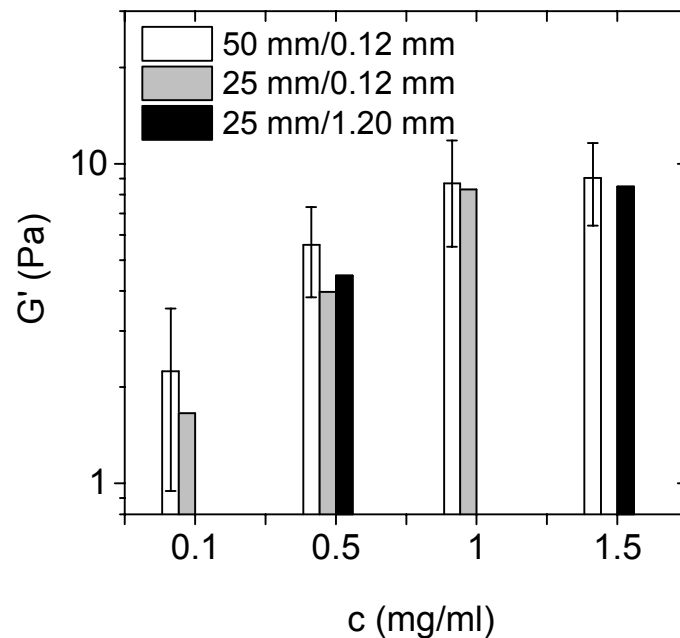


Fig. 4.9 The elastic modulus G' at a frequency of 6.3 rad/s at different K8/K18 concentrations measured with 50 mm plate with 0.12 mm gap (white), with a 25 mm plate with 0.12 mm gap (grey), and with a 25 mm plate and a 1.2 mm gap (black).

In conclusion, artifacts from sample surface elasticity, wall slip, the filling process or network formation within the rheometer gap can be excluded.

4.3.2 Measurement of the non-linear properties

A simple method to characterize the non-linear properties of these gels is the application of stress-controlled oscillations at a constant sinusoidal frequency and increasing amplitude $\hat{\sigma}$. In the linear regime, the output signal has the same sinusoidal form as the input signal. The moduli remain constant with increasing amplitude of the input signal. In the non-linear regime above a critical deformation γ_{crit} the moduli start to change and the response signal becomes distorted. However, the stress-controlled rheometer determines an apparent storage modulus $G' = (\hat{\sigma}/\hat{\gamma}) \cos \delta$ and an apparent loss modulus $G'' = (\hat{\sigma}/\hat{\gamma}) \sin \delta$ from the input signal, the apparent phase shift δ and the apparent strain amplitude $\hat{\sigma}$ calculated from the first harmonic after Fast-Fourier transformation. These LAOS experiments have been used to compare the influence of mutations or buffer conditions on strain stiffening of keratin, vimentin, and desmin networks qualitatively (Ma et al., 2001, 1999; Schopferer et al., 2009; Yamada et al., 2002). A drop of the apparent storage modulus G' at large amplitudes is an indication for strain softening and an increase indicates strain stiffening. The network properties change dramatically after exceeding a maximum strain γ_{max} at which the network ruptures.

The result of a LAOS experiment for K8/K18 at a concentration of 0.5 g/l is shown in Fig. 4.10. The shape of the curve indicates softening of the network and no strain stiffening. This is in contrast to the findings for desmin and vimentin at similar length densities (Schopferer et al., 2009).

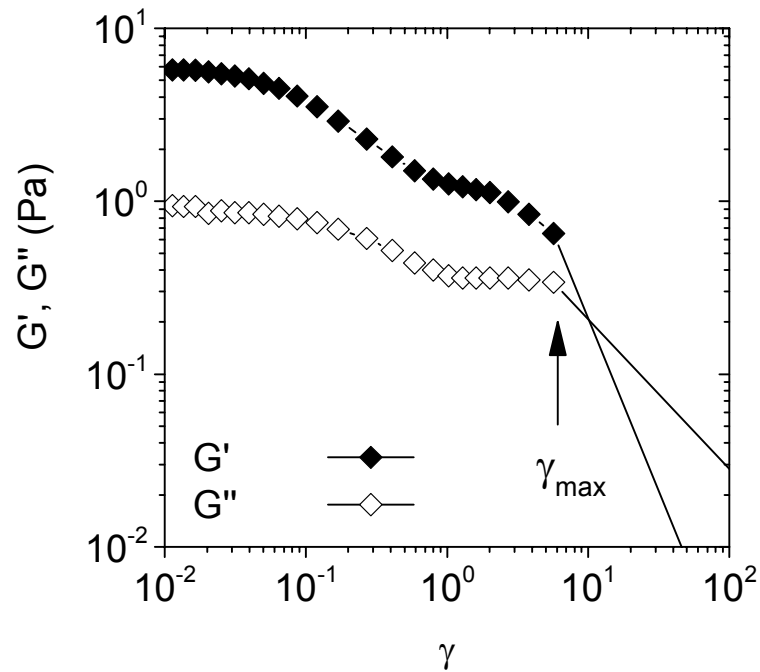


Fig. 4.10 Apparent G' and G'' as calculated by the rheometer software as a function of the strain amplitude γ at $\omega = 1$ rad/s of K8/K18 at a protein concentration of 0.5 g/l.

Fig. 4.11 shows the raw oscillatory signal in the non-linear regime and the first harmonic oscillation used by the rheometer software to calculate the apparent moduli. The raw data of the strain response is clearly non-sinusoidal. The strain amplitude of the sinusoidal fit used for the calculation of the moduli of K8/K18 is higher than the real strain response. This shows that the interpretation of the apparent moduli is problematic, because the strain amplitude used in the calculations directly influences the apparent moduli.

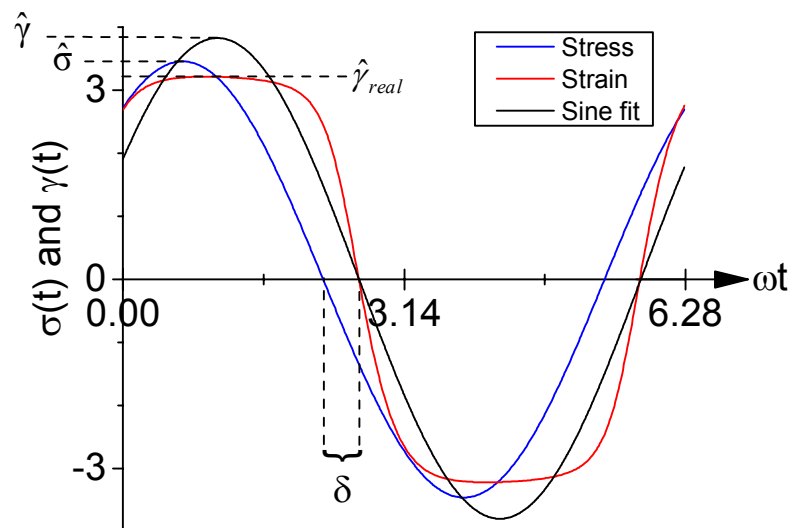


Fig. 4.11 Raw data in the non-linear regime used for Fig. 4.10 at $\sigma = 3.51$ Pa and the sinusoidal fit, from which the apparent moduli were calculated.

To compare the raw data of all data points of the LAOS experiment in Fig. 4.10 Lissajous figures were generated by plotting γ_{raw} against σ_{raw} (Fig. 4.12). In the linear viscoelastic regime the Lissajou figures of viscoelastic materials have the form of an ellipse. The ellipse becomes a line for purely elastic materials and a circle for viscous fluids. In the non-linear regime the signal becomes distorted. The inset of Fig. 4.12 shows the linear viscoelastic response of K8/K18 at small deformations. The shape of the Lissajou figures clearly becomes distorted at large deformation. In addition, the center of the strain response clearly moves away from the origin towards larger strains even though the input stress signal is always symmetric around the x -axis.

This can be explained by plastic flow and a non-reversible increase in elasticity after half of the oscillation cycle. The stiffening within a single oscillation cycle means that the response signal is not only non-sinusoidal but also aperiodical. An aperiodic response in LAOS experiments was also observed for K5/K14 and actin networks (Ma et al., 1999; Semmrich et al., 2008).

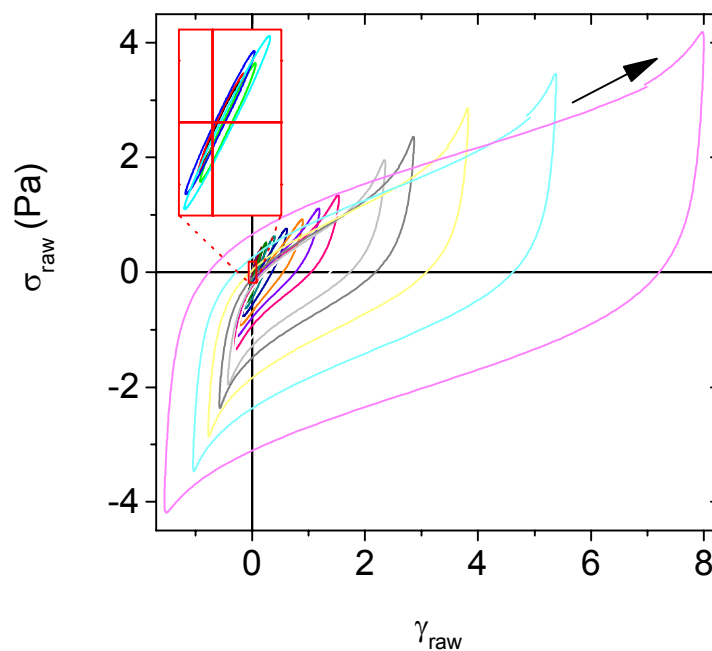


Fig. 4.12 Lissajou figures of the raw data of Fig. 4.10.

A convenient quantitative evaluation of the Lissajous figures was suggested by Ewoldt and co-workers (2008). The method was applied using the raw data of the LAOS experiment with K8/K18 at a concentration of 0.5 g/l (Fig. 4.10). Fig. 4.13a shows a Lissajou figure in the linear

regime and Fig. 4.13b a Lissajou plot in the non-linear regime. The origin of the coordinate system was always placed at the center of the Lissajou figure for a better illustration. The method defines a minimum strain modulus G_M' and a large strain modulus G_L' . G_M' is obtained by the slope of the stress-strain-curve at small deformations. $G_L' = \sigma_{max}/\gamma_{max}$ is the ratio of stress and strain at the maximum strain.

In the linear regime in Fig. 4.13a all values are identical $G' = G_M' = G_L'$. The slope of the Lissajou curve at small strains and therefore G_M' decreases in the non-linear regime. Hence, the material shows softening at small deformations. On the other hand, G_L' in the non-linear regime in Fig. 4.13b is clearly larger than G_M' until reaching the maximum stress.

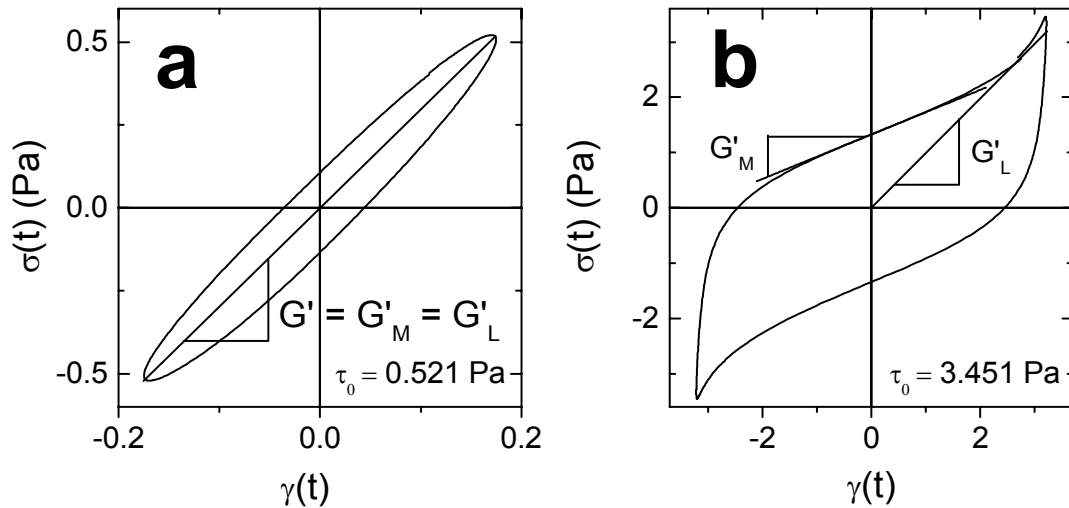


Fig. 4.13 Lissajou plots from the raw data of Fig. 4.10 in the linear regime (a) and in the non-linear regime (b). The lines illustrate the calculation of the minimum strain modulus G_M' and the large strain modulus G_L' .

Strain stiffening can be characterized by the strain stiffening index $S = G_L'/G_M'$, which is defined as the ratio of G_L' to G_M' (Semmrich et al., 2008). The results in Fig. 4.14 show that the stiffening response overweighs the softening at large deformations. The strain stiffening as characterized by the index S is in contrast to the softening determined by the apparent moduli calculated by the rheometer software.

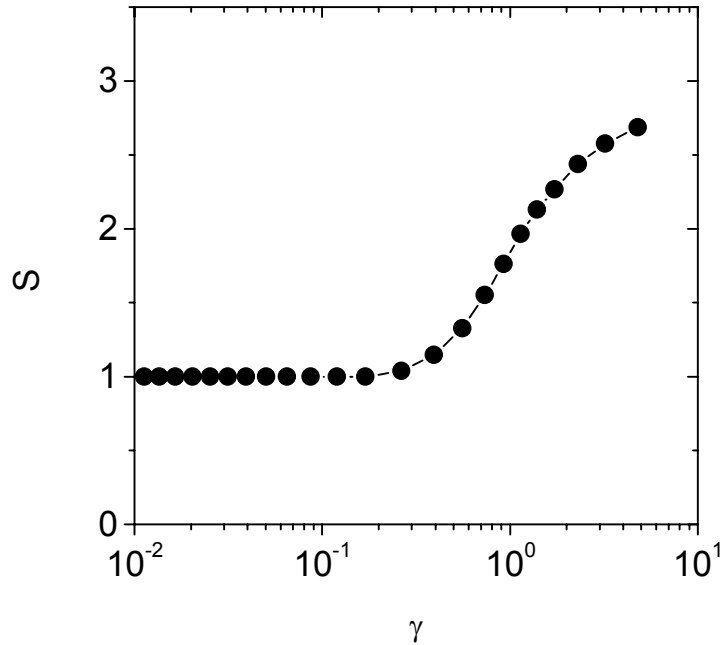


Fig. 4.14 Strain stiffening index of K8/K18 at a protein concentration of 0.5 g/l as a function of strain.

The apparent moduli from LAOS experiments have been used recently to characterize strain stiffening for vimentin, desmin as well as keratin networks and proved that they are well suited for qualitative comparison (Bär et al., 2010; Ma et al., 2001; Schopferer et al., 2009).

The discussion shows that the interpretation of the apparent moduli and a rigorous comparison to theory, as e.g. the glassy wormlike chain model, is difficult. Even a more sophisticated analysis of the LAOS data using the strain stiffening index S has disadvantages because the oscillations become aperiodic due to plastic flow and intracyclic strain stiffening. Therefore, other experimental protocols to investigate the nonlinear viscoelastic response of keratin networks were examined as suggested in the literature (Broedersz et al., 2010; Semmrich et al., 2008). These methods rely on the so-called differential modulus K .

The differential modulus K' can be measured by the pre-stress protocol. The method is based on the application of a steady pre-stress σ_0 and superposition of a small amplitude oscillatory stress (Broedersz et al., 2010b). Here, a constant pre-stress σ_0 was applied for 2 min and a small oscillatory stress with an amplitude of $\partial\sigma_0 \approx 0.1\sigma_0$ was superimposed. From

the resulting oscillatory strain amplitude $\hat{\gamma}_0$ and phase shift δ the differential storage modulus was calculated $K' = (\partial\sigma_0/\partial\gamma_0) \cos \delta$.

The corresponding data for a K8/K18 concentration of 0.5 g/l are shown in Fig. 4.15. The measured signal increases at the beginning of each stress pulse, but after ~ 1 min a steady state is reached and K' is evaluated. The inset shows K' as a function of pre-stress σ_0 .

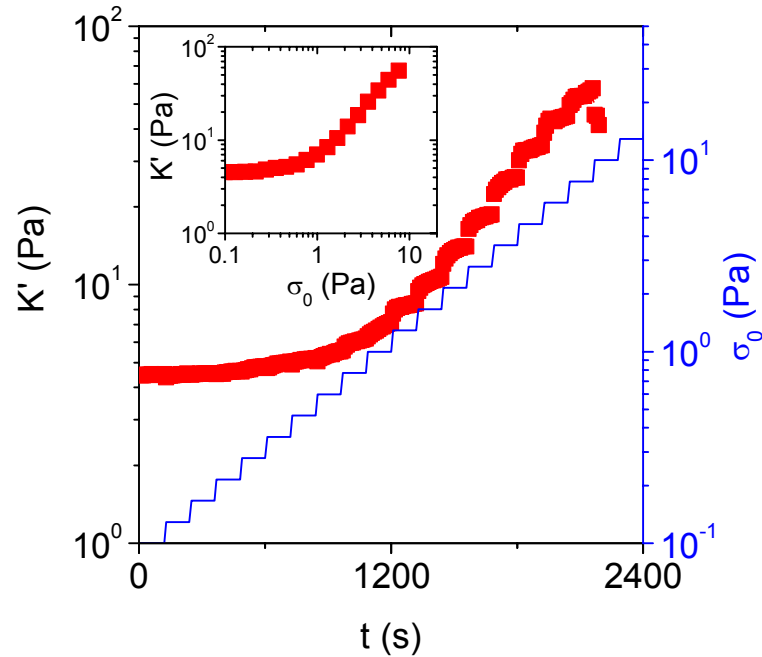


Fig. 4.15 The differential storage modulus K' versus time at a constant frequency of $\omega = 6.3$ rad/s and varying pre-stress σ_0 at a K8/K18 concentration of 0.5 g/l. The time interval for each step is 2 min. The inset shows K' as a function of σ_0 .

In the linear regime at low pre-stresses σ_0 the differential modulus K' is constant and equals the plateau modulus G_0 . After reaching a critical pre-stress σ_{crit} the network starts to stiffen. From σ_{crit} the critical strain γ_{crit} can be calculated as $\gamma_{crit} = \sigma_{crit}/G_0$. The differential modulus increases until a maximum stress σ_{max} is reached at which the network ruptures. At this point the network reaches the highest elasticity K'_{max} .

Fig. 4.16 shows results obtained with this method using two different geometries and different plate diameters. The shape of the curve overlap very well and all characteristic values agree within experimental error. The good reproducibility is also the main advantage of the pre-stress protocol. Disadvantages of the method are long measurement times and the limitation to frequencies around 6.3 rad/s to characterize materials in order

to achieve a sufficient signal to noise ratio. This makes it difficult to characterize networks with very low G_0 values, which cannot be analyzed at frequencies of 6.3 rad/s because of errors due to inertia of the rotating rheometer tools.

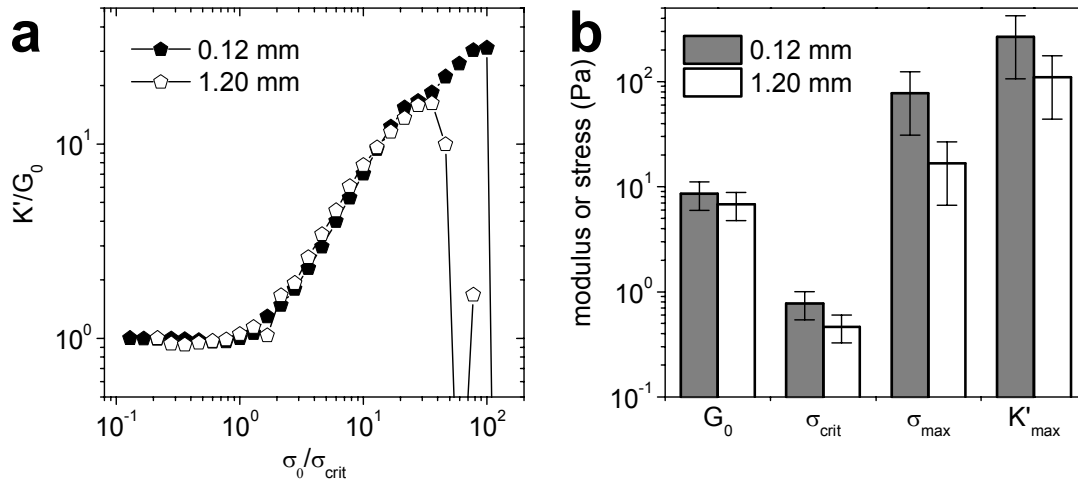


Fig. 4.16 Differential modulus of K8/K18 at a concentration of 1.5 g/l measured at a gap of 0.12 mm and a 50 mm plate, and a gap of 1.2 mm and a 25 mm plate. The functional form is the same (a) and the characteristic values agree within experimental error (b).

Consecutive creep and relaxation experiments were performed for K8/K18 to evaluate the creep of the sample during pre-stress experiments. The results shown in Fig. 4.17 indicate that the sample exhibits significant creep. This is typical for networks with transient cross-links, which can break and reform (Broedersz et al., 2010b). Even though the sample exhibits significant creep the differential modulus at each stress step approaches a constant value (Fig. 4.15). Earlier, it was already shown that the pre-stress protocol is insensitive to creep (Broedersz et al., 2010b).

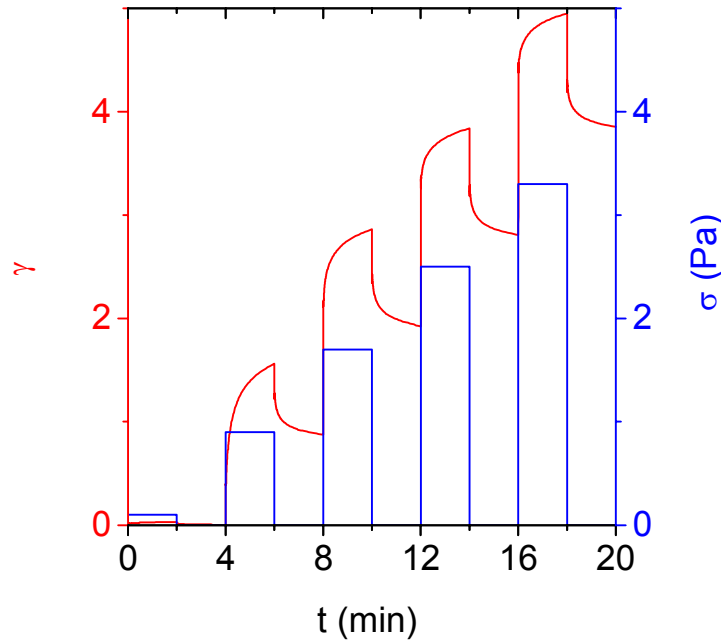


Fig. 4.17 Consecutive creep and relaxation cycles of K8/K18 at a concentration of 0.5 g/l show plastic flow of the network during each stress period.

The strain-ramp protocol is a complementary method to measure the differential modulus. For this protocol, the strain is steadily increased at a constant shear rate and the stress response was measured (Fig. 4.18a). The differential modulus is calculated from the derivative $K = d\sigma/d\gamma$ of the smoothed stress-strain curve. The results in Fig. 4.18b show that the data are independent of strain rate. In contrast, the protocol revealed a strong strain rate dependency for entangled networks of actin (Broedersz et al., 2010b; Semmrich et al., 2008). So far, strain rate independent results of the strain ramp protocol were only found for cross-linked protein filament networks e.g. actin networks cross-linked by biotin–NeutrAvidin or cross-linked fibrin networks (Broedersz et al., 2010b).

The advantages of the strain-ramp protocol are the short measuring times and the applicability for very weak gels. On the other side, it is difficult to maintain the strain rate using a stress controlled rheometer, which results in large errors especially at low strains. Depending on the smoothing algorithms of the software, these errors can have a strong effect on the resulting differential modulus data.

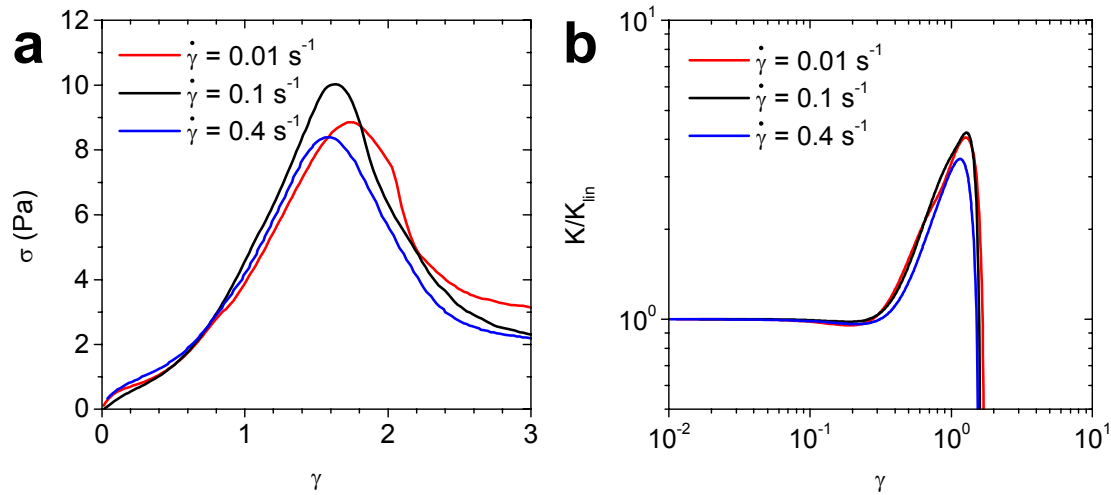


Fig. 4.18 (a) Stress σ versus strain γ of K8/K18 at a concentration of 0.5 g/l for various shear rates. (b) The differential modulus $K = d\sigma/d\gamma$ normalized by the linear modulus K_{lin} versus the strain γ .

The results of all discussed methods normalized by G_0 are plotted in Fig. 4.19. The stress at which the networks rupture is the same for all methods. All methods except the amplitude sweep experiment clearly show the stiffening of the K8/K18 networks. Consequently, the apparent moduli obtained by the simple evaluation of amplitude sweep experiments are not appropriate for quantitative analysis of the strain stiffening response. Even the interpretation of the strain stiffening index S obtained from the raw data of amplitude sweep experiments is difficult because of aperiodical response signal in LAOS experiments. Therefore, the differential modulus was used to characterize the non-linear viscoelastic properties. The pre-stress protocol was selected in most experiments because of the good reproducibility. In some cases, the strain ramp protocol was the method of choice because it allows to extend the measuring range to materials with very low G_0 values.

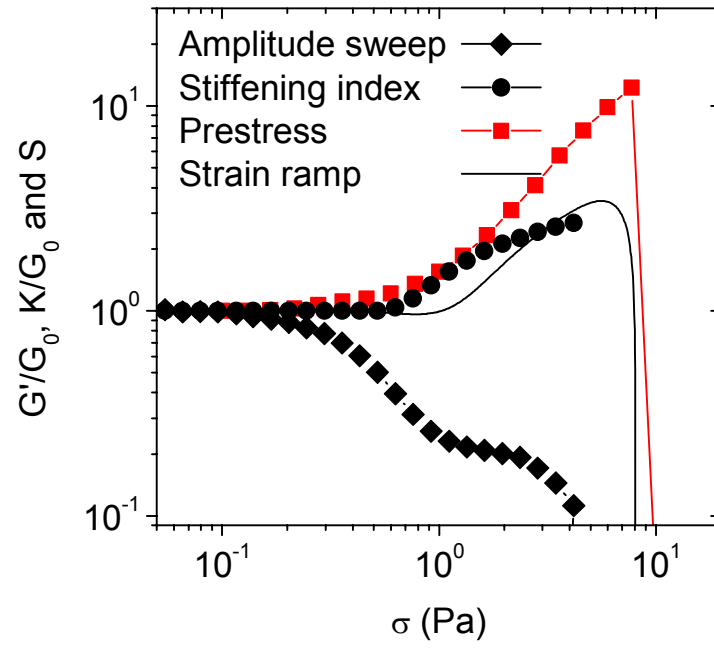


Fig. 4.19 Comparison of different protocols to characterize the non-linear rheological properties.

4.4 Viscoelastic properties of pure K8/K18 networks

The influence of concentration on the viscoelastic properties at buffer conditions of 10 mM Tris-HCl (pH 7.4) has been characterized by linear and non-linear shear rheology, high frequency squeeze flow as well as different microrheological methods. Corresponding results are presented and discussed in this section.

4.4.1 Results

Linear oscillatory shear data at different protein concentrations is shown in Fig. 4.20. All samples show predominant elastic behavior in the frequency range between 0.01 and 25 rad/sec, i.e. $G' \gg G''$. This is also true for K8/K18 concentrations as low as 0.1 g/l for which SEM images (Fig. 4.4) did not show a filament network. Here, G' is approximately frequency independent and its absolute value is termed the plateau modulus G_0 . The dissipation factor $\tan \delta = G''/G'$ of all samples is between 0.1 and 0.2.

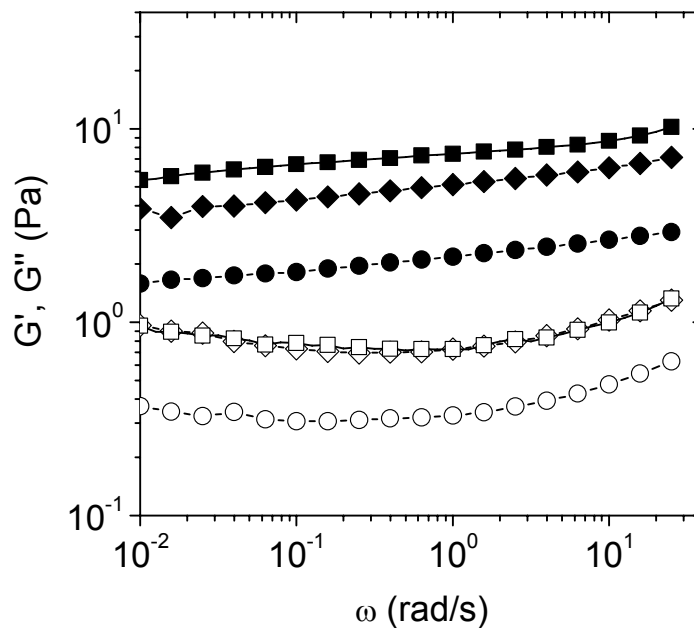


Fig. 4.20 Frequency dependency of the storage modulus G' (closed symbols) and the viscous modulus G'' (open symbols) in the linear viscoelastic regime of K8/K18 filaments at concentrations of 0.1 g/l (cycles), 0.5 g/l (diamonds), and 1.0 g/l (squares).

In addition, MPT measurements were conducted to determine the viscoelastic properties. The MSD and the resulting moduli for unfunctionalized particles with diameter of 1.01 μm are shown in Fig. 4.21.

A prerequisite to compare the moduli from bulk rheology with microrheological data is a homogeneous sample with a mesh size much smaller than the particle diameter. Most MSDs in the experiments presented in Fig. 4.21A, B, and C are all close to the averaged MSD value illustrated by the red line. This confirms that the samples are fairly homogeneous. The linear increase of the MSD at a K8/K18 concentration of 0.1 g/l (Fig. 4.21A) shows that the particles diffuse through the meshes of the filament network. Accordingly, the respective moduli (Fig. 4.21a) are dominated by the loss modulus G'' . At larger diameters the particles are trapped by the network and the MSDs approach a time independent plateau at large lag times τ (Fig. 4.21B & C). The corresponding moduli at low frequencies are dominated by the storage modulus (Fig. 4.21b & c). The storage modulus G' at a K8/K18 concentration of 0.5 g/l exhibit similar absolute values as obtained by Leitner et al. (2012) but is significantly lower than the values determined from bulk rheology in Fig. 4.20.

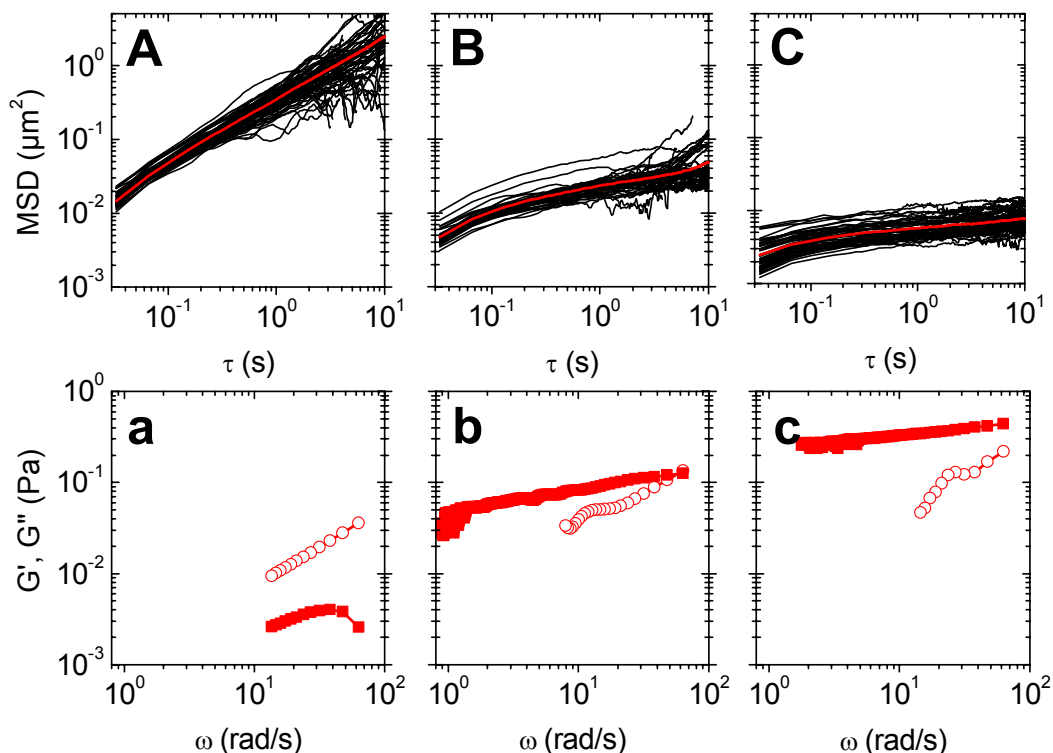


Fig. 4.21 Mean square displacements (capital letters) and moduli derived from the averaged MSD (small letters) measured with $1.01 \mu\text{m}$ unfunctionalized particles at K8/K18 concentrations of 0.1, 0.5, and 1.0 g/l. G' is denoted using closed symbols and G'' using open symbols.

Fig. 4.22 shows the plateau modulus G_0 as a function of protein concentration c as obtained from linear oscillatory shear rheometry and

MPT. The keratin concentration dependency of G_0 measured by shear rheology is weak and can be described by a power law $G_0 \sim c^x$ with $x = 0.5 \pm 0.08$. A similar weak influence of protein concentration on the plateau modulus was found for intermediate filament networks of K5/K14 (Ma et al., 1999), vimentin (Janmey et al., 1991; Ma et al., 1999; Schopferer et al., 2009), desmin (Schopferer et al., 2009), and K8/K18 (Yamada et al., 2003) without treatment of the air-liquid interface by phospholipids. The exponents in these investigations are ranging from $x = 0.25$ for untreated K8/K18 (Yamada et al., 2003) to $x = 0.70$ for desmin (Schopferer et al., 2009). In contrast, the moduli measured by MPT are significantly lower and show a much stronger concentration dependency ($x = 1.1 \pm 0.3$) than the moduli determined by bulk rheology.

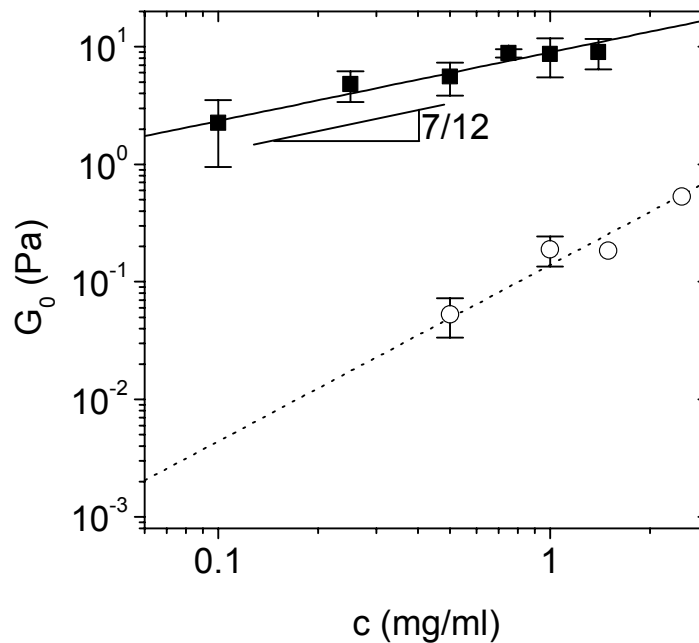


Fig. 4.22 The plateau modulus G_0 from bulk rheology (squares) and from MPT (open circles) versus K8/K18 concentration measured at a frequency of 1 rad/s. The black line illustrates a scaling of $G_0 \sim c^{7/12}$. The dotted line shows the results obtained by the cubic grid model in equation 2.15.

The frequency dependence of the storage modulus G' and the loss modulus G'' obtained from MPT and shear rheometry cover the frequency range up to 100 rad/s. Oscillatory squeeze flow and DWS have been used to expand the frequency range beyond 10^5 rad/s. DWS is applied here to IF networks for the first time. Fig. 2.23 show that the viscoelastic properties of

K8/K18 determined by DWS and mechanical squeeze flow agree well with the results from MPT measurements.

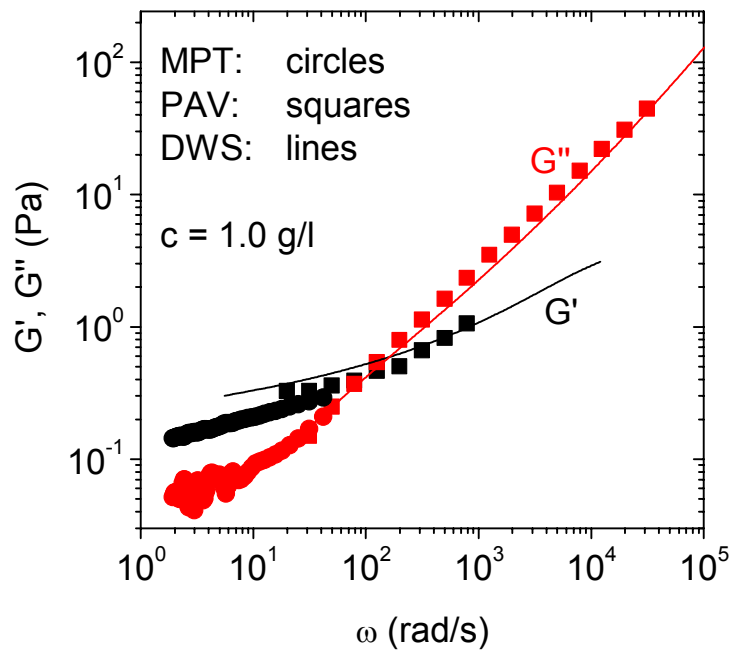


Fig. 4.23 Comparison of storage G' and loss moduli G'' of K8/K18 as obtained by MPT, oscillatory squeeze flow and DWS.

The slope of the loss modulus changes in the high frequency regime. Fig. 4.24 shows the loss modulus G'' corrected by the contribution of the buffer solution $\eta_s \omega$. The viscosity of the buffer solution equals the viscosity of water, which is 1.0 mPa s at 20 °C. The resulting reduced loss modulus represents only the contribution of the filaments. The slope of the reduced loss modulus $G'' - \eta_s \omega$ as a function of frequency in a double logarithmic plot in Fig. 4.24 changes from 5/9 in the Rouse-Zimm regime to 3/4 at higher frequencies at which the filament relaxation is determined by the internal fluctuation Kuhn segments. The shortest relaxation time in the Rouse-Zimm spectrum can be extracted from the critical frequency $\omega_0 \approx 40$ rad/s at which the change in slope occurs. A persistence length of $l_p \approx 0.23$ μm was obtained from ω_0 using equation 2.4.

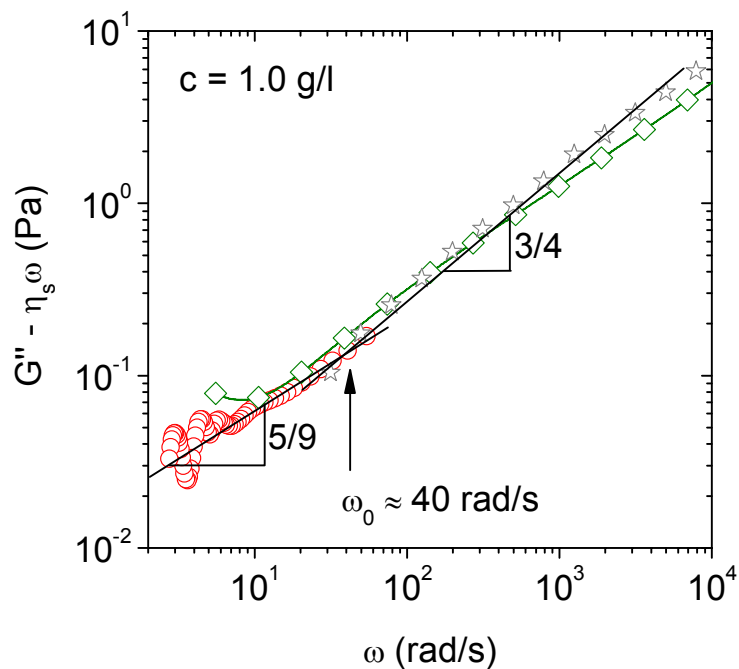


Fig. 4.24 Loss modulus G'' measured by MPT (circles), squeeze flow (stars) and DWS (diamonds) of K8/K18 corrected for the solvent contribution $\eta_s \omega$.

The viscoelastic properties in the high frequency regime at different protein concentrations were systematically characterized using the piezo-driven squeeze flow device. The reduced loss modulus normalized by the protein concentration is shown in Fig. 4.25. All curves collapse and exhibit

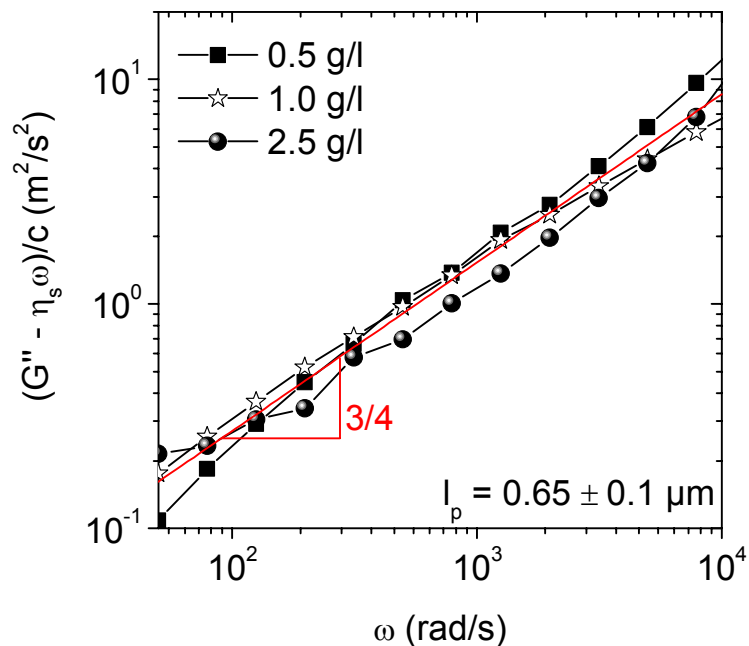


Fig. 4.25 Loss modulus G'' measured by squeeze flow corrected for the solvent contribution $\eta_s \omega$ and normalized by the protein concentration as a function of frequency.

a scaling of $G^* = \omega^{3/4}$. The linear relationship between G^* and c confirms, that single filament properties are probed in this frequency range. Thus, equation 2.5 can be used to calculate the persistence length l_p from these rheological data. An average persistence length of $l_p = 0.65 \pm 0.1 \mu\text{m}$ was obtained by this method.

The persistence length l_p obtained from rheological measurements using two different methods is in the range of the persistence length of $l_p = 0.3 \mu\text{m}$ determined from the curvature of single K8/K18 filaments measured by microscopic methods (Lichtenstern et al., 2012).

In the non-linear regime biological filament networks rupture when a critical maximum strain γ_{max} is exceeded. First, the effect of this disruption on the network properties of K8/K18 filaments has been characterized by performing three consecutive LAOS experiments. Fig. 4.26 shows the apparent storage modulus G' normalized by G' of the mature network obtained after 60 min of assembly. The absolute modulus values of G' in this experiment were measured with cone-plate geometry and are slightly higher than the values obtained with the plate-plate fixture used in most other experiments. This results in different shape of the apparent moduli in the LAOS experiments. However, the results presented are qualitatively similar to the results found using a different rheometer setup.

In the first run the stress amplitude was increased from 0.01 to 10 Pa. This maximum in the stress amplitude was chosen such that the critical strain $\gamma_{max} \approx 1.1$ at which the network ruptures was not reached. Accordingly, the G' data in the second run are essentially the same as in the first run, but now the stress was further increased until the network ruptures. Above this critical strain G' drops drastically and the strain amplitude γ increases by magnitudes. Subsequently, the network was allowed to recover and after 30 min waiting time the G_0 value measured in the first run was reached again. In the subsequent third run, the G' versus γ curve exhibits nearly the same functional form as in the first run confirming the reconstitution of the network.

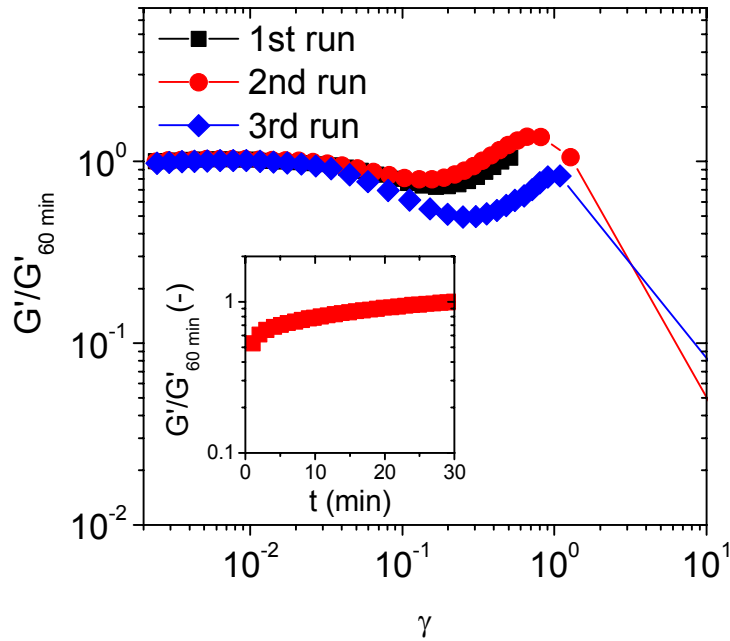


Fig. 4.26 Deformation dependence of storage modulus G' normalized by G' determined after 60 min assembly time prior to the first run for a K8/K18 solution with $c = 0.5$ mg/ml at a frequency of $\omega = 1$ rad/s. The moduli are shown for three subsequent measurements on the same sample. In the first run the maximum strain amplitude was chosen such that the maximum in G' was not yet reached. In the second run, γ was increased until rupture of the sample occurred and the third run was performed after a recovery time of 30 min. Inset: Recovery of the samples between the 2nd and the 3rd run measured at $\hat{\gamma} = 1\%$.

A similar self-healing behavior has been observed for K5/K14 (Ma et al., 1999) and neurofilament networks (Wagner et al., 2007). In contrast, desmin filament networks are irreversibly damaged after exceeding the critical strain γ_{max} and do not recover within waiting times on the order of 30 to 60 min (Schopferer et al., 2009).

The non-linear response at different protein concentrations was characterized by the pre-stress protocol (Fig. 4.27). All analyzed samples exhibit strain stiffening. From the measurements of the differential modulus characteristic values such as the critical strain $\gamma_{crit} = \sigma_{crit}/G_0$ at which the network starts to stiffen, the maximum stress σ_{max} at which the network ruptures, and the highest elasticity K'_{max} were extracted.

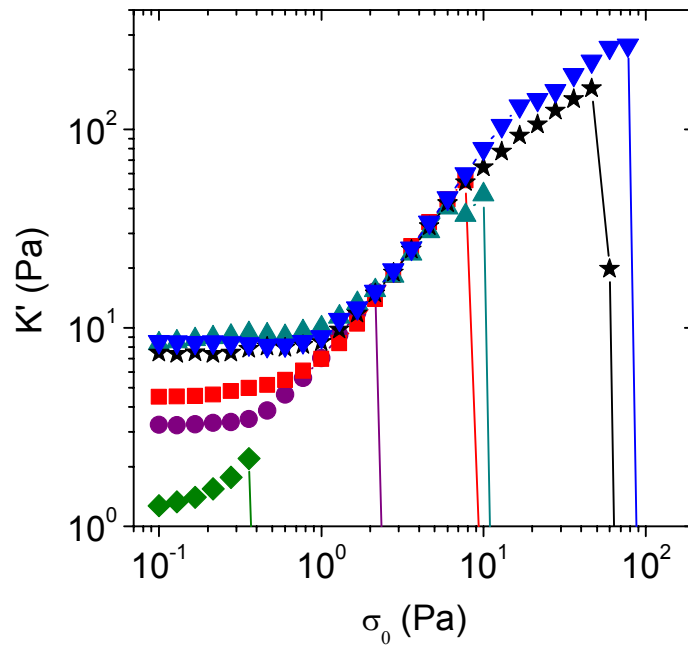


Fig. 4.27 K' versus σ_0 of K8/K18 at concentrations of 0.1 (diamonds), 0.25 (circles), 0.5 (squares), 0.75 (up triangles), 1.0 (stars), and 1.4 g/l (down triangles).

Fig. 4.28 shows the influence of the protein concentration on the critical deformation γ_{crit} . Obviously, $\gamma_{crit} \approx 0.09$ is independent of the protein concentration.

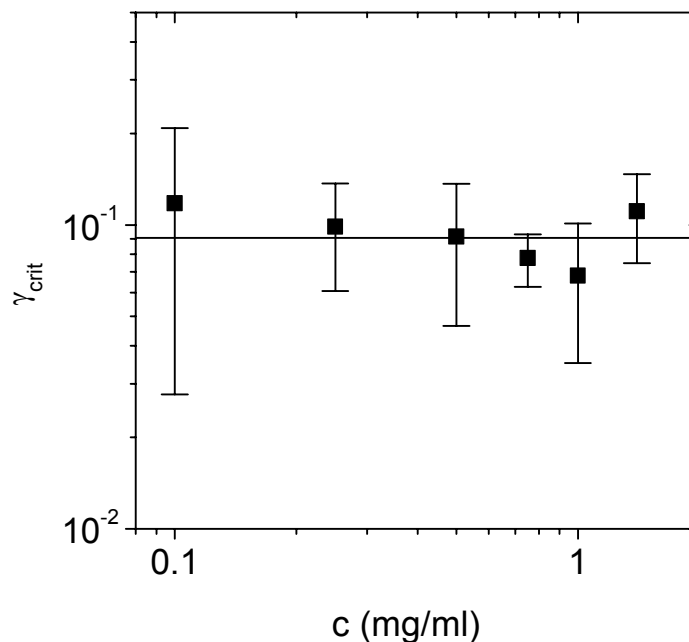


Fig. 4.28 The influence of the K8/K18 concentration on γ_{crit} .

The influence of the protein concentration and on σ_{max} and K'_{max} is shown in Fig. 4.29. In contrast to the linear viscoelastic properties and γ_{crit} , both non-linear quantities increase strongly with protein concentration.

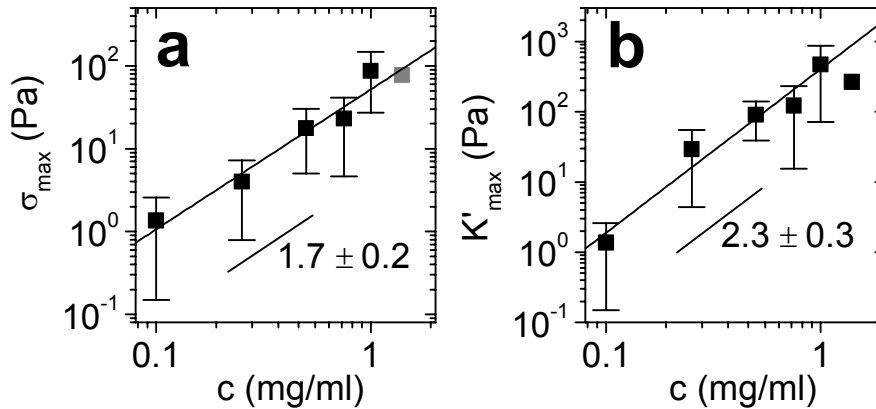


Fig. 4.29 The stress at which the networks ruptures σ_{max} (a) and the maximal elasticity K'_{max} (b) of the network versus K8/K18 concentration.

The data for the differential modulus K' obtained at different protein concentrations result in a master curve when K' is normalized by G_0 and σ_0 by σ_{crit} as demonstrated in Fig. 4.30. The non-linear response is characterized by two scaling regimes $K' \sim \sigma_0^\alpha$ with different exponents α . At intermediate stresses the increase of K' is characterized by $\alpha \approx 1.0$. In the high stress regime the scaling exponent $\alpha \approx 0.6$ is found.

Master curves for normalized K' versus σ_0 data have also been found for other cytoskeletal filament networks but with different α -values and different scaling regimes. Rammensee and colleagues found a single scaling regime with $\alpha = 1$ for neurofilaments (Rammensee et al., 2007). Actin and the rigid cross-linker scruin (Gardel et al., 2004a, 2004b), and neurofilaments with magnesium chloride (Lin et al., 2010b) as well show only a single scaling regime but with an α -value of $3/2$. Vimentin (Lin et al., 2010a, 2010b) and actin cross-linked by the flexible cross-linker filamin (Kasza et al., 2009) show two regimes with a $\alpha = 3/2$ scaling at intermediate stresses and a lower α -value at high stresses. The differential modulus K' of vimentin gradually levels off at high stresses, but actin cross-linked by filamin (Kasza et al., 2009) shows a second regime with a constant slope of $\alpha = 1$.

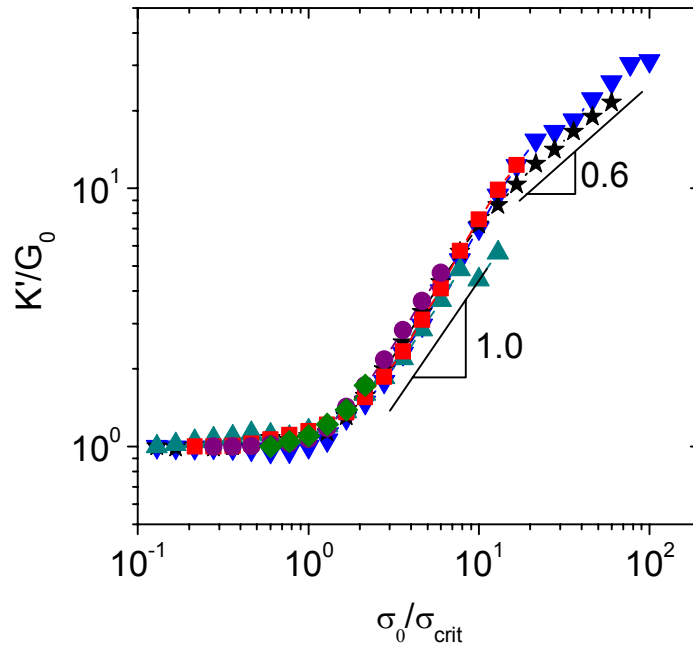


Fig. 4.30 K' and σ_0 normalized by G_0 and σ_{crit} for K8/K18 concentrations of 0.1 (diamonds), 0.25 (circles), 0.5 (squares), 0.75 (up triangles), 1.0 (stars), and 1.4 g/l (down triangles).

On the other hand actin solutions (Semmrich et al., 2007), bundled actin-fascin networks (Lieleg and Bausch, 2007), and actin isotropically cross-linked by heavy meromyosin (Tharmann et al., 2007) show α -values, which depend significantly on parameters such as time scale of the measurement, cross-link density, temperature, ionic strength, filament length, and protein concentration.

4.4.2 Discussion

Pure K8/K18 networks exhibit a predominantly elastic behavior in a broad frequency range without any indication for a cross-over at small frequencies. This gel-like behavior and the range of the dissipation factor between $G''/G' = 0.1$ and 0.2 is typical for chemically or physically cross-linked polymer networks. The dependence of the plateau modulus G_0 on keratin concentration is weak and can be described by a power law $G_0 \sim c^x$ with $x = 0.5 \pm 0.08$. Different theoretical models have been proposed in the literature to describe the relationship between G_0 and the microscopic network and filament features as described in chapter 2.3.

The relevant length scale in all these models is in the range of the mesh size or the length between adjacent cross-links, which are both related to the cross-link density of the network. The scaling exponents of these models range from $x = 1.4$ to 2.5 .

The weak increase of G_0 with protein concentration found for K8/K18 cannot be explained by any of these models. The inconsistency with theoretical models was explained by structural changes of the network (e.g. bundling) (Schopferer et al., 2009), attractive filament-filament interactions (Coulombe et al., 2000; Ma et al., 1999) or a strong elasticity of the air-liquid interface (Yamada et al., 2003). The latter can be excluded here as discussed in chapter 4.4.1. SEM images and MPT experiments show no clear indication for bundling to occur in networks without added salt. This is also confirmed from the constant value of persistence length at different protein concentrations as deduced from high frequency oscillatory squeeze flow measurements (Fig. 4.25). Furthermore, bundling would result in a larger mesh size and in G_0 values lower than expected for networks of individual filaments at high protein concentrations.

Instead, the weak concentration dependence of the modulus observed here is a consequence of the high G_0 values found at low protein concentrations. The experimental data are e.g. much higher than corresponding values for entangled actin solutions at similar length densities (Gardel et al., 2003; Hinner et al., 1998). The plateau modulus G_0 can be directly calculated from the protein concentration using the cubic grid model (equation 2.15). The corresponding values are shown as a dotted line in Fig. 4.22. This theoretical curve exhibits much lower values than the data obtained from shear rheology, e.g. $G_0 \leq 4 \cdot 10^{-3}$ Pa at a concentration of 0.1 g/l.

The plateau modulus can also be assessed by using the affine model for semi-flexible filaments (equation 2.11). The value of G_0 predicted by this model increases with decreasing L_c or increasing protein concentration $c = \rho \cdot \lambda_m$. In addition, the modulus value increases if the bending stiffness $\kappa = k_B T l_p$ increases. The maximum persistence length found for K8/K18 has a value of $l_p = 0.65 \mu\text{m}$ as determined from high frequency oscillatory squeeze flow measurements (Fig. 4.25). A mesh size of $\xi \geq 1 \mu\text{m}$ can be estimated from the MPT experiments at 0.1 g/l protein

concentration (Fig. 4.4). L_c is equal or larger than ζ . For an K8/K18 concentration of 0.1 g/l and mesh size of $\zeta = 1 \mu\text{m}$ the model results in $G_0 \leq 3.5 \cdot 10^{-2} \text{ Pa}$, which is again much lower than the value obtained from shear rheology.

The deviation between data measured by shear rheometry and both model predictions decreases with increasing protein concentration. Therefore, there must be an additional contribution to the free energy of the network to account for the high moduli at low protein concentrations. Following the classical theory describing the swelling of chemically cross-linked networks of flexible polymer chains (Obukhov et al., 1994), this can be explained by an additional contribution from stretched filaments between cross-links. For such networks the cross-link density decreases upon swelling, but the contour length of network strands between adjacent cross-links L_c is constant as illustrated in Fig. 4.31.

The weak influence of polymer concentration on G_0 is a consequence of two competing effects. The cross-link density decreases with decreasing polymer concentration, but this is partly compensated by stretching of polymer strands associated with an increase in conformational free energy. The theory for swollen gels of chemically cross-linked networks of flexible chains predicts $G_0 \sim c^{1/3}$ for a polymer network in a θ -solvents and $G_0 \sim c^{7/12}$ in a good solvent (Obukhov et al., 1994). The latter scaling law is in excellent agreement with our experimental observations shown in Fig. 4.22. Therefore, it can be hypothesized that the number of cross-links in the K8/K18 networks investigated here is approximately independent of the protein concentration and that the filament strands between cross-links are more stretched at lower concentrations.

This explains not only the weak concentration dependency of G_0 , but also the high modulus values at low protein concentrations. The model indicates that the stretched filaments on the SEM images in Fig. 4.4 represent the natural filament conformation within the network.

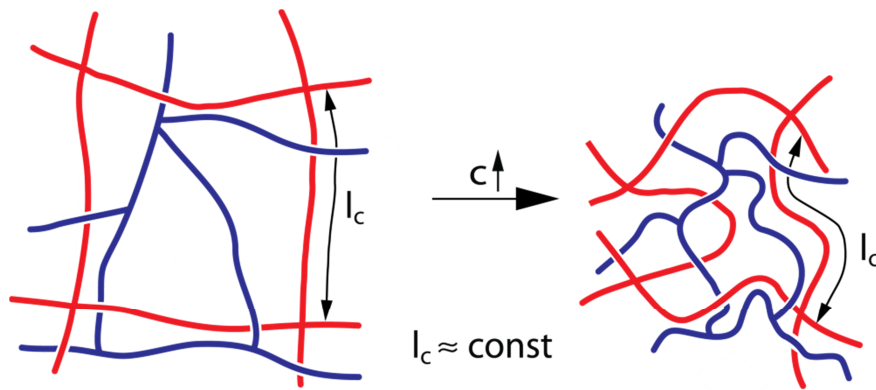


Fig. 4.31 The sketch illustrates the change in the network structure with concentration according to our model.

In contrast, the moduli calculated from MPT data are consistent with the prediction calculated by the cubic grid model (equation 2.15). This is because the particle motion detected in MPT experiments is only sensitive to the network topology and does not sense the entropic contribution of stretched filaments.

The concentration independence of the parameter γ_{crit} , which characterizes the on-set of the non-linear response shown in Fig. 4.28, can also be rationalized based on the assumption of increasing filament stretching at decreasing protein concentrations. According to equation 2.12, the onset of the non-linear response of semi-flexible filaments at γ_{crit} is directly proportional to the filament contour length between adjacent cross-links L_c if the elasticity is entropic in origin and bending stiffness is constant (MacKintosh et al., 1995). High frequency measurements show that the persistence length and consequently the bending stiffness does not depend on the protein concentration (Fig. 4.25). The constant value of γ_{crit} confirms that L_c is independent from the protein concentration for the K8/K18 networks investigated here.

Only literature data for vimentin and neurofilament networks in the presence of divalent ions show that L_c determined from γ_{crit} decreases with protein concentration according to a power law $L_c \sim c^{-0.4}$, which is close to the scaling for the mesh size of a cubic grid of rigid filaments $\xi \sim c^{-0.5}$ (Lin et al., 2010b).

The evaluation of the differential storage modulus K' as a function of pre-stress σ_0 at different protein concentrations demonstrates that the

characteristic values σ_{max} and K'_{max} depend strongly on protein concentration (Fig. 4.29). This is in contrast to the weak concentration dependency of G_0 and γ_{crit} . According to Storm et al. (2005) σ_{max} is mainly controlled by the strength of the bonds between filaments and K'_{max} by the strain stiffening mechanism and the compliance of filaments in axial direction.

The α -value characterizing the slope of the K' versus σ_0 curve (Fig. 4.30) is always below $3/2$ as expected for networks with irreversible cross-links, i.e. bonds of infinite strength (Gardel et al., 2004a; Kroy and Glaser, 2007). Within the framework of the GWLC model, the master curve obtained after normalizing the differential modulus K' with G_0 and the pre-stress σ_0 with σ_{crit} in Fig. 4.30 indicates a universal strain stiffening mechanism with a constant and finite strength of sticky contacts. The low α -value and the decreasing slope of K' may be explained by a successive breaking of weak network bonds.

The change in slope of the master curve at high pre-stresses might also originate from two different bond types with different strength of attractive interactions or from an extension of the individual filaments due to the high stresses prior to rupture. The decreasing slope of the K' versus σ_0 curves at high pre-stresses found for vimentin was also attributed to stretching of the polymer backbone (Lin et al., 2010b). This hypothesis is further supported by mechanical studies on single filaments of neurofilaments, desmin, keratin 5 and 14 (Kreplak et al., 2005). Accordingly, atomic force microscopy has revealed that IFs, i.e. keratins K5/K14 and desmin filaments as well as authentic neurofilaments, can be stretched up to threefold of their initial contour length before rupture.

4.5 Influence of magnesium chloride on K8/K18 networks

Here, the influence of magnesium chloride at on K8/K18 networks at a constant protein concentration of 0.5 g/l in 10 mM Tris-HCl (pH 7.4) has been investigated using linear and non-linear shear rheology. The considered magnesium chloride concentration range was limited to concentrations equal or below 1.5 mM because at higher concentrations of magnesium chloride the assembly is so fast that aggregated filaments plug the pipette tip before the sample was filled into the rheometer.

4.5.1 Results

The frequency dependency of the moduli G' and G'' measured by linear oscillatory shear rheology for K8/K18 networks with 1.5 mM magnesium chloride and without salt is shown in Fig. 4.32. The added divalent salt has no effect on these linear viscoelastic properties. Accordingly, the magnesium chloride concentration has also no influence on the plateau modulus G_0 as shown in Fig. 4.33.

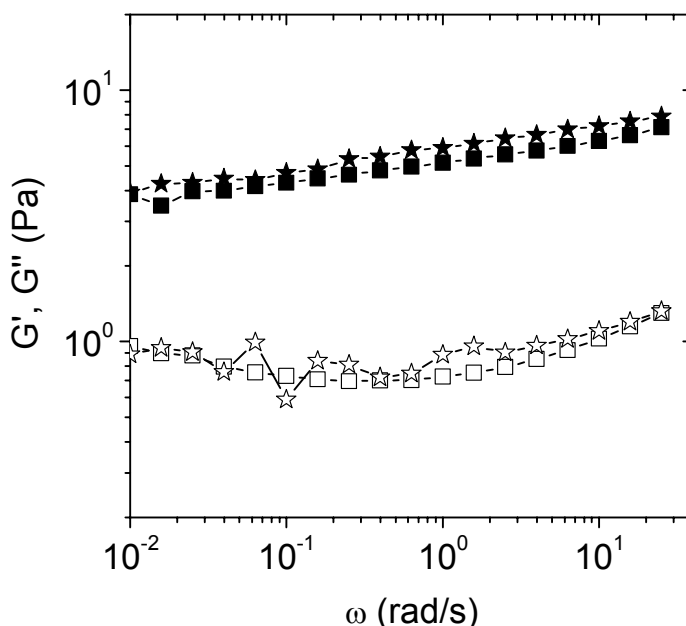


Fig. 4.32 Frequency dependency of the storage modulus G' (closed symbols) and the viscous modulus G'' (open symbols) in the linear viscoelastic regime of K8/K18 filaments at concentrations of 0.5 g/l without salt (squares), and with 1.5 mM magnesium chloride (stars).

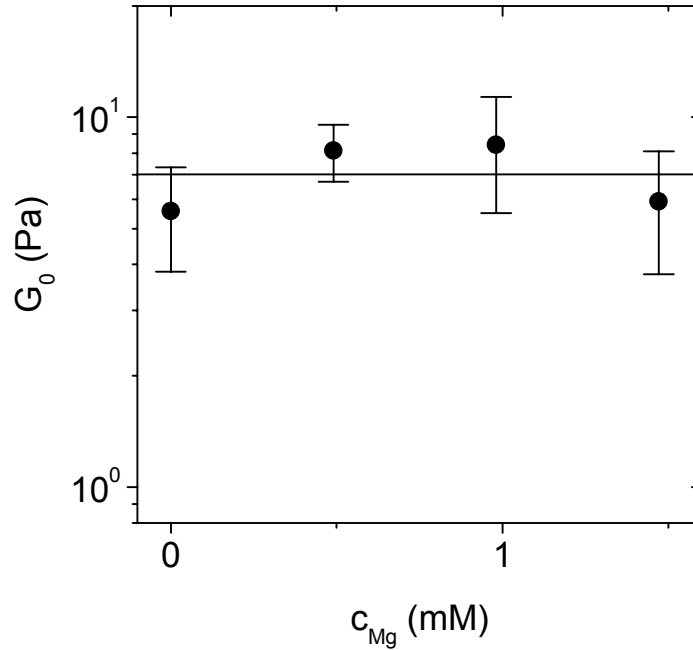


Fig. 4.33 The plateau modulus G_0 at a frequency of 6.3 rad/s versus magnesium chloride concentration at a K8/K18 concentration of 0.5 g/l.

In contrast to the findings presented here, Lin and co-workers have observed a scaling of $G_0 \sim R^{0.6}$ for vimentin and neurofilaments, where R is the ratio of the molar concentrations of divalent cations to IF proteins (Lin et al., 2010b). The moduli of K8/K18 obtained from microrheological experiments (Leitner et al., 2012) increase even stronger with increasing magnesium chloride concentration. However, the calculation of the bulk modulus of a gel or network sample from MPT results is based on the assumption that the tracer particles move in a homogeneous continuum, i.e. the MSD data show a Gaussian distribution with $\alpha_2 \approx 0$ (Oppong et al., 2006). This is not the case here when salt is added (see Fig. 4.5) and therefore the macroscopic data cannot be compared with the results of Leitner et al. (2012).

The onset of the non-linear response at γ_{crit} is also independent of the magnesium chloride concentration as shown in Fig. 4.34. For networks of vimentin and neurofilament networks a scaling of $\gamma_{crit} \sim c_{\text{Mg}}^{-0.2}$ with magnesium ion concentration has been reported (Lin et al., 2010b).

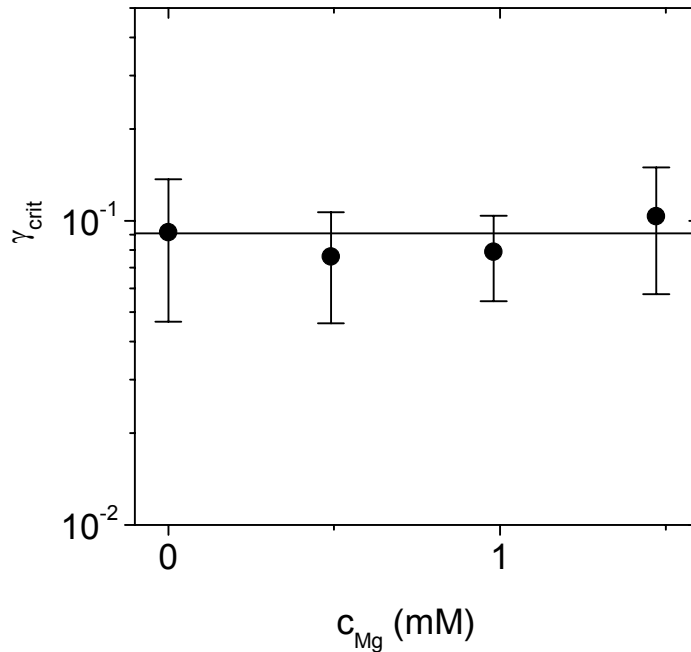


Fig. 4.34 The influence of the magnesium chloride concentration on γ_{crit} at a protein concentration of 0.5 g/l.

On the other hand, the magnesium chloride concentration strongly influences stress at which the networks ruptures σ_{max} and the maximal elasticity K'_{max} (Fig. 4.35a and b). The increase of both parameters with magnesium chloride concentration can be described by power-law exponents between 1.3 and 1.4. This strong effect of divalent ions on these parameters was also found for the wild type of vimentin (Lin et al., 2010a).

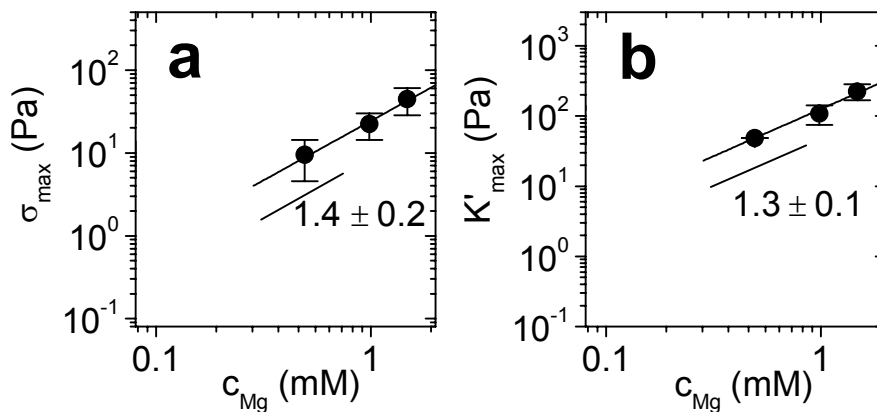


Fig. 4.35 The stress at which the networks ruptures σ_{max} (a) and the maximal elasticity K'_{max} (b) of the network versus $MgCl_2$ concentration at a K8/K18 concentration of 0.5 g/l.

The data for the differential modulus K' obtained at different magnesium ion concentrations result in a similar master curve as for

different protein concentrations when K' is normalized by G_0 and σ_0 by σ_{crit} as demonstrated in Fig. 4.36. The shape of the master curve is similar to K8/K18 networks without additional salt. The corresponding raw data are shown as inset.

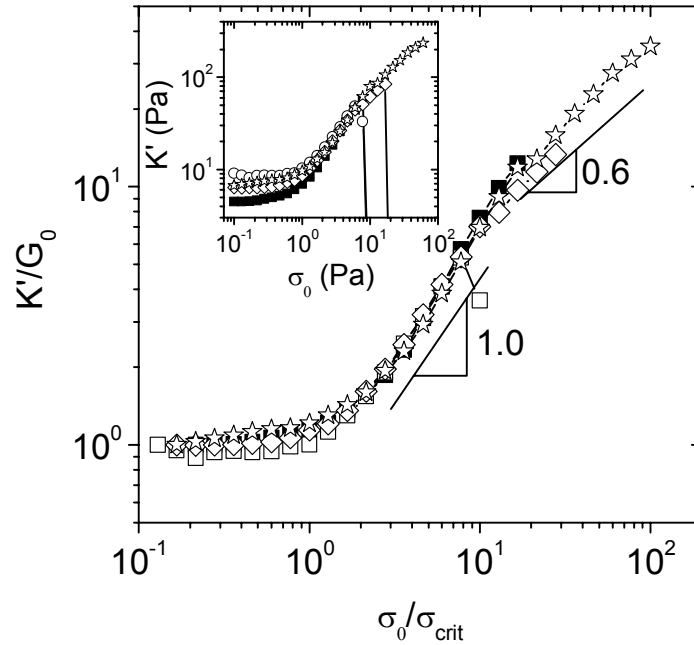


Fig. 4.36 K' and σ_0 normalized by G_0 and σ_{crit} . Inset: Raw data used for the master curve. Symbols represent magnesium chloride concentrations of 0 (squares), 0.5 (open squares), 1.0 (open diamonds), and 1.5 mM (open stars) at a K8/K18 concentration of 0.5 g/l.

4.5.2 Discussion

The constant elasticity G_0 and the constant critical deformation γ_{crit} of K8/K18 networks with increasing magnesium chloride concentration in Fig. 4.33 and Fig. 4.34 indicate a constant mesh size $G_0 \sim \xi^{-3}$ (equation 2.8) and a constant length between cross-links $\gamma_{crit} \sim L_c$ (equation 2.12) with $L_c \approx \xi$. This seems to be in contradiction to the results from electron micrographs and MPT experiments shown in Fig. 4.4 revealing changes in the network structure due to bundling at high magnesium chloride concentrations. A quantitative evaluation of the mesh size from SEM images also suggest that the mesh size exhibits a scaling of $L_c \sim c_{Mg}^{-0.39}$ with increasing magnesium ion concentration (Leitner et al., 2012). The results for K8/K18 contradict also the shear rheological results for vimentin

and neurofilament networks, which indicate a decrease in L_c with increasing magnesium ion concentration (Lin et al., 2010b).

As shown above, the high moduli include a contribution from strong non-equilibrium stretching of filaments between cross-links. This contribution to the moduli decreases with increasing cross-link density. This effect seems to balance the contribution of increasing cross-link density by magnesium chloride. The linear dependency of γ_{crit} from L_c seems to be too small to be captured by our measurement in the narrow concentration range investigated here.

The only parameters, which change significantly, are the stress at which the network ruptures σ_{max} and the maximal elasticity K'_{max} of the network. This strong effect of the magnesium concentration on these parameters was previously attributed to cross-links by divalent cations (Lin et al., 2010a). According to the GWLC model, the master curve indicates a constant ε -parameter, which corresponds to constant bond strength between filaments even in the presence of divalent ions.

4.6 Influence of the non-ionic surfactant Triton X-100 on the viscoelastic properties of IF networks

Yamada and co-workers (2003) analyzed the effect of Triton X-100 on the linear viscoelastic response at a constant K8/K18 concentration of 1 g/l. The authors showed that the macroscopic viscoelastic properties of K8/K18 drastically drop if a critical amount of the non-ionic surfactant Triton X-100 (TX-100) was added to the assembly buffer but that the addition of the surfactant has no effect on negative stained electron micrographs and on pelleting experiments. The changes in the viscoelastic response were attributed to a decrease in the interfacial elasticity.

In this study it was shown, that the shear rheological properties are not influenced by the surface treatment or the ratio of the air-liquid interface to sample volume (chapter 4.3). Thus, influences of the interfacial elasticity could be excluded. Here, the effect on the surfactant on K8/K18 networks was investigated using linear and non-linear shear rheology, high frequency oscillatory squeeze flow, MPT, DWS, and electron microscopy. The results for K8/K18 were compared to those obtained for IF networks assembled from the tailless mutants K8 Δ T and K18 Δ T as well as vimentin.

4.6.1 Results

In the first step, the critical surfactant concentration at which the shear rheological properties change dramatically was determined. Fig. 4.35 shows the plateau modulus of K8/K18 at a protein concentration of 0.5 g/l as a function of the surfactant concentration for two different gap widths and two different plate diameters. At a gap width of 0.12 mm the critical concentration is about 0.3 mM (0.2 %) but only 0.08 mM (0.005 %) at a 1.2 mm gap width. However, measurements with different gaps or different geometries give the same results if the Triton X-100 concentration is above the critical threshold. In the following, all experiments were conducted above the critical Triton X-100 concentration.

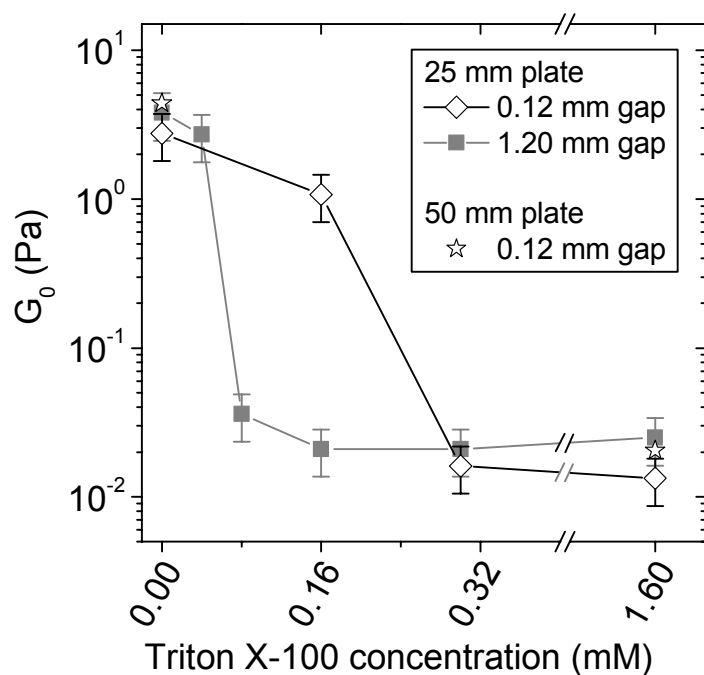


Fig. 4.37 The influence of the surfactant concentration on plateau modulus G_0 at $\omega = 1$ rad/s and at a K8/K18 concentration of 0.5 g/l (9.8 μ M).

The frequency dependency of the storage modulus G' and the loss modulus G'' of the bulk K8/K18 network without and with Triton X-100 at the same protein concentration are shown in Fig. 4.38. Both networks exhibit predominantly elastic, gel-like behavior in the frequency range accessible by rotational rheometry. In addition, the modulus G' is in both cases approximately frequency independent and corresponds consequently to the plateau modulus G_0 . For comparison it is shown that the surfactant has no effect on the modulus of a DNA dissolved in the same buffer as used for K8/K18. The DNA concentration of 7.5 g/l at the respective length of 1.02 μ m (3 kbp) was chosen to be well above the critical overlap concentration of 1.3 g/l at which the DNA molecules start to entangle (Mason et al., 1998). However, the relaxation time of this solution is still short enough such that classical shear rheometry only covers the terminal flow regime with $G'' > G'$.

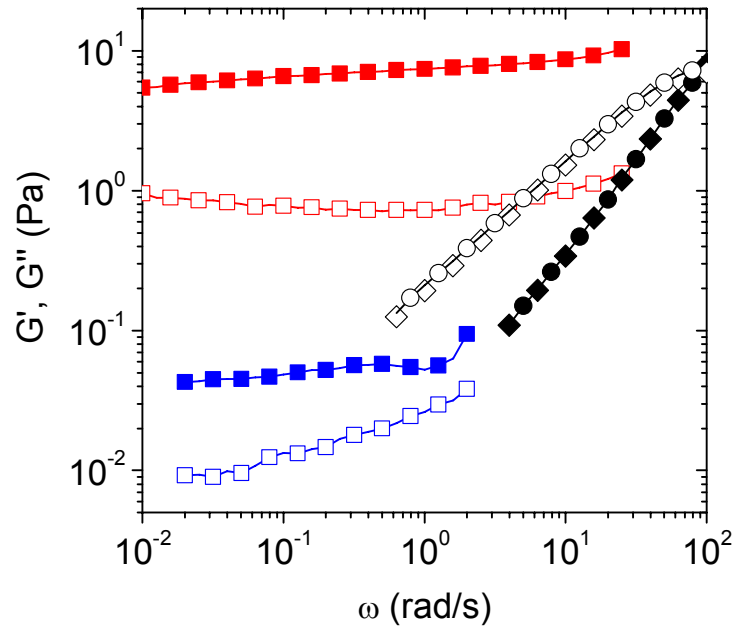


Fig. 4.38 Frequency dependency of G' (closed symbols) and G'' (open symbols) without surfactant (red symbols) and with 0.01 % Triton X-100 (blue symbols) of K8/K18 (squares) at $c = 1.0$ g/l. As reference the results for DNA at $c = 7.5$ g/l (black symbols) are shown without surfactant (circles) and with 0.01% Triton X-100 (diamonds).

Transmission electron micrographs of the negatively stained K8/K18 filaments without surfactant (Fig. 4.39a) and in the presence of 0.01 % Triton X-100 (0.16 mM) (Fig. 4.39b) show homogeneous long filaments. The K8/K18 network without surfactant seems to look more dense, likely because of slight differences of the filament deposition on the grid as discussed by Lichtenstern et al. (2012), but in general, these images do not reveal qualitative differences in filament assembly or network structure due to the addition of surfactant.

MPT microrheology was used to probe the influence of the surfactant on the network microstructure in its natural aqueous environment without further sample preparation. Particles ($d = 0.52$ μm) slightly bigger than the mesh size at the respective protein concentration $c = 1.0$ g/l were used and the corresponding MSD data for networks without surfactant and in the presence of Triton X-100 are presented in Fig. 4.39c and Fig. 4.39d. The MSD data for both cases follow the same trend and have approximately the same magnitude. At long lag times τ the MSD approaches a time independent plateau showing that the particles are trapped by the network.

The insets show the histogram of the MSDs after a time interval of $\tau = 1$ s. Not only the average MSD, but also the distribution of MSDs is very similar for both networks and the addition of Triton X-100 does not show any significant effect. Similar distributions of the MSDs were observed for homogeneous F-actin solutions (Apgar et al., 2000).

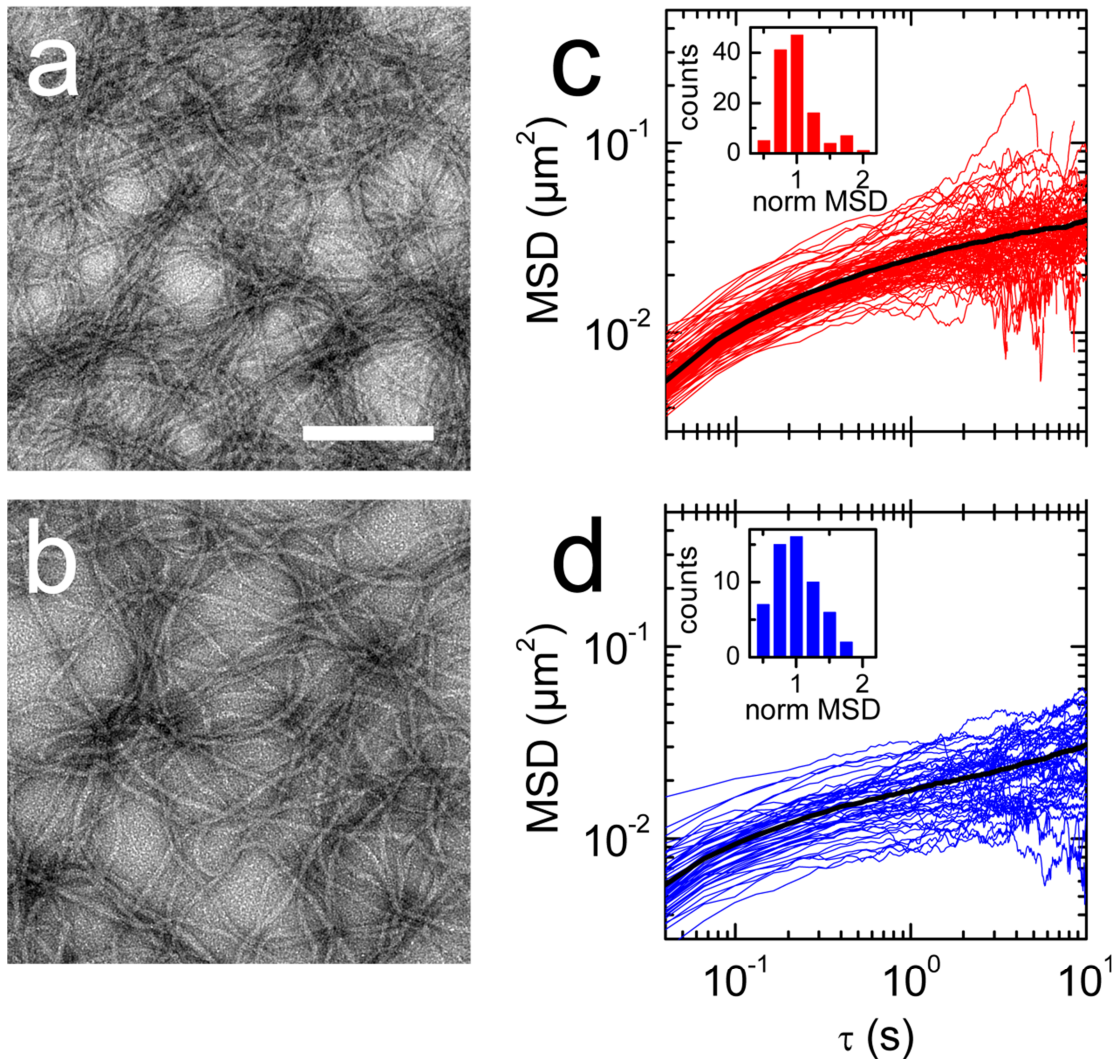


Fig. 4.39 Influence of the surfactant Triton X-100 on network structure of K8/K18 characterized by transmission electron microscopy and MPT. Electron micrographs of K8/K18 without surfactant (a) and with 0.01 % Triton X-100 (b). Scale bar represents 200 nm. (c) and (d) show the MSDs without surfactant and with 0.01% Triton X-100 at $c = 1.0$ g/l as a function of time τ . The black line illustrates the ensemble average of the MSDs. The insets show the histogram of the MSDs normalized by the averaged MSD after $\tau = 1$ s.

Triton X-100 has also no influence on the viscoelastic properties in the high frequency regime measured by squeeze flow (Fig. 4.40). Hence, the persistence length l_p remains unaffected by the surfactant.

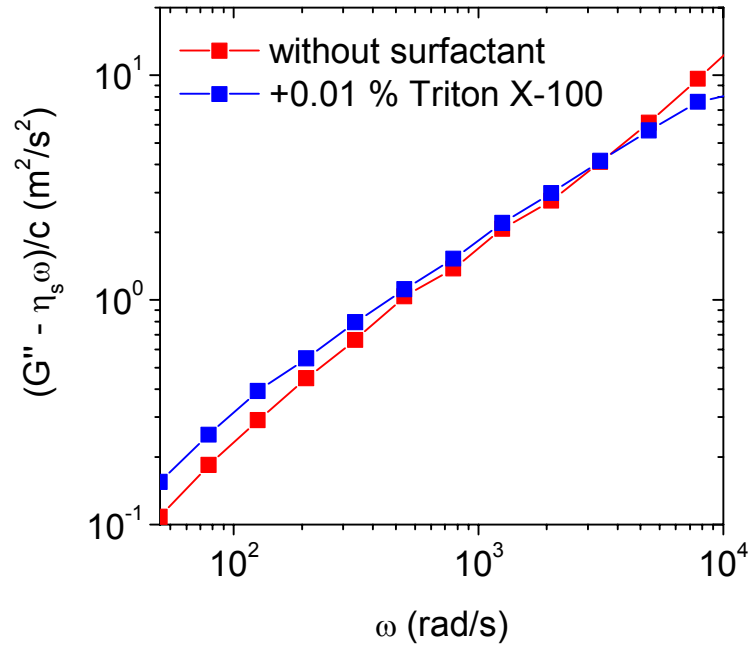


Fig. 4.40 High frequency squeeze flow measurements without surfactant and with Triton X-100 at a K8/K18 concentration of 0.5 g/l.

To further investigate the influence of the surfactant on the network properties the linear viscoelastic properties were characterized at different protein concentrations. Corresponding plateau modulus G_0 taken at $\omega = 1$ rad/s are shown in Fig. 4.41. In addition to shear rheological data, G_0 derived from MPT experiments are plotted in the graph. In the presences of Triton X-100 the magnitude of G_0 decreases and the scaling of $G_0 \sim c^x$ increases from $x = 0.5 \pm 0.1$ to 1.9 ± 0.2 . Most strikingly, the data from MPT experiments without surfactant are close to the results from mechanical shear rheometry with Triton X-100.

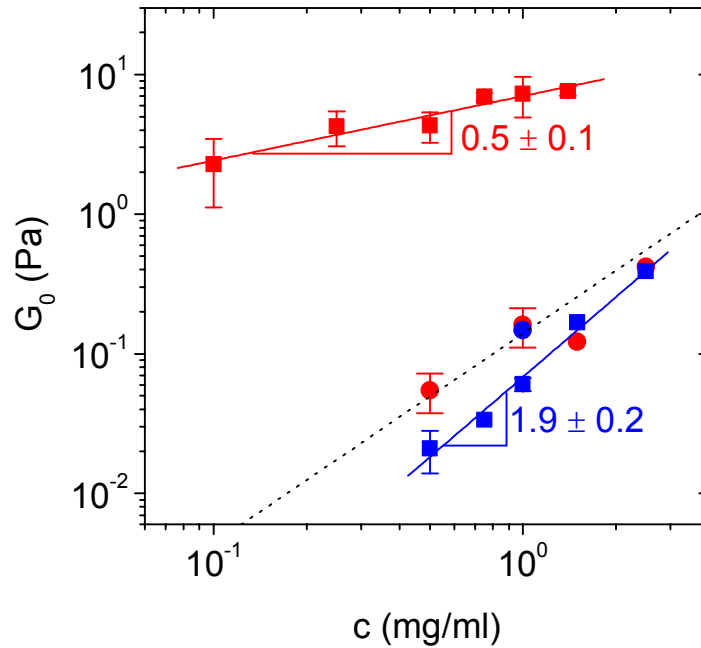


Fig. 4.41 The plateau modulus G_0 measured by shear rheology (squares) and by MPT (circles) without surfactant (red) and with 0.01 % Triton X-100 (blue) versus K8/K18 concentration. The dotted line shows the results obtained by the cubic grid model in equation 2.15.

Fig. 4.42 compares the mesh size ξ of K8/K18 and literature data for vimentin, desmin and actin calculated from the protein concentration assuming a cubic grid (equation 2.6) with the apparent $\xi = (k_B T / G_0)^{1/3}$ calculated from G_0 (equation 2.8). The length densities of the filaments used in Fig. 4b are $\lambda_m = 6.31 \cdot 10^{-11}$ g/m for vimentin (Herrmann et al., 1999), $\lambda_m = 9.80 \cdot 10^{-11}$ g/m for desmin (Herrmann et al., 1999), and $\lambda_m = 2.66 \cdot 10^{-11}$ g/m for actin (Steinmetz et al., 1998). The data calculated for networks of K8/K18 filaments with surfactant and actin filaments are close to the diagonal line, showing that both methods result essentially in the same mesh size ξ . But for K8/K18 without surfactant, vimentin, and desmin the apparent mesh size obtained from G_0 is very low compared to the cubic grid model.

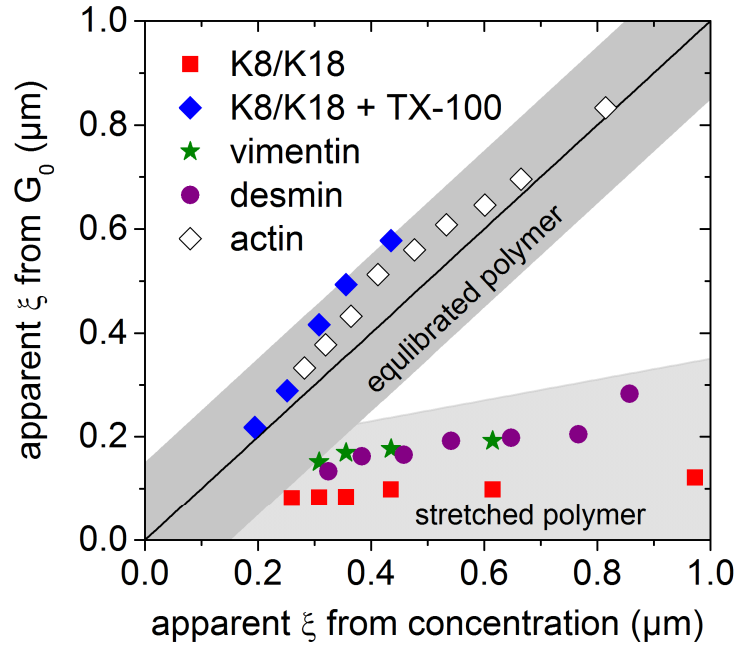


Fig. 4.42 Comparison of the apparent mesh size ξ of different biological filament networks calculated from protein concentration using the cubic grid model (equation 2.6) with the mesh size calculated from the plateau modulus $\xi = (k_B T / G_0)^{1/3}$. The data used for K8/K18 is taken from Fig. 4.41. Data for vimentin and desmin were taken from (Schopferer et al., 2009). Actin data was extracted from Fig. 3 in (Hinner et al., 1998).

The dark grey zone illustrates that the simplistic model can be used to calculate the mesh size of networks from G_0 with an uncertainty of $\pm 0.15 \mu\text{m}$. This holds if the filaments are in thermal equilibrium. The light grey area shows that this is not the case for many IF networks.

Oscillatory squeeze flow described above and DWS have been used to expand the frequency range for characterization of the linear viscoelastic network properties up to 10^6 rad/s . Fig. 4.43 shows the results of all rheological methods without surfactant and the shear rheological data with Triton X-100. The data illustrates that the data measured by oscillatory shear rheology with surfactant agree well with the high frequency squeeze flow and the microrheological data. The combination of all methods allows for characterization of the viscoelastic properties of K8/K18 networks over a frequency range of six orders of magnitude. This is the first time that the linear viscoelastic properties of an IF network have been determined over such a broad frequency range using four independent methods.

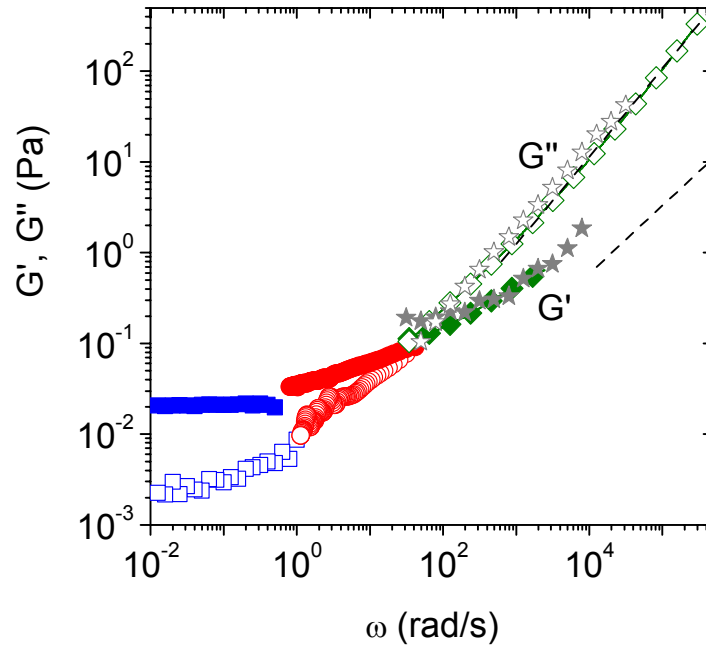


Fig. 4.43 G' (closed symbols) and G'' (open symbols) measured by shear rheology (blue squares), MPT (red circles), DWS (green diamonds), and squeeze flow (grey stars) as a function of frequency ω . The K8/K18 concentration is 0.5 g/l. Black dashed lines: Theoretical values calculated by the model of Gittes & MacKintosh 1998 with a persistence length of $l_p = 0.3 \mu\text{m}$ from Lichtenstern et al. (2012).

The tailless variants K8 Δ /K18 Δ T were characterized to investigate the influence of the tail domain on the viscoelastic properties. IF proteins without tail domain still form bona fide filaments (Bär et al., 2010; Hatzfeld and Weber, 1990). As reference, networks from the IF protein vimentin were analyzed. A higher concentration was chosen for vimentin because it consists of 32 instead of 16 molecules per cross-section as in K8/K18 filaments (Herrmann et al., 1999). Tab. 3 compares the effect of surfactant on G_0 for K8/K18, K8 Δ /K18 Δ T, and vimentin. Without surfactant the plateau modulus of K8 Δ T/K18 Δ T is close to the results for the wild-type. Similar results were obtained for networks from tailless desmin (Bär et al., 2010), tailless vimentin (Lin et al., 2010a) and tailless keratin 14 (Bousquet et al., 2001). Vimentin networks without surfactant exhibits also a plateau modulus similar to that of the other samples. In the presence of 0.1 % Triton X-100 the plateau modulus of all samples decrease dramatically, showing that the phenomenon is not unique to K8/K18. This decrease is even more pronounced for K8 Δ /K18 Δ T and vimentin than for K8/K18.

Tab. 3 Influence of Triton X-100 on G_0 at $\omega = 0.5$ rad/s.

IF protein	concentration	without surfactant	0.1 % Triton X-100
	g/l (μM)	Pa	Pa
K8/K18	0.50 (9.8)	$3.9 \pm 0.8^*$	$0.017 \pm 0.004^*$
K8 Δ T/K18 Δ T	0.45 (9.8)	1.5	0.0025
vimentin	0.90 (16.8)	1.8	0.0022

*exp. errors calculated from st. dev. of at least three independent measurements

The effect of Triton X-100 seems also not to be unique to this specific surfactant. The addition of 0.01 % of non-ionic surfactant Tween 20 reduces the plateau modulus G_0 to 0.035 Pa at a K8/K18 concentration of 0.45 g/l using the same measuring conditions. This value is close to the result for K8/K18 with Triton X-100.

The torques measured by the rheometer to determine the moduli of the samples with surfactant in oscillatory shear are close to the resolution limit of the device. The noise level of the rheometer characterized by the standard deviation of the torque signal during air measurements was 8.6 ± 0.2 nNm. In this work, the torques of K8/K18 at $c \geq 0.5$ g/l with Triton X-100 were always above 12 nNm at $\gamma \leq 0.2$ using a 25 mm parallel plate geometry. The moduli of vimentin with Triton X-100 were measured using a 50 mm plate and a shear amplitude of $\gamma = 0.15$ to obtain torques above the noise level of the device (> 10 nNm).

In all previous experiments the surfactant was added to the assembly buffer before the network was constituted. In order to show in which way the surfactant affects mature IF networks, the networks were treated with surfactant containing buffer after an assembly time of 60 min. For these experiments, the IF networks were assembled in the rheometer as in chapter 4.1. After 60 minutes the rim of the rheometer plate was carefully treated with a buffer containing 10 mM Tris-HCl (pH 7.4), 0.5 mM DTT and 0.1 % Triton X-100 and the same volume as the sample volume. The viscoelastic properties during the assembly and after addition of the assembly buffer were followed by small amplitude oscillatory shear at a frequency of 1 rad/s.

The results for K8/K18, K8 Δ T/K18 Δ T at a concentration of 9.8 μM , and 16.8 μM vimentin are shown in Fig. 4.44. The modulus of all IF

networks drops after treatment with the surfactant. However, the final moduli after 120 min are much higher than for the networks, which were assembled in the presence of the surfactant presented in Tab. 3.

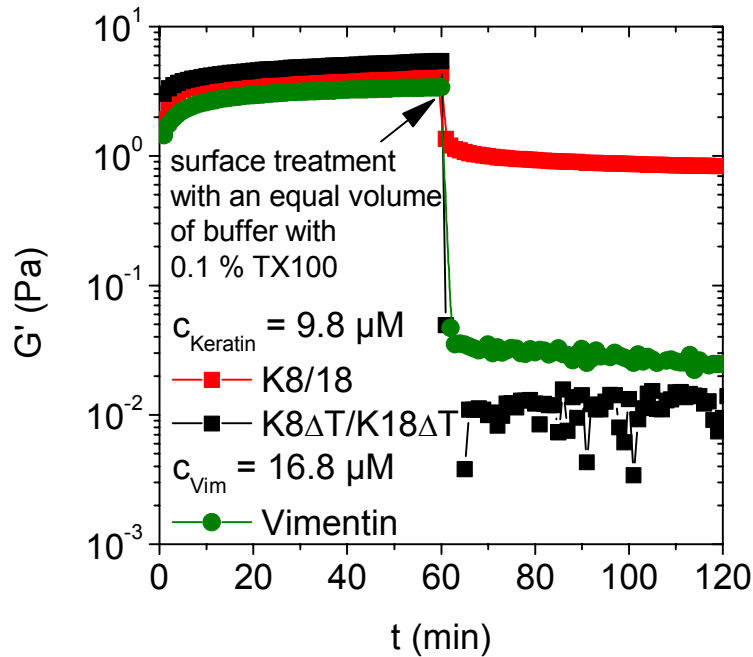


Fig. 4.44 Kinetics of network formation and subsequent destruction of sticky contacts due to treatment with buffer containing 0.1 % Triton X-100 characterized by the elastic modulus obtained from small amplitude oscillatory shear.

The non-linear viscoelastic properties of IF networks were characterized to probe in which way the surfactant influences strain stiffening. These properties were measured by application of a constant strain rate of $\dot{\gamma} = 0.1 \text{ s}^{-1}$ and measurement of the resulting shear stress σ as shown in Fig. 4.45a. Without surfactant all IF networks exhibit an increase of stress with increasing strain as expected for elastic materials. After reaching a maximum stress at γ_{max} the network ruptures and the stress drops. The IF solutions with Triton X-100 exhibit σ values at least one order of magnitude lower than the corresponding surfactant-free networks and the stress response is approximately strain independent similar as for viscous fluids.

Strain stiffening is characterized by the increase in slope of the stress-strain curve. To quantify strain stiffening the differential modulus $K = d\sigma/d\gamma$ was calculated from the stress-strain curves in Fig. 4.45a. The results presented in Fig. 4.45b illustrate that strain stiffening of K8/K18 is much more pronounced than for vimentin networks. In contrast,

K8 Δ T/K18 Δ T does not show strain stiffening. In the presence of Triton X-100 the stress response is strain independent and hence the differential modulus is zero.

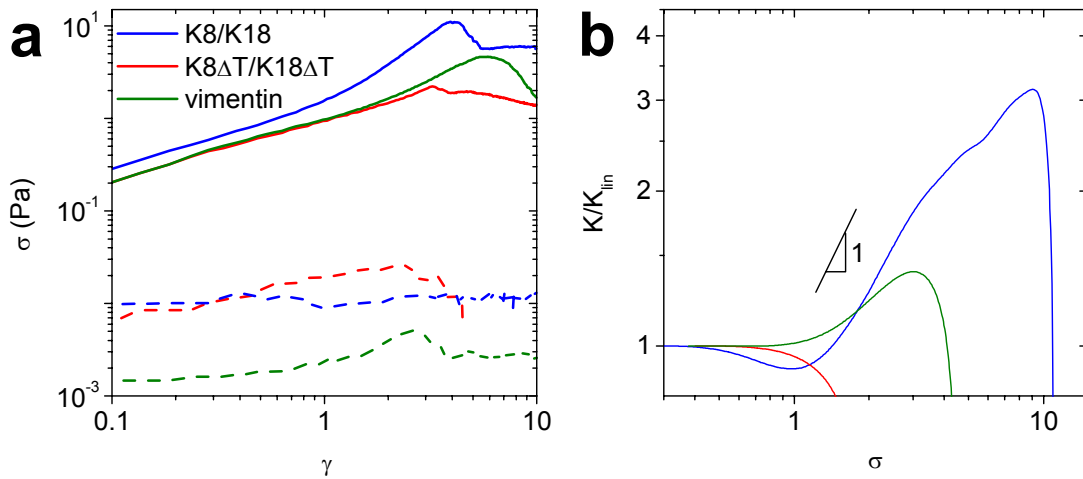


Fig. 4.45 Shear stress σ as a function of deformation γ of K8/K18, K8 Δ T/K18 Δ T at a concentration of 9.8 μ M, and vimentin (16.8 μ M) by measuring the stress response without surfactant (continuous lines) and with 0.1% Triton X-100 (dashed lines). Measurements were conducted at a constant strain rate of $\dot{\gamma} = 0.1 \text{ s}^{-1}$ (a). The normalized differential modulus $K = d\sigma/d\gamma$ derived from the stress-strain curves normalized by the differential modulus at small deformations K_{lin} as a function of deformation (b).

4.6.2 Discussion

The macroscopic mechanical properties of K8/K18 networks change dramatically above a critical concentration of Triton X-100. The critical concentration increases with decreasing gap width. This can be explained by the increase in the ratio of the external sample interface to sample volume. Surfactants tend to adsorb on interfaces. The total external interface consists of the air-liquid interface and the interface between the rheometer fixture and sample. The surface area of a Triton X-100 molecule on an air-liquid interface is 0.6 nm² (Janczuk & Bruque 1995). The measurements were conducted using a plate with a diameter of 25 mm without overfilling the gap. At a Triton X-100 concentration of 0.01 % and a gap width of 0.12 mm 30 % of the surfactant is needed to saturate the external interfaces assuming that the surface area per molecule is the same on all external interfaces. In contrast, only 3 % of the surfactant is needed

to saturate the external interface at a gap width of 1.2 mm. The critical Triton X-100 concentration at which G_0 drops increases drastically from 0.005 % (0.08 mM) to 0.019 % (0.3 mM) by changing the gap from 1.2 mm to 0.12 mm. This is in accordance with the rough approximation for the surfactant needed to saturate the external surfaces.

The critical surfactant concentration does also allow to estimate the number of Triton X-100 molecules per ULF needed to reduce the attractive interactions among filaments. At both gap widths less than 16 % of the added surfactant is needed to saturate the external interface. Already 130 surfactant molecules per ULF (length: ~ 45 nm) are sufficient to reduce the viscoelastic properties drastically at a gap width of 1.2 mm.

The addition of Triton X-100 has no significant influence on the particle motion observed in microrheological experiments. The narrow distribution of the MSD from particle tracking experiments with normalized standard deviations below 33 % after a lag time of 1 s shows that the homogeneity is similar to pure F-actin networks (Tseng and Wirtz, 2001) without any indication for bundling as observed for actin with the bundling protein fascin (Apgar et al., 2000) or actin cross-linked by α -actinin (Tseng and Wirtz, 2001). Moreover, the surfactant has no influence on the rheological properties at high frequencies and the visual impression of the K8/K18 filaments on electron micrographs (Fig. 4.38, Fig. 4.39a, and b). Hence, the surfactant does not affect network parameters, such as filament diameter, persistence length, network heterogeneity, or mesh size.

The characteristic plateau modulus G_0 obtained from small amplitude oscillatory shear decreases by orders of magnitude and is in the range expected for an equilibrated network without contributions from stretched filaments when Triton X-100 is added. The scaling of G_0 with concentration ($x = 1.9 \pm 0.2$) is captured by various theoretical models for networks of flexible or semi-flexible polymers, which predict scaling exponents between 1.4 and 2.5 (de Gennes, 1979; Hinner et al., 1998; Kroy and Frey, 1996; MacKintosh et al., 1995). In addition, the concentration dependence and the absolute values of G_0 show reasonable quantitative agreement with the simple estimate given by the cubic grid model shown as dotted line in Fig. 4.41. This indicates that only the cross-links contribute an energy of $k_B T$ to the free energy of the network. The additional

contribution from stretched filament strands seems to vanish upon addition of the surfactant. It should also be noted, that the motion of the tracer particles is determined by the mesh size of the network, but not by additional contributions to the free energy density, like e.g. the stretched filament strands. Accordingly, there is a strong discrepancy between the G_0 values from MPT and mechanical shear rheometry for untreated K8/K18 networks, but these values are in excellent agreement for the surfactant treated networks.

The mesh size predicted from rheology for K8/K18 networks with Triton X-100 and actin networks (Gardel et al., 2003; Hinner et al., 1998) is close to the mesh size calculated by assuming a cubic grid of filaments (Fig. 4.42). In contrast, data for IF networks without additional surfactant is well below the diagonal line, indicating an additional free energy contribution due to stretched filaments.

The elastic modulus decreases less if the surfactant Triton X-100 is added to the mature network. Hence, only a fraction of the stretched filaments can equilibrate upon addition of the surfactant.

The findings outlined above referring to the effect of added surfactant on the viscoelastic properties of IF networks can be rationalized taking into account that the hydrophobic parts of the surfactant molecules will adsorb onto hydrophobic regions of the keratin filaments, thus providing a steric stabilization. This prevents the filaments from approaching each other close enough to encounter strong attraction. Accordingly, the formation of permanent cross-links is suppressed and equilibration of the stretched filaments between cross-links is enabled. The surfactant does not change the number of contact points, which is determined by the protein filament length density and is well estimated by the simple cubic grid model. Accordingly, the mesh size is unaffected by the addition of surfactant. Finally, the linear viscoelastic response of the networks in the high frequency regime is not affected by the surfactant, since it is determined by the stress relaxation of short filament strands and therefore, independent of the interactions among filaments at their contact points.

This basic idea is captured by the glassy wormlike chain model (GWLC) described in chapter 2.5. The GWLC model describes the

attractive interactions by reversible breakable cross-links. The bound state is energetically favorable because its inner energy is lower than that of the unbound state. The fraction of bound to unbound filaments is determined by the difference in inner energy U between both states. To unbind or bind a filament an energy barrier ($\varepsilon - U$) characterized by the stickiness parameter ε has to be overcome and this determines the binding/unbinding kinetics. For K8/K18 the gain in inner energy due to filament-filament bonds is so high that two filaments always form bonds when they are close enough together. The unbinding rate approaches zero because of the high energy barrier ε . Therefore, many filament strands between such contact points are not in thermal equilibrium and the entropically unfavorable stretched conformation of filaments between adjacent cross-links leads to an additional contribution to the free energy. Within the framework of the GWLC model the steric stabilization of filaments provided by Triton X-100 is expressed as a reduction of the ε parameter. The corresponding increase in the binding and unbinding rates enables the filaments to attain their thermodynamically favorable conformation.

The plateau modulus value of K8 Δ T/K18 Δ T without surfactant is close to that of the wild-type. Similar results were obtained for tailless desmin (Bär et al., 2010), tailless vimentin (Lin et al., 2010a) and tailless keratin 14 (Bousquet et al., 2001). Thus, the attractive hydrophobic interactions required to maintain the stretched filament strands between contact points and hence responsible for the high plateau moduli are located in the central rod domain (Fig. 4.46). Five particular hydrophobic amino acids clusters are found in the rod region of the K8 and K18 coiled-coil dimer, and in addition one cluster each in the head domains close to the beginning of the rods (Fig. 4.47).

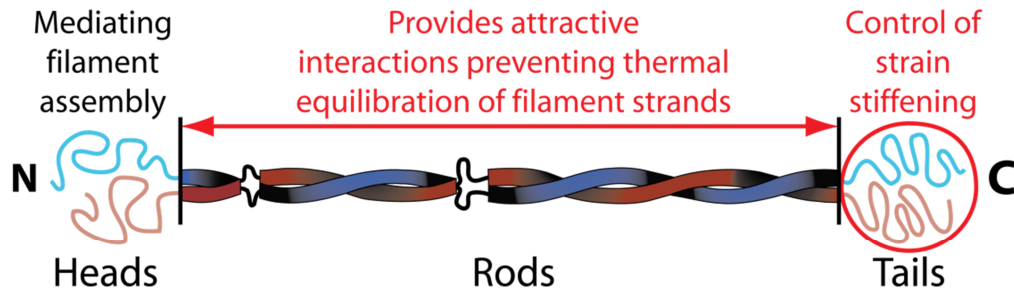


Fig. 4.46 Schematic representation of the heterodimeric K8/K18 complex and the protein domains responsible for the high elasticity in the linear viscoelastic regime and strain stiffening. Illustration adapted from (Herrmann and Aebi, 1998).

In the presence of the surfactant the plateau modulus of K8 Δ T/K18 Δ T and vimentin are nearly one order of magnitude lower than for K8/K18 indicating a reduction of mesh size. This might be attributed to a larger fraction of short filaments or dangling ends not contributing to the entanglement network, which is further supported by the high value of G''/G' , which demonstrates pronounced viscous losses during oscillatory shear of these networks. The estimated isoelectric points of K8 Δ T and K18 Δ T are 4.89 and 5.07. They are lower than the estimated isoelectric points of the wild-type with 5.26 for K8 and 5.11 for K18. Hence, the net negative charge of K8 Δ T/K18 Δ T at pH = 7.5 is higher than for the wildtype. Also vimentin exhibits strong electrostatic repulsion allowing strain stiffening only at high salt concentrations (Schopferer et al., 2009). These repulsive interactions may also lead to a reduction of the cross-link density.

K8/K18 and vimentin show strain stiffening, which is characteristic for many biological gels (Storm et al., 2005). Strain stiffening mainly originates from a strong non-linear increase of the entropic contribution to the free energy of the network with increasing deformation when the filament strands between cross-links or sticky contacts are stretched. (Gardel et al., 2004b). Strong attractive interactions at filament contact points are a prerequisite for strain-stiffening. This phenomenon is completely suppressed upon addition of Triton X-100. Within the framework of the GWLC model the strength of these cross-links is characterized by the stickiness parameter ε . The slope of the differential

Head
MS**F**T**R**R**T****F**S**T**N**R**S**I**G**S**V**O**A**P**S**Y**G**A**R**P**V**S**A**S**V**Y**A**G**A**G**G**S**G**S**R**I**S**V**S**R**S**T**S**F**R**G**G**M**G**S**G**I**A**T**G**I**A**G**M**G**G**I**O**N**
MS**I**R**V**I**O**K**S**I**K****V**S**T**S**G**P**R**A**F**S**S**R**S**I**T**S**G**P**G**S**R**I**S**S**S**S**F**S**R**V**G**S**S**N**F**R**G**G**L**G**G**G**Y**G**G**A**S**G**M**G**G**I**T**A**V**T**V**N**O**S**I**L**S**P**V**L**E**V**D**P**N**I**O**A**V**R**T**Q

Rod

Coil 1A
EK**E**T**M**O**S**I**N**D**R**L**A**S**Y**L**D**R**V**R**S**L**E**T**E**N**R**L**E**S**K**I**R**E**H**
EK**E**Q**I**K**T**L**N**N**K**E**A**S**F**I**D**K**V**R**F**L**E**Q**O**N**K**M**L**E**T**K**W**S**L**L

Linker I1
LE**R**K**K**G**P**Q**V**R**D**
QO**Q**K**T**A**R**S**N**M

Coil 1B
WS**H****F**K**T**I**E**D**L**R**A**Q**I**F**A**N**T**V**D****A**R**I**V**L**Q**I**D**N**A**R**L**A**D**D**F**R**V**K**Y**E**T**E**L**A**M**R**O**S**V**E**N**D**I**H**G**L**R**K**V**I**D**D**I**N**I**T**R**I**Q**L**E**T**E**I**E**A**L**K**E**E**L**L**M**K**K**N**H**E**E**E**V**K**G**L**
DN**M**E**S**T**I**N**N**L**R**Q**L**E**T**L**G**O**E**K**L**K**L**E**A**L**G**N**M**O**G**L**V**E**D**F**K**V**K**Y**E**D**E**L**N**K**R**I**E**M**E**N**E**V**L**I**K**K**D**V**D**E**A**Y**M**N**V**E**L**E**S**R**L**E**G**L**T**D**E**I**N**F**L**R**O**L**Y**E**E**I**R**E**L**

Linker I12
QA**Q**I**A**S**S**G**L**T**V**V**D**A**P**K**S**Q
QS**Q**I**S**D**T**S**V**V**L**S**M**D**N**S**R**S**L**

Coil 2A
DL**A**K**I**V**A**D**I**R**A**Q**Y**D**E**L**A**R**K**
DM**D**S**I**L**A**F**V**K**A**Q**Y**E**D**L**A**N**R**

Linker I2
NR**E**E**L**D**K**Y
SR**A**E**A**E**S**M

Coil 2B
WS**Q**I**E**S**T**T**V**T**T**O**S**A**E**V**G**A**E**T**T**L**T**E**L**R**R**T**V**O**S**L**E**I**D**S**M**R**N**L**E**A**S**I**E**N**S**L**R**E**V**E**A**R**Y**A**M**O**M**Q**I**N**G**I**L**H**E**S**E**L**A**O**T**R**A**E**S**O**R**A**O**E**Y**E**A**L**I**N**I**K**V**L**E**A**E**I**A**T**Y**R**R**L**L**E
WI**K**I**V**E**L**Q**S**L**A**G**K**H**G**D**L**R**R**K**T**E**L**S**E**M**N**R**N**I**S**R**Q**A**E**L**E**G**L**K**G**O**F**A**S**I**E**A**L**I**A**D**E**O**R**G**I**A**I**K**D**A**N**K**L**S**E**L**E**A**L**O**R**A**K**O**D**A**R**Q**L**R**E**Y**O**E**L**M**V**K**A**L**D**I**E**L**A**T**Y**R**K**L**L**E

Tail
DG**E**D**F**N**I**G**D**A**L**D**S**S**N**S**M**Q**I**O**K**T**T**R**R**I**V**D**G**K**V**S**E**T**N**D**I**K**V**L**R**H
GE**S**S**R**L**E**S**G**M**O**N**S**I**H**T**K**T**T**S**G**Y**A**G**G**L**S**A**Y**G**G**L**T**S**P**G**L**S**V**S**L**G**S**S**F**G**S**G**A**G**S**S**S**F**S**R**T**S**S**S**R**A**V**V**V**K**K**I**E**T**R**D**G**K**I**V**S**E**S**S**D**V**L**P**K**

Fig. 4.47 Amino acid sequence alignment of the keratin assembly partners K18 (blue letters) and K8 (green letters).

The order of the subdomains is as reported in Figure 1 of (Herrmann and Aebi, 2004).

Hydrophobic amino acids in the non- α -helical head and tail domains are indicated in red (Kyte and Doolittle, 1982).

Significant hydrophobic motifs in these domains are underlined. In the rod domain, the α - and d -heptad positions are highlighted in yellow; these amino acids are responsible for the formation of a coiled-coil dimer from two individual α -helices.

modulus $\alpha = dK/d\sigma$ characterizing the change of the differential modulus with stress increases with increasing ε and approaches a limiting value of $\alpha = 3/2$ for irreversible cross-links ($\varepsilon \rightarrow \infty$) (Semmrich et al., 2007). The results presented in Fig. 4.45b show, that $\alpha \approx 1$ for K8/K18. Similar results were obtained by a different measuring protocol (Fig. 4.30). Both results indicate a strong but finite attractive interaction at filament contact points. Furthermore, the interaction strength is weaker for vimentin than for K8/K18. This is presumably due to the strong electrostatic repulsion among filaments partly compensating the attractive hydrophobic or van der Waals attractions because strain stiffening in vimentin only occurs at high salt concentrations (Schopferer et al., 2009) when the range of these electrostatic repulsions is strongly reduced and sticky contacts can form.

No strain stiffening is observed for K8 Δ T/K18 Δ T. In this case sticky contacts exist and are strong enough to prevent thermal equilibration of the filament strands between contact points, which results in the high G_0 values, but the attractive interactions are not strong enough to withstand the high stresses occurring in the non-linear deformation experiments. The strong influence of the tail domain on strain stiffening was also found for K14 (Bousquet et al., 2001), vimentin (Lin et al., 2010a), and desmin (Bär et al., 2010) showing, that the protein sequence motifs providing the strong attraction at filament contact points are located in the tail with its high fraction of hydrophobic amino acids (Fig. 4.46 and Fig. 4.47).

5 Open questions and outlook

5.1 Influence of cross-linking agents on IF networks

Intermediate filaments form additional cross-links in the presence of external cross-linking agents such as divalent cations (Lin et al., 2010b), plectin (Steinböck and Wiche, 1999), or desmoplakin (Smith and Fuchs, 1998).

The influence of magnesium chloride on the macrorheological properties of K8/K18 filament networks was already investigated here (see chapter 4.5). The linear viscoelastic properties measured by shear rheometry are unaffected by magnesium cations up to concentrations of 1.5 mM. The data interpretation is difficult because of the experimental error and the narrow concentration range. The extension of the concentration range would facilitate a clear evidence for the influence of magnesium chloride. However, the maximum in the magnesium concentration investigated here is limited by the preparation protocol because the K8/K18 filaments aggregate and plug the pipette tip at salt concentrations above 1.5 mM. The addition of highly concentrated magnesium buffer solutions to mature homogeneous network similar as in Fig. 4.44, would allow investigating high magnesium concentrations at defined conditions. The use of this assembly protocol should be considered in future projects.

In this study it was shown that the mechanical properties of intermediate filament networks can be explained by cross-links due to attractive interactions and a contribution of stretched filaments to the free energy even in the absence of these external cross-linking agents. The strength of these interactions can be strongly reduced by the addition of the non-ionic surfactant Triton X-100. To separate the intrinsic properties of the IF networks from the contribution of external cross-linking agents, further experiments should investigate the effect of divalent cations and crossbridging proteins in the presence of Triton X-100.

5.2 Influence of the pH on the plateau modulus of K8/K18

The assembly of K8/K18 filaments starts by decreasing the pH or increasing the salt concentrations. During the assembly the length of the filament increases by end-to-end fusion. Yamada et al. concluded from electron micrographs and from the soluble protein fraction observed in a pelleting assay that the filament length can be controlled by the pH value (Yamada et al., 2003).

The viscoelastic properties of K8/K18 are approximately independent of the pH value (Yamada et al., 2003). This observation was explained by the formation of aggregates at the air-liquid interface. In this study, it was shown that the viscoelastic properties are not influenced by the interfacial elasticity (see chapter 4.3.1). However, preliminary experiments confirm the results by Yamada and co-workers (Fig. 5.1). K8/K18 forms predominantly elastic networks even at a pH = 9.0 at which the classical theory predicts the presence of soluble tetrameric complexes (Herrmann and Aebi, 2004). Further investigations are needed to clarify this aspect.

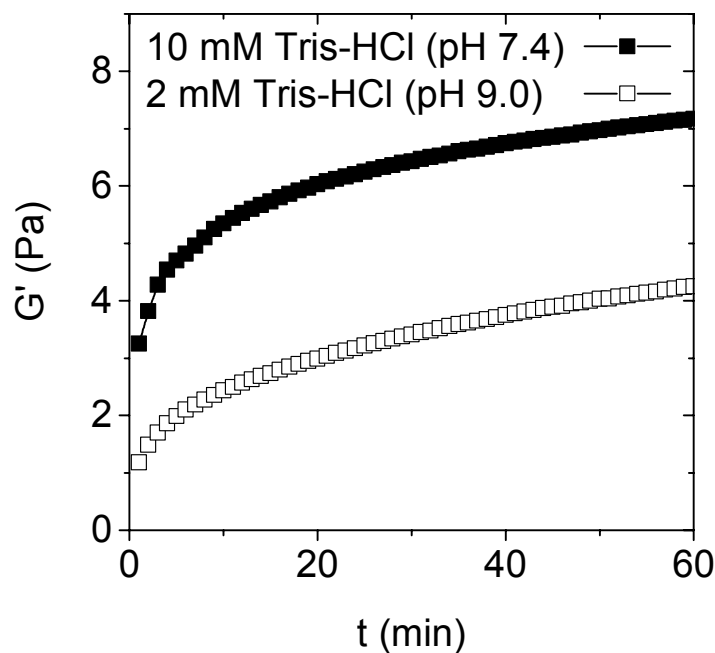


Fig. 5.1 Time evolution of G' during the assembly of 0.45 g/l K8/K18 at different pH 7.4 and pH 9.0 measured at a frequency of 1 rad/s.

5.3 Imaging of IF networks

The origin of the rheological properties can be clarified by correlating images of IF networks with the rheological measurements. This was successfully done for bundled actin networks (Shin et al., 2004). The difficulties of microscopic methods arise from the resolution needed to image single filaments and the artifacts from sample preparation.

Electron microscopy allows to resolve single filaments but for SEM and TEM the filaments are treated with aggressive chemicals, dehydrated, and stained. Cryo-TEM avoids artifacts from dehydration, fixation, and staining. Filaments on cryo-TEM images appeared to be more stretched than on TEM images (Kirmse et al., 2010). Cryo-TEM experiments at different protein concentrations would allow the analysis of the conformation of filaments at different protein concentration if artifacts from the freezing process could be avoided.

Fluorescence microscopic methods allow to image filaments with a diameter of 10 nm in their natural aqueous environment (Winheim et al., 2011). A disadvantage of the method is that the filaments have to be tagged with a fluorescence dye, which may influence the network properties. Another issue is the time scale of the measurement in relation to the thermal fluctuations of the filaments. In order to distinguish two filaments, the distance has to be larger than the optical resolution limit of 220 nm. The resolution can be increased using methods such as Stimulated Emission Depletion (STED) microscopy, which selectively deactivates fluorophores. Preliminary experiments using STED microscopy show that the dynamics of single filaments are too fast compared to the timescale of the scanning process. Only bundles at high magnesium chloride concentration could be imaged (Fig. 5.2). Further improvements of these methods are required to image single filament networks.

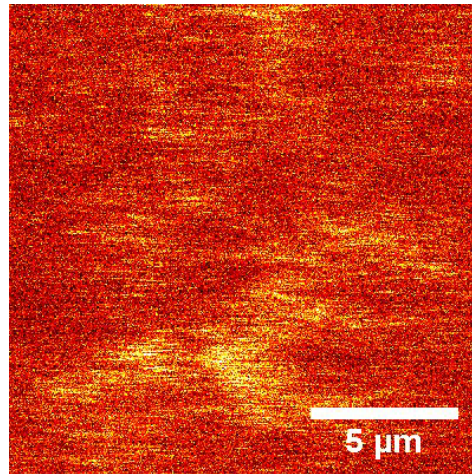


Fig. 5.2 STED image of cysteine mutated K8 tagged with Alexa 647 (label efficiency: 61 %) and K18 in 10 mM Tris-HCl (pH 7.4) and 1.5 mM MgCl₂.

6 Summary

Intermediate filaments (IF) networks have characteristic mechanical features such as a high elasticity and a weak concentration dependency of the shear modulus at small deformations as well as a pronounced strain stiffening at large deformation even in the absence of additional cross-linking agents. The origin of these properties has been investigated here. In detail, the viscoelastic properties of IF networks assembled from keratin 8 (K8) and keratin 18 (K18) at standard buffer conditions using 10 mM Tris-HCl (pH 7.4), with additional MgCl_2 , or with the non-ionic surfactant Triton X-100 have been studied comprehensively using shear rheology, high frequency oscillatory squeeze flow, and optical microrheology. The results have been compared to IF networks assembled from the tailless mutant K8 Δ T/K18 Δ T and the well characterized vimentin. In addition, various characteristics of K8/K18 networks have been investigated e.g. the kinetics of the network formation, the network structure, the network homogeneity, the network recovery after rupture, the persistence length, and the mesh size.

The kinetics of network formation of K8/K18 characterized by small amplitude oscillatory shear rheology is similar to that found for vimentin and desmin networks (Schopferer et al., 2009). The networks already exist when measuring the first data point after 1 min. After 20 min at least 85 % of the G' value finally obtained after 60 min is reached. The network formation process and the absolute values of the linear viscoelastic moduli are almost the same at 20 °C and at 37 °C. The microrheological characterization of network formation by multiple particle tracking (MPT) exhibits a qualitatively similar change in the viscoelastic properties with time as bulk rheology.

The network structure was analyzed using scanning electron microscopy (SEM) and particle tracking microrheology at different protein and different magnesium chloride concentrations. The mesh size of the networks without added salt can be well described by the geometric mesh size of a cubic grid of rigid filaments. Hence, the mesh size ζ is close to the filament length between adjacent cross-links L_c . At a protein concentration of 1.0 g/l the network structure appears bundled on scanning electron

micrographs. However, the homogeneity measured by the non-Gaussian parameter α_2 and the mesh size determined for this concentration by particle tracking experiments indicate that these bundles are an artifact from sample preparation. On the other hand, the addition of magnesium ions at concentrations of 1.5 mM clearly results in bundled structures as confirmed by SEM images as well as by the distribution of mean squared displacements (MSDs) observed by multiple particle tracking experiments. A complete sedimentation of the proteins after centrifugation was observed after addition of 1.5 mM magnesium chloride, which can also be explained by an increase in heavier structures due to bundling.

Variation of the measurement conditions revealed that the linear and non-linear shear rheological properties are not affected by artifacts from the air-liquid interface, wall slip or the filling process of the rheometer.

The comparison of the different protocols to characterize the non-linear rheological properties shows that differential modulus measurements are more appropriate than classical amplitude sweep experiments. The protocol allows an easy data interpretation without sophisticated data analysis and errors due to the aperiodic response signal. The differential modulus can be measured by superposition of a small oscillatory stress and a steady pre-stress σ_0 or by application of a constant shear rate and measurement of the resulting stress. The evaluation of the superimposed oscillatory signal resulting in K' or the derivative of the strain-stress curve $K = d\sigma/d\gamma$ give approximately the same result even though the K8/K18 networks exhibit significant creep during the superimposed oscillatory shear experiment.

The characterization of K8/K18 networks at different protein concentrations show that even at protein concentrations as low as $c = 0.1$ g/l an unexpected high frequency independent storage modulus G' is observed. This so-called plateau modulus G_0 depends only weakly on protein concentration ($G_0 \sim c^{0.5}$) and the critical deformation γ_{crit} at which the non-linear response sets in is independent of protein concentration. In analogy to the classical theory for swollen networks of flexible polymers these findings can be rationalized assuming that the cross-link density decreases with decreasing IF concentration, but that the filament contour length between cross-links is independent of the protein concentration. Thus filaments are more stretched at lower protein concentrations and the

according increase in conformational energy partly compensates the decrease in free energy related to the change of cross-links density. The predicted scaling of $G_0 \sim c^{0.58}$ for a cross-linked network of flexible polymers swollen in a good solvent (Obukhov et al., 1994) is in excellent agreement with our experimental findings.

The networks rupture when a critical strain is exceeded, but recovers and exhibits its initial viscoelastic response after a “healing” time of about 30 min. Other characteristic parameters of the non-linear network response are the stress σ_{max} at which the network ruptures and the corresponding differential modulus K'_{max} . These quantities strongly increase with increasing protein concentration. All data collapse onto a master curve when K' is normalized by G_0 and the underlying steady pre-stress σ_0 by the critical stress σ_{crit} at which non-linear response sets in. Two scaling regimes $K' \sim \sigma_0^\alpha$ are observed with $\alpha \approx 1$ at intermediate stresses and $\alpha \approx 0.6$ at high stresses. These scaling exponents are significantly lower than the value $\alpha \approx 3/2$ predicted for permanently cross-linked networks of semiflexible filaments and may be rationalized within the framework of the glassy wormlike chain (GWLC) model assuming sticky contacts with a finite and constant bond strength. The weak increase and the change in slope of the differential modulus are in this case a result of the successive failure of network bonds. The second regime with a lower slope could also be due to the existence of two types of sticky filament contacts with different bond energies or by the compliance of the individual filaments occurring at large deformations. Further structural investigations on networks exposed to mechanical stresses are required to clarify this aspect.

The plateau modulus G_0 is independent of the divalent magnesium cation concentration suggesting, that the increased number of filament junctions revealed by electron microscopy goes along with a decreasing contribution of stretched filaments. Both effects balance and G_0 remains constant. The changes in cross-link density due to divalent magnesium cations appear not to be strong enough to be captured by the γ_{crit} measurements. In the non-linear regime the stress σ_{max} at which the network ruptures and the corresponding modulus K'_{max} strongly increase with increasing magnesium chloride concentration. Similar results were obtained for the effect of magnesium ions on vimentin networks (Lin et al.,

2010a). The shape of the stiffening curve is the same as without salt indicating a similar bond strength in both cases.

Our electron microscopy, MPT, and high frequency rheology studies confirm that K8/K18 forms homogeneous networks of single filaments without and even with added non-ionic surfactant Triton X-100. In the presence of Triton X-100 the modulus drops by orders of magnitude and exhibits a strong concentration dependence. Both, the absolute values of G_0 and a scaling law with $G_0 \sim c^x$ the scaling exponent $x = 1.9 \pm 0.2$ describing the concentration dependence are well approximated by a simple cubic grid model ($x = 1.5$) calculating the number of contact points per volume from the filament length density and assigning a free energy contribution of $k_B T$ to each contact point in the network. The scaling exponent also agrees fairly well with theoretical predictions for networks of semi-flexible or flexible polymers ($1.4 \leq x \leq 2.5$). The stretched filament conformation suggested to explain the high values of G_0 at low concentrations and its weak dependence on protein concentration require strong attractive interactions among filaments at these contact points, also called sticky contacts. The surfactant strongly reduces the strength of the attractive interactions and allows the filaments to equilibrate. The shear rheological data with Triton X-100 agrees also with the data from high frequency squeeze flow, diffusing wave spectroscopy, and MPT experiments, which are not affected by the surfactant. This is the first time that the frequency dependency of G' and G'' could be measured between frequencies of 10^{-2} and 10^6 rad/s using four independent methods. The stiffness of K8/K18 filaments determined from the high frequency regime is between $l_p = 0.23$ and $0.65 \mu\text{m}$.

The moduli of K8 Δ T/K18 Δ T, vimentin, and also for wildtype and tailless desmin (Bär et al., 2010) are similar to those of K8/K18 indicating that sticky contacts are present in these IF networks, too and that the respective attractive interactions originate from the central rod domain of the protein. The decrease of the plateau modulus G_0 in the presence of surfactant is stronger for K8 Δ T/K18 Δ T and vimentin than for the wildtype K8/K18. This might be due to a larger fraction of short filaments or dangling ends not contributing to the network or due to stronger electrostatic repulsion between the filaments.

The plateau modulus is higher if the surfactant is added to the mature network than if the network is assembled in the presence of Triton X-100 because not all the filament-filament bonds of the mature network can be resolved.

Strain-stiffening is stronger for K8/K18 than for vimentin, which might be due to electrostatic repulsion among vimentin filaments weakening the sticky contacts. K8 Δ T/K18 Δ T still exhibits predominately elastic behavior and a modulus similar to the wildtype protein, but does not show strain stiffening. Similar behavior was found comparing wildtype and tailless desmin (Bär et al., 2010), and vimentin (Lin et al., 2010a). These filaments form sticky contacts still strong enough to prevent equilibration of stretched filaments between contact points, but the tail domain seems to control the strain stiffening phenomenon and provides the stronger attraction necessary to withstand the large stresses networks are exposed to at large, non-linear deformations. The protein sequences providing these strong attractions are located in the tail domain.

The conclusions of the investigations conducted in this work are:

1. K8/K18 forms homogeneous networks with a mesh size, which can be well described by a cubic grid of rigid filaments, since the persistence length is on the order of the mesh size.
2. The high G_0 values at low concentration and the weak dependence of G_0 on protein concentration characteristic not only for keratin, but also for various other IF networks (Janmey et al., 1991; Ma et al., 1999; Schopferer et al., 2009) emerge from a strong entropic contribution of stretched filament strands between filament contact points to the free energy of the networks. This requires attractive interactions ($> k_B T$) at these contact points which are provided by the central rod domain of the protein.
3. K8/K18 networks regain their original viscoelastic properties after rupture.
4. A master curve obtained from the stiffening response of K8/K18 networks at different protein concentrations and different concentrations of $MgCl_2$ suggests a universal stiffening mechanism of a network with constant and finite strength of the

bonds between filaments. The strong attractive forces at filament contact points required for strain stiffening of IF networks are provided by the protein sequences located in the tail domain.

The formation of sticky contacts among filaments can be suppressed by adding a non-ionic surfactant to the network. Then strain stiffening vanishes and the concentration dependence of G_0 gets stronger. The corresponding scaling exponent is well captured by theoretical predictions for networks of semi-flexible or flexible polymers.

7 Zusammenfassung

Charakteristische mechanische Eigenschaften von Netzwerken aus Intermediärfilamenten (IFs) sind die ungewöhnlich hohen Elastizitäten bei geringen Deformationen, die nur geringfügig durch die Proteinkonzentration beeinflusst werden, sowie eine ausgeprägte Scherversteifung bei hohen Deformationen ohne dass zusätzliche Vernetzungsmoleküle benötigt werden. In dieser Studie werden die Ursachen für diese ungewöhnlichen Eigenschaften untersucht. Im Einzelnen werden die viskoelastischen Eigenschaften von IF Netzwerken aus den Proteinen Keratin (K8) und Keratin (K18) unter Standardbedingungen bei 10 mM Tris-HCl (pH 7.4), mit MgCl_2 oder mit dem nichtionischen Tensid Triton X-100 mittels Scherrheologie, oszillatorischer Quetschströmung und Mikrorheologie ausgiebig charakterisiert. Die Ergebnisse werden mit IF Netzwerken aus Mutanten von K8/K18 ohne N-terminale globuläre Endgruppe (K8 Δ T/K18 Δ T) und aus dem IF-Protein Vimentin verglichen. Zusätzlich werden verschiedene charakteristische Eigenschaften von K8/K18-Netzwerken untersucht. Zu diesen Charakteristika zählen die Kinetik der Netzwerkbildung, die Netzwerkstruktur, die Netzwerkhomogenität, das Verhalten von gerissenen Netzwerken, die Persistenzlänge der einzelnen Filamente und die Maschenweite.

Die Kinetik der Netzwerkbildung von K8/K18 Intermediärfilamenten wurde zunächst mit oszillationsrheologischen Methoden ermittelt. Experimente bei kleinen Deformationen im linear-viskoelastischen Bereich zeigen eine ähnlich Kinetik wie sie auch bei Vimentin und Desmin-Netzwerken beobachtet wurde (Schopferer et al., 2009). Die Netzwerke existieren bereits bei der Messung des ersten Datenpunktes nach einer Minute. Nach 20 Minuten hat der Speichermodul G' bereits 85% des endgültigen Wertes erreicht. Die Kinetik der Netzwerkbildung und die quantitativen Werte von G' wurden bei 20 °C und bei 37 °C untersucht. Beides ist temperaturunabhängig. Mikrorheologische Messungen zeigen eine ähnliche qualitative Veränderung der Moduli während der Netzwerkbildung wie scherrheologische Experimente.

Die Struktur der Netzwerke bei unterschiedlichen Proteinkonzentrationen und bei unterschiedlichen MgCl_2 -Konzentrationen wurde mittels Elektronenmikroskopie und mittels Multiple Particle Tracking (MPT) untersucht. Die Ergebnisse zeigen, dass die Maschenweite der Netzwerke ohne Salz gut durch ein kubisches Gitter aus starren Filamenten beschrieben werden kann. Folglich ist die Maschenweite ungefähr identisch mit der Konturlänge der Filamente zwischen benachbarten Vernetzungspunkten. Rasterelektronenmikroskopische Aufnahmen von K8/K18 Netzwerken bei einer Konzentration von 1.0 g/l zeigen viele bündelartige Strukturen. Die Homogenität der Netzwerke, die über MPT-Messungen ermittelt wurde, deutet daraufhin, dass es sich bei den Bündeln um Artefakte durch die Probenvorbereitung handelt. Im Gegensatz dazu bestätigen MPT-Experimente die Bündel, die in elektronenmikroskopischen Aufnahmen bei 1.5 mM MgCl_2 beobachtet wurden. Sedimentationsexperimente zeigen ebenfalls, dass mit steigender MgCl_2 -Konzentration ein zunehmender Anteil der Probe während der Zentrifugation sedimentiert. Die Zunahme schwerer und unlöslicher Bestandteile mit steigender MgCl_2 -Konzentration weist ebenfalls darauf hin, dass die Zugabe von MgCl_2 zur Bündelbildung führt.

In dieser Studie konnte durch die Variation der Messbedingungen gezeigt werden, dass die linearen und nicht linearen scherrheologischen Eigenschaften nicht durch Artefakte beeinflusst werden, die beispielsweise durch eine hohe Grenzflächenelastizität, Wandgleiten oder den Befüllungsprozess hervorgerufen werden.

Zur Charakterisierung der nichtlinearen rheologischen Eigenschaften wurden verschiedene Methoden genutzt. Der Methodenvergleich zeigt, dass sich die Messmethoden zur Bestimmung des differentiellen Modulus besser zur Charakterisierung der Scherversteifung eignen als Oszillationsversuche mit zunehmender Amplitude. Der differentielle Modul erlaubt eine einfache Dateninterpretation ohne eine Verfälschung der Ergebnisse durch eine aperiodische und nicht-sinusförmige Antwortfunktion. Der komplexe differentielle Modul kann durch die Überlagerung eines oszillatorischen Schubspannungssignals mit geringer Amplitude über eine konstante Schubspannung gemessen werden. Der entsprechende differentielle Speichermodul K' wird aus dem überlagerten

Oszillationssignal berechnet. Alternativ kann auch einfach die Schubspannungsantwort bei einer konstanten Schergeschwindigkeit ermittelt werden. Der differentielle Modul ist dann die Ableitung des Schubspannungssignals nach der Deformation $K = d\sigma/d\gamma$. Obwohl die Probe im ersten Versuchstypen stark kriecht, zeigen beide Messprotokolle ähnliche Ergebnisse.

In scherrheologischen Experimenten zeigen K8/K18-Netzwerke bereits bei einer Konzentration von 0.1 g/l vorwiegend elastische und frequenzunabhängige Eigenschaften mit einem ungewöhnlich hohen Plateaumodul G_0 . Der Plateaumodul hängt nur schwach von der Proteinkonzentration ab ($G_0 \sim c^{0.5}$). Die kritische Deformation γ_{crit} , ab der das nichtlineare Antwortsignal beginnt, ist unabhängig von der Proteinkonzentration. Beide Phänomene können dadurch erklärt werden, dass die Verknüpfungsdichte mit abnehmender IF Konzentration abnimmt ohne dass sich die Konturlänge des Filaments zwischen den Verknüpfungspunkten ändert. Die daraus resultierende gestreckte und thermodynamisch ungünstige Konformation der Filamente kompensiert teilweise die Abnahme in der freien Energie durch die Abnahme der Verknüpfungspunktdichte. Analog zu dieser Betrachtungsweise prognostiziert die Theorie für gequollene, quervernetzte Netzwerke aus flexiblen Filamenten in gutem Lösungsmittel das Potenzgesetz $G_0 \sim c^{0.58}$ (Obukhov et al., 1994), das sehr gut mit den Beobachtungen für IF-Netzwerke übereinstimmt.

Die Netzwerke reißen, wenn eine kritische Amplitude überschritten wird. Allerdings erholen sich die Netzwerke und weisen nach 30 Minuten die gleichen viskoelastischen Eigenschaften wie das ursprüngliche Netzwerk auf. Andere nichtlineare Eigenschafts-Parameter sind die Schubspannung bei der die Netzwerke reißen σ_{max} und der entsprechende Maximalwert des differentiellen Moduls K'_{max} . Beide Parameter zeigen einen starken Anstieg mit steigender Protein-Konzentration. Nach der Normalisierung von K' mit G_0 und der kontinuierlichen Schubspannung σ_0 mit der kritischen Schubspannung σ_{crit} bei der die nichtlineare Antwortfunktion einsetzt, fallen die Daten für unterschiedliche Protein-Konzentrationen alle auf einer Masterkurve zusammen. Dabei werden zwei unterschiedliche Regime $K' \sim \sigma_0^\alpha$ beobachtet, eines mit $\alpha \approx 1$ bei mittleren

Schubspannungen und mit $\alpha \approx 0.6$ bei hohen Schubspannungen. Die Exponenten sind geringer als der Wert $\alpha \approx 3/2$ für fest vernetzte Netzwerke aus semiflexiblen Filamenten. Der α -Wert kann im Rahmen des Glassy Wormlike Chain (GWLC) Modells unter der Annahme von reversiblen Bindungen zwischen den Filamenten mit konstanter und endlicher Bindungsenergie erklärt werden. Die Änderung der Steigung kann durch das Vorhandensein eines zweiten Bindungstyps oder die Dehnung einzelner Filamente hervorgerufen werden.

Der Plateaumodul G_0 wird nicht durch die MgCl_2 -Konzentration beeinflusst obwohl elektronenmikroskopische Aufnahmen auf eine Zunahme der Verknüpfungsdichte hindeuten. Diese kann damit erklärt werden, dass der Anstieg der Verknüpfungsdichte mit einem geringeren Anteil gestreckter Filamente einhergeht. Die Zunahme der Verknüpfungsdichte ist allerdings nicht stark genug um sich in einer Änderung von γ_{crit} niederzuschlagen. Im nichtlinearen Bereich steigt σ_{max} und K'_{max} stark mit zunehmender MgCl_2 -Konzentration an. Der Verlauf der Kurve ist identisch mit den Messungen ohne Salz. Ähnliche Ergebnisse wurden auch für den Einfluss divalenter Kationen auf Vimentin beobachtet (Lin et al., 2010a).

Der Einfluss des nichtionischen Tensids Triton X-100 auf die Eigenschaften von K8/K18-Netzwerken wurde zunächst mittels MPT, Hochfrequenzrheologie und Elektronenmikroskopie untersucht. Die Versuche zeigen, dass das Tensid keinen Einfluss auf die Homogenität, die Maschenweite, die Biegesteifigkeit und den Filamentdurchmesser hat. Auf der anderen Seite bewirkt das Tensid eine drastische Abnahme des Plateaumodulus bei scherrheologischen Messungen im linear viskoelastischen Bereich. Die absoluten Werte von G_0 und das Potenzgesetz $G_0 \sim c^x$ mit $x = 1.9 \pm 0.2$ können durch ein einfaches Modell beschrieben werden indem jeder Kontaktpunkt einen Energiebeitrag von $k_B T$ leistet und die Verknüpfungspunktdichte über die Längendichte von K8/K18-Filamenten unter Annahme eines kubischen Gitters berechnet wird ($x = 1.5$). Der Exponent des Potenzgesetzes für die Konzentrationsabhängigkeit des Plateaumodulus in Gegenwart von Triton X-100 ist auch im Bereich anderer theoretischer Modelle für Netzwerke aus flexiblen oder semi-flexiblen Filamenten ($1.4 \leq x \leq 2.5$). Dies kann

durch eine Abschwächung der hohen Bindungsenergie an den Filamentkontaktstellen erklärt werden, die die gestreckte Filamentkonformation hervorruft, welche für die hohen Moduli und die geringe Konzentrationsabhängigkeit ohne Triton X-100 verantwortlich ist. Die Zugabe des Tensids ermöglicht es den Filamenten zu equilibrieren und eine energieärmere Konformation einzunehmen.

Die scherrheologischen Daten mit Triton X-100 stimmen mit den Daten aus hochfrequenzrheologischen Messung mittel oszillatorischer Quetschströmung und den Daten aus mikrorheologischen Experimenten (Diffusing Wave Spectroscopy und MPT) überein. Dies ist das erste Mal das die Frequenzabhängigkeit der linear viskoelastischen Eigenschaften eines Intermediärfilament-Netzwerks über einen Frequenzbereich von 10^{-2} bis 10^6 rad/s charakterisiert werden konnte. Dabei wurden vier voneinander unabhängige Methoden genutzt. Die Persistenzlänge von K8/K18-Filamenten, die über die Messung der viskoelastischen Eigenschaften im Hochfrequenzbereich bestimmt wurden, liegt zwischen $l_p = 0.23$ und $0.65 \mu\text{m}$.

Die Moduli von K8 Δ T/K18 Δ T, Vimentin sowie von Desmin mit und ohne der N-terminalen Endgruppe (Bär et al., 2010) ähneln in ihren linearen viskoelastischen Eigenschaften dem Wildtyp von K8/K18. Dies zeigt, dass die attraktiven Wechselwirkungen, die das ungewöhnliche Verhalten von G_0 verursachen, durch hydrophobe Wechselwirkungen in der zentralen, α -helicalen und stäbchenförmigen Domäne hervorgerufen werden. Die Abschwächung der elastischen Eigenschaften durch Triton X-100 bei K8 Δ T/K18 Δ T und Vimentin ist stärker ausgeprägt als beim Wildtypen von K8/K18. Diese Beobachtung kann durch einen größeren Anteil von Filamentenden erklärt werden, die nichts zum Netzwerk beitragen. Ein anderer Erklärungsansatz ist eine stärkere elektrostatische Abstoßung zwischen K8 Δ T/K18 Δ T- und Vimentin-Filamenten, die ebenfalls zu einer Reduktion der Verknüpfungsdichte führt.

Wenn das Tensid im Nachhinein zum einem vollständig ausgebildeten Intermediärfilament-Netzwerk dazugegeben wird, sinkt der Plateaumodul G_0 ebenfalls. Der Absolutwert von G_0 nach Zugabe des Tensids ist jedoch höher als bei den Netzwerken die in Gegenwart des Tensids assembliert

wurden. Dieser Befund zeigt, dass das Tensid nicht alle Bindungen zwischen den Filamenten auflösen kann.

Im nächsten Schritt wurde die Scherversteifung von K8/K18, K8 Δ T/K18 Δ T und Vimentin mit und ohne Triton X-100 untersucht. Die Scherversteifung von K8/K18-Netzwerken ist stärker als bei Vimentin-Netzwerken. K8 Δ T/K18 Δ T bildet überwiegend elastische Netzwerke aus, zeigt allerdings keine Scherversteifung. Der Vergleich der Wildtypen mit Mutationen ohne die N-terminale globuläre Domäne der IF-Proteine Desmin (Bär et al., 2010) und Vimentin (Lin et al., 2010a) zeigt ein ähnliches Verhalten. Die Filamente ohne die N-terminale globuläre Proteindomäne bilden reversible Verknüpfungen deren Bindungsstärke ausreicht, dass viele Filamente in einer gestreckten Filamentkonformation vorliegen und sich kein Gleichgewicht einstellt. Die Bindungsstärke ohne die terminale globuläre Domäne ist jedoch offensichtlich nicht stark genug, um den Schubspannungen bei großen nicht-linearen Deformationen zu widerstehen. Die für die Scherversteifung verantwortliche Protein-Sequenz, die ausreichend starke attraktive Wechselwirkungen hervorruft befindet sich in der N-terminalen globulären Endgruppe.

Die Ergebnisse dieser Studie zeigen:

1. K8/K18 bilden homogene Netzwerke aus, deren Maschenweite durch ein kubisches Gitter aus starren Filamenten beschrieben werden kann.
2. Die hohen Werte für G_0 und die niedrige Konzentrationsabhängigkeit von G_0 sind charakteristische Eigenschaften von K8/K18, sowie Netzwerken aus anderen IF-Proteinen (Janmey et al., 1991; Ma et al., 1999; Schopferer et al., 2009), die durch einen starken entropischen Beitrag durch eine gestreckte Konformation der Filamente zwischen den Verknüpfungspunkten erklärt werden können. Die Ursache hierfür sind attraktive Wechselwirkungen, die durch die zentrale, α -helicale und stäbchenförmigen Domäne der Proteine hervorgerufen werden.
3. K8/K18-Netzwerke erholen sich nachdem die Netzwerke bei hohen Deformationen zerstört wurden und weisen nach einer

bestimmten Zeitspanne wieder ihre ursprünglichen viskoelastischen Eigenschaften auf.

4. Im nicht-linearen Bereich fallen die normalisierten Daten der differentiellen Moduli und des Schubspannungssignals, die bei unterschiedlichen K8/K18-Konzentrationen und bei unterschiedlichen Konzentrationen von MgCl_2 ermittelt wurden, auf einer Masterkurve zusammen. Die Ergebnisse deuten auf einen universellen Scherversteifungsmechanismus hin. Die starken attraktiven Wechselwirkungen zwischen den Filamenten, die die Scherversteifung hervorrufen, haben eine endliche und konstante Energie und werden durch die N-terminalen globulären Endgruppen der Proteine hervorgerufen.

Die reversiblen Bindungen zwischen den Filamenten können durch die Zugabe eines nicht-ionischen Tensids stark reduziert werden. Die Netzwerke zeigen in der Gegenwart des Tensids keine Scherversteifung. Im linearen Bereich sinkt G_0 und weist eine stärkere Konzentrationsabhängigkeit auf. Die Exponenten, welche die Konzentrationsabhängigkeit von G_0 beschreiben, können dann durch etablierte polymerphysikalische Theorien für semi-flexible oder flexible Polymeren beschrieben werden.

8 Appendix

8.1 Complementing experimental results

The network structure and the moduli can be derived from the MSD determined by microrheology. The resulting moduli can only be compared with the macroscopic viscoelastic properties if the particles are larger than the mesh size of the network and do not specifically interact with the protein filaments. In order to assess the interactions of the particles with the network, the averaged MSD from multiple particle tracking experiments with PEG coated PS particles was compared with experiments using unfunctionalized PS particles (Fig. 8.1). The results show no evidence for the influence of the particle surface on the resulting MSD.

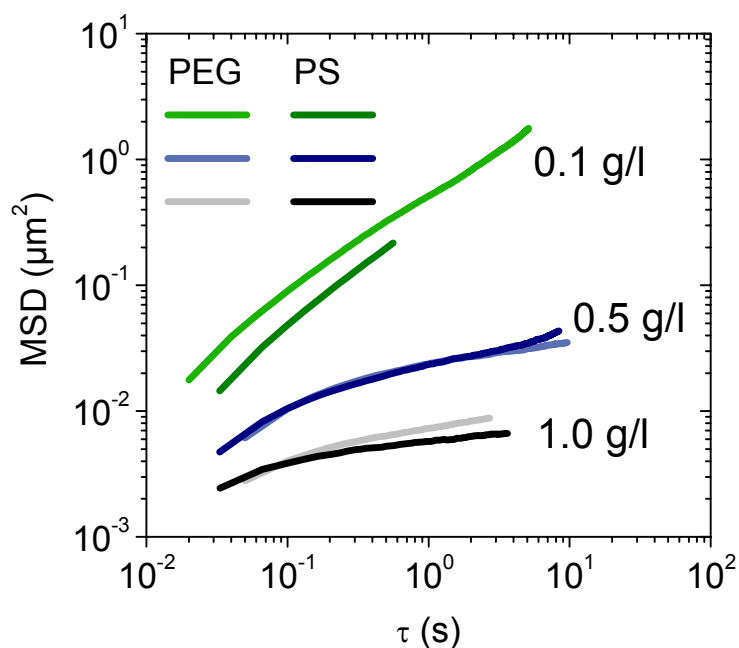


Fig. 8.1 Averaged MSD of particles coated with PEG and unfunctionalized PS particles with a diameter of $1.01 \mu\text{m}$ against lag time τ .

For diffusing wave spectroscopy sulfate functionalized particles were compared with unfunctionalized tracer particles (Fig. 8.2). The results clearly show higher moduli for the sulfate functionalized particles. This might originate from interactions between the particles and the filaments, which reduces the thermal motion of the particles. The PEG coated PS particles were chosen for all further experiments because the results agree well with data from MPT and high frequency oscillatory squeeze flow

measurements. These DWS measurements are not influenced by Triton X-100 (Fig. 8.3)

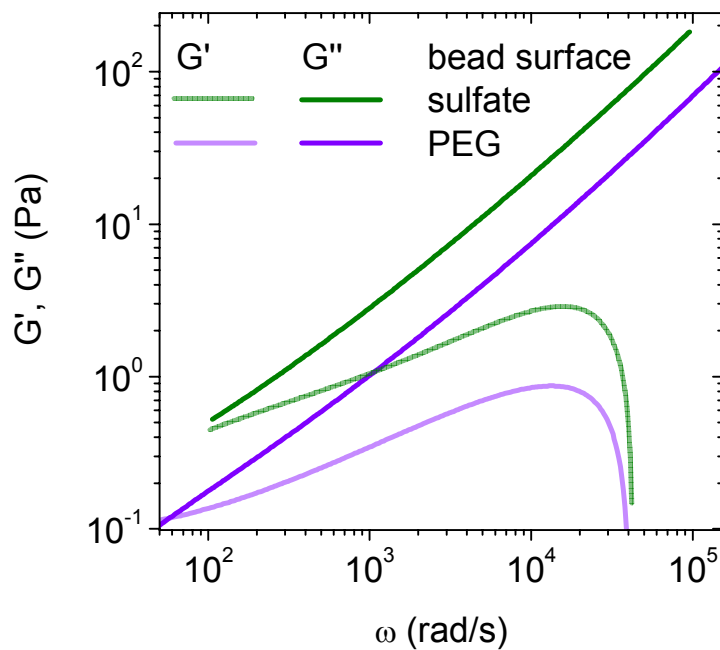


Fig. 8.2 Moduli from DWS with sulfate functionalized and PEG coated PS particles at a K8/K18 concentration of 0.5 g/l.

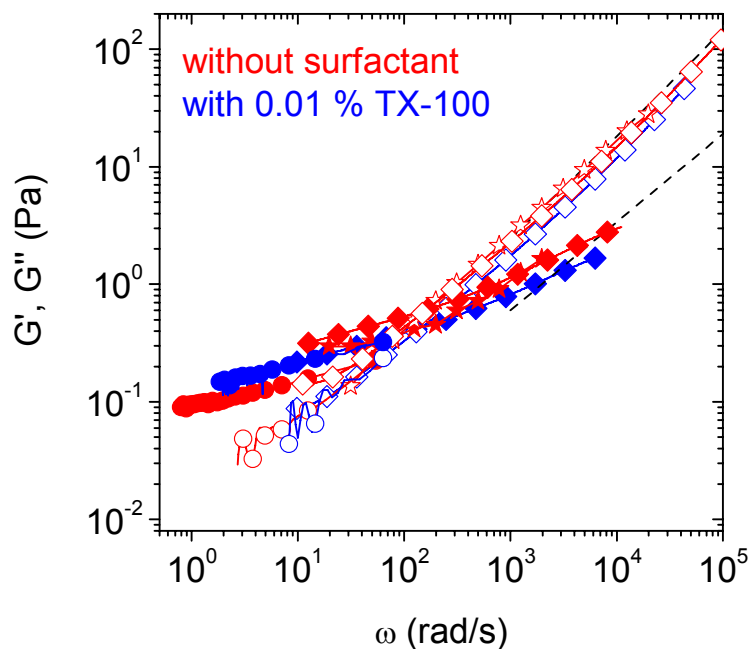


Fig. 8.3 G' (closed symbols) and G'' (open symbols) for K8/K18 networks without surfactant (red) and with 0.01 % TX-100 (blue) measured by MPT (circles) and DWS (diamonds). The K8/K18 concentration is 1.0 g/l.

8.2 List of symbols and abbreviations

Latin symbols:

a	Scaling exponent $G^* \sim \omega^a$
b	Monomer length, Kuhn length
c	Concentration
CMC	Critical micelle concentration
d	Tube diameter, gap width
DTT	Dithiothreitol
DWS	Diffusing wave spectroscopy
EDTA	Ethylenediaminetetraacetic acid
f	Free energy
F	Force
G	Shear modulus
G^*	Complex shear modulus
G'	Loss modulus
G''	Storage modulus
G_0	Plateau modulus
G'_M	Modulus at zero strain
G'_L	Modulus at the maximum strain
h	Gap width

ICF	Intensity correlation function
IF	Intermediate filaments
K	Differential modulus
K'	Differential storage modulus
K^*	Complex differential modulus
K5/K14	Keratin 5 and keratin 15
K8/K18	Keratin 8 and keratin 18
K8 Δ T/K18 Δ T	Tailless K8 and tailless K18
k_B	Boltzmann constant: $k_B = 1.3806 \cdot 10^{-23}$ J/K
L	Contour length
L_c	Contour length between adjacent cross-links
L_e	Contour length between adjacent entanglements
l_p	persistence length
L_x, L_y and L_z	Macroscopic dimensions of a cuboid
MPT	Multiple particle tracking
MSD	Mean square displacement
MT	Microtubules
MWCO	Molecular weight cut-off
N	Number of monomers per chain
n	Number of chains
NA	Numerical aperture

PEG	Polyethylene glycol
r	Particle radius
r_i	Bond vector
R	End-to-End vector of a polymer chain
S	Strain stiffening index
SDS	Sodium dodecyl sulfate
SDS-PAGE	SDS polyacrylamide gel electrophoresis
SEM	Scanning electron micrographs
T	Absolute temperature
TEM	Transmission electron micrographs
Tris	2-Amino-2-hydroxymethyl-propane-1,3-diol
U	Inner energy
ULF	Unit length filament
V	Volume
x	Scaling exponent $G_0 \sim c^x$

Greek symbols:

α	Scaling of K' with σ_0 ($K' \sim \sigma_0^\alpha$)
α_2	non-Gaussian parameter

γ	Deformation/shear
$\dot{\gamma}$	Shear rate
$\hat{\gamma}$	Strain amplitude
γ_{crit}	Strain at which the response signal becomes non-linear
γ_{max}	Strain at which the network ruptures
δ	Phase shift
ε	Stickiness parameter
η_s	Solvent viscosity
$ \eta^* $	Complex viscosity
$\kappa = k_B T l_p$	Bending stiffness
λ	Stretch factor, wavelength
λ_m	Mass per length
ν	Constraints per volume
ξ	Mesh size
ξ_b	Blob diameter
ρ	Polymer length density
σ	Shear stress
σ_0	Pre-stress
$\hat{\sigma}$	Stress amplitude
τ	Lag time
τ_e	Entanglement time
τ_R	Reptation time
ϕ	Volume fraction
ω	Angular frequency
ω_{rep}	Reptation frequency

9 References

- Apgar, J., Tseng, Y., Fedorov, E., Herwig, M.B., Almo, S.C., Wirtz, D., 2000. Multiple-particle tracking measurements of heterogeneities in solutions of actin filaments and actin bundles. *Biophys. J.* 79, 1095–1106.
- Bär, H., Schopferer, M., Sharma, S., Hochstein, B., Mücke, N., Herrmann, H., Willenbacher, N., 2010. Mutations in desmin’s carboxy-terminal “tail” domain severely modify filament and network mechanics. *J. Mol. Biol.* 397, 1188–1198.
- Bastide, J., Candau, S., Leibler, L., 1981. Osmotic deswelling of gels by polymer solutions. *Macromolecules* 719–726.
- Bousquet, O., Ma, L., Yamada, S., Gu, C., Idei, T., Takahashi, K., Wirtz, D., Coulombe, P.A., 2001. The nonhelical tail domain of keratin 14 promotes filament bundling and enhances the mechanical properties of keratin intermediate filaments in vitro. *J. Cell Biol.* 155, 747–754.
- Bradford, M.M., 1976. A rapid and sensitive method for the quantitation of microgram quantities of protein utilizing the principle of protein-dye binding. *Anal. Biochem.* 72, 248–254.
- Bräuchle, C., Lamb, D., Michaelis, J., 2009. Single particle tracking and single molecule energy transfer. Wiley-VCH Verlag GmbH & Co. KGaA, Weinheim, Germany.
- Broedersz, C.P., Depken, M., Yao, N.Y., Pollak, M.R., Weitz, D.A., MacKintosh, F.C., 2010a. Cross-link-governed dynamics of biopolymer networks. *Phys. Rev. Lett.* 105, 1–4.
- Broedersz, C.P., Kasza, K.E., Jawerth, L.M., Münster, S., Weitz, D.A., MacKintosh, F.C., 2010b. Measurement of nonlinear rheology of cross-linked biopolymer gels. *Soft Matter* 6, 4120–4127.
- Bustamante, C., Marko, J.F., Siggia, E.D., Smith, S., 1994. Entropic Elasticity of Lambda-Phage DNA. *Science.* 265, 5–6.

- Coulombe, P.A., Bousquet, O., Ma, L., Yamada, S., Wirtz, D., 2000. The “ins” and “outs” of intermediate filament organization. *Trends Cell Biol.* 10, 420–428.
- Crassous, J.J., Régisser, R., Ballauff, M., Willenbacher, N., 2005. Characterization of the viscoelastic behavior of complex fluids using the piezoelastic axial vibrator. *J. Rheol.* 49, 851–863.
- Crocker, J.C., Valentine, M.T., Weeks, E.R., Gisler, T., Kaplan, P.D., Yodh, a G., Weitz, D. a, 2000. Two-point microrheology of inhomogeneous soft materials. *Phys. Rev. Lett.* 85, 888–891.
- Daoud, M., Cotton, J.P., Farnoux, B., Jannink, G., Sarma, G., Benoit, H., Duplessix, Picot, C., de Gennes, P.-G., 1975. Solutions of flexible polymers. Neutron experiments and interpretation. *Macromolecules* 589, 804–818.
- De Gennes, P.-G., 1979. *Scaling concepts in polymer physics*. Cornell Univ. Pr., Ithaca.
- Doi, M., Edwards, S., 1996. *Introduction to Polymer Physics*. Oxford University Press, USA.
- Edwards, S., 1967. The statistical mechanics of polymerized material. *Proc. Phys. Soc.* 92, 9.
- Ewoldt, R.H., Hosoi, A.E., McKinley, G.H., 2008. New measures for characterizing nonlinear viscoelasticity in large amplitude oscillatory shear. *J. Rheol.* 52, 1427–1458.
- Gardel, M.L., Nakamura, F., Hartwig, J.H., Crocker, J.C., Stossel, T.P., Weitz, D.A., 2006. Prestressed F-actin networks cross-linked by hinged filamins replicate mechanical properties of cells. *Proc. Natl. Acad. Sci. U. S. A.* 103, 1762–1767.
- Gardel, M.L., Shin, J.H., MacKintosh, F.C., Mahadevan, L., Matsudaira, P., Weitz, D.A., 2004a. Elastic behavior of cross-linked and bundled actin networks. *Science.* 304, 1301–1305.

- Gardel, M.L., Shin, J.H., MacKintosh, F.C., Mahadevan, L., Matsudaira, P., Weitz, D.A., 2004b. Scaling of F-actin network rheology to probe single filament elasticity and dynamics. *Phys. Rev. Lett.* 93, 188102.
- Gardel, M.L., Valentine, M.T., Crocker, J.C., Bausch, A.R., Weitz, D.A., 2003. Microrheology of entangled F-actin solutions. *Phys. Rev. Lett.* 91, 158302.
- Gittes, F., MacKintosh, F.C., 1998. Dynamic shear modulus of a semiflexible polymer network. *Phys. Rev. E* 58, R1241–R1244.
- Gittes, F., Mickey, B., Nettleton, J., Howard, J., 1993. Flexural rigidity of microtubules and actin filaments measured from thermal fluctuations in shape. *J. Cell Biol.* 120, 923–934.
- Gittes, F., Schnurr, B., Olmsted, P., MacKintosh, F.C., Schmidt, C.F., 1997. Microscopic viscoelasticity: shear moduli of soft materials determined from thermal fluctuations. *Phys. Rev. Lett.* 17, 3286–3289.
- Hatzfeld, M., Weber, K., 1990. Tailless keratins assemble into regular intermediate filaments in vitro. *J. Cell Sci.* 97, 317–324.
- Herrmann, H., Aebi, U., 1998. Intermediate filament assembly: fibrillogenesis is driven by decisive dimer-dimer interactions. *Curr. Opin. Struct. Biol.* 8, 177–85.
- Herrmann, H., Aebi, U., 2004. Intermediate filaments: molecular structure, assembly mechanism, and integration into functionally distinct intracellular Scaffolds. *Annu. Rev. Biochem.* 73, 749–789.
- Herrmann, H., Bär, H., Kreplak, L., Strelkov, S. V., Aebi, U., 2007. Intermediate filaments: from cell architecture to nanomechanics. *Nat. Rev. Mol. Cell Biol.* 8, 562–573.
- Herrmann, H., Häner, M., Brettel, M., Ku, N.-O., Aebi, U., 1999. Characterization of distinct early assembly units of different intermediate filament proteins. *J. Mol. Biol.* 286, 1403–1420.

- Herrmann, H., Hofmann, I., Franke, W.W., 1992. Identification of a nonapeptide motif in the vimentin head domain involved in intermediate filament assembly. *J. Mol. Biol.* 223, 637–650.
- Herrmann, H., Strelkov, S. V, Burkhard, P., Aebi, U., 2009. Intermediate filaments: primary determinants of cell architecture and plasticity. *J. Clin. Invest.* 119, 1772–1783.
- Hinner, B., Tempel, M., Sackmann, E., Kroy, K., Frey, E., 1998. Entanglement, elasticity, and viscous relaxation of actin solutions. *Phys. Rev. Lett.* 81, 2614–2617.
- Hofmann, I., Franke, W.W., 1997. Heterotypic interactions and filament assembly of type I and type II cytokeratins in vitro: viscometry and determinations of relative affinities. *Eur. J. Cell Biol.* 72, 122–132.
- Ilavský, M., Bouchal, K., Dušek, K., 1989. Effect of dilution during network formation on the sol fraction and elasticity of polyurethane networks. *Die Makromol. Chemie* 891, 883–891.
- Isambert, H., Maggs, A.C., 1996. Dynamics and rheology of actin solutions. *Macromolecules* 29, 1036–1040.
- James, H.M., Guth, E., 1943. Theory of the Elastic Properties of Rubber. *J. Chem. Phys.* 11, 455–481.
- Janmey, P.A., Euteneuer, U., Traub, P., Schliwa, M., 1991. Viscoelastic properties of vimentin compared with other filamentous biopolymer networks. *J. Cell Biol.* 113, 155–160.
- Käs, J., Strey, H., Tang, J.X., Finger, D., Ezzell, R., Sackmann, E., Janmey, P.A., 1996. F-actin, a model polymer for semiflexible chains in dilute, semidilute, and liquid crystalline solutions. *Biophys. J.* 70, 609–625.
- Kasza, K.E., Koenderink, G.H., Lin, Y.-C., Broedersz, C.P., Messner, W., Nakamura, F., Stossel, T.P., MacKintosh, F.C., Weitz, D.A., 2009. Nonlinear elasticity of stiff biopolymers connected by flexible linkers. *Phys. Rev. E* 79, 041928.

- Kasza, K.E., Rowat, A.C., Liu, J., Angelini, T.E., Brangwynne, C.P., Koenderink, G.H., Weitz, D.A., 2007. The cell as a material. *Curr. Opin. Cell Biol.* 19, 101–107.
- Kayser, J., Grabmayr, H., Harasim, M., Herrmann, H., Bausch, A.R., 2012. Assembly kinetics determine the structure of keratin networks. *Soft Matter* 8, 8873–8879.
- Kegel, W.K., van Blaaderen, A., 2000. Direct observation of dynamical heterogeneities in colloidal hard-sphere suspensions. *Science* (80-.). 287, 290–293.
- Kim, A.J., Manoharan, V.N., Crocker, J.C., 2005. Swelling-based method for preparing stable, functionalized polymer colloids. *J. Am. Chem. Soc.* 127, 1592–1593.
- Kirmse, R., Bouchet-Marquis, C., Page, C., Hoenger, A., 2010. Three-dimensional cryo-electron microscopy on intermediate filaments. *Methods Cell Biol.* 96, 565–589.
- Kirmse, R., Portet, S., Mu, N., Aebi, U., Herrmann, H., Mücke, N., Langowski, J., 2007. A quantitative kinetic model for the in vitro assembly of intermediate filaments from tetrameric vimentin. *J. Biol. Chem.* 282, 18563–18572.
- Köster, S., Lin, Y.-C., Herrmann, H., Weitz, D.A., 2010. Nanomechanics of vimentin intermediate filament networks. *Soft Matter* 6, 1910–1914.
- Kreplak, L., Bär, H., Leterrier, J.-F., Herrmann, H., Aebi, U., 2005. Exploring the mechanical behavior of single intermediate filaments. *J. Mol. Biol.* 354, 569–577.
- Kroy, K., Frey, E., 1996. Force-extension relation and plateau modulus for wormlike chains. *Phys. Rev. Lett.* 77, 306–309.
- Kroy, K., Glaser, J., 2007. The glassy wormlike chain. *New J. Phys.* 9, 416–416.

- Kyte, J., Doolittle, R.F., 1982. A simple method for displaying the hydrophobic character of a protein. *J. Mol. Biol.* 157, 105–132.
- Laemmli, U., 1970. Cleavage of structural proteins during the assembly of the head of bacteriophage T4. *Nature* 227, 680–685.
- Leitner, A., Paust, T., Marti, O., Walther, P., Herrmann, H., Beil, M., 2012. Properties of intermediate filament networks assembled from keratin 8 and 18 in the presence of Mg²⁺. *Biophys. J.* 103, 195–201.
- Lichtenstern, T., Mücke, N., Aebi, U., Mauermann, M., Herrmann, H., 2012. Complex formation and kinetics of filament assembly exhibited by the simple epithelial keratins K8 and K18. *J. Struct. Biol.* 177, 54–62.
- Lieleg, O., Bausch, A.R., 2007. Cross-linker unbinding and self-similarity in bundled cytoskeletal networks. *Phys. Rev. Lett.* 99, 158105.
- Lin, Y.-C., Broedersz, C.P., Rowat, A.C., Wedig, T., Herrmann, H., MacKintosh, F.C., Weitz, D.A., 2010a. Divalent cations crosslink vimentin intermediate filament tail domains to regulate network mechanics. *J. Mol. Biol.* 399, 637–644.
- Lin, Y.-C., Yao, N.Y., Broedersz, C.P., Herrmann, H., MacKintosh, F.C., Weitz, D.A., 2010b. Origins of elasticity in intermediate filament networks. *Phys. Rev. Lett.* 104, 058101.
- Ma, L., Xu, J., Coulombe, P.A., Wirtz, D., 1999. Keratin filament suspensions show unique micromechanical properties. *J. Biol. Chem.* 274, 19145–19151.
- Ma, L., Yamada, S., Wirtz, D., Coulombe, P.A., 2001. A “hot-spot” mutation alters the mechanical properties of keratin filament networks. *Nat. Cell Biol.* 3, 503–506.
- MacKintosh, F.C., Käs, J., Janmey, P.A., 1995. Elasticity of semiflexible biopolymer networks. *Phys. Rev. Lett.* 75, 4425–4428.

- Mason, T.G., Dhople, A., Wirtz, D., 1998. Linear viscoelastic moduli of concentrated DNA solutions. *Macromolecules* 31, 3600–3603.
- Mason, T.G., Ganesan, K., van Zanten, J., Wirtz, D., Kuo, S., 1997. Particle tracking microrheology of complex fluids. *Phys. Rev. Lett.* 79, 3282–3285.
- Mason, T.G., Weitz, D.A., 1995. Optical measurements of frequency-dependent linear viscoelastic moduli of complex fluids. *Phys. Rev. Lett.* 74, 1250–1253.
- Morse, D.C., 1998. Viscoelasticity of concentrated isotropic solutions of semiflexible polymers. 2. Linear response. *Macromolecules* 9297, 7044–7067.
- Mücke, N., Kreplak, L., Kirmse, R., Wedig, T., Herrmann, H., Aebi, U., Langowski, J., 2004. Assessing the flexibility of intermediate filaments by atomic force microscopy. *J. Mol. Biol.* 335, 1241–1250.
- Obukhov, S.P., Rubinstein, M., Colby, R.H., 1994. Network modulus and superelasticity. *Macromolecules* 27, 3191–3198.
- Odijk, T., 1983. On the statistics and dynamics of confined or entangled stiff polymers. *Macromolecules* 16, 1340–1344.
- Oelschlaeger, C., Schopferer, M., Scheffold, F., Willenbacher, N., 2009. Linear-to-branched micelles transition: a rheometry and diffusing wave spectroscopy (DWS) study. *Langmuir* 25, 716–723.
- Omary, M.B., 2009. “IF-pathies”: a broad spectrum of intermediate filament – associated diseases. *J. Clin. Invest.* 119, 1756–1762.
- Omary, M.B., Ku, N.-O., Tao, G.-Z., Toivola, D.M., Liao, J., 2006. “Heads and tails” of intermediate filament phosphorylation: multiple sites and functional insights. *Trends Biochem. Sci.* 31, 383–394.

- Oppong, F., Rubatat, L., Frisken, B., Bailey, A., de Bruyn, J., 2006. Microrheology and structure of a yield-stress polymer gel. *Phys. Rev. E* 73, 041405.
- Pearson, D., 1987. Recent advances in the molecular aspects of polymer viscoelasticity. *Rubber Chem. Technol.* 60, 439–496.
- Portet, S., Mücke, N., Kirmse, R., Langowski, J., Beil, M., Herrmann, H., 2009. Vimentin Intermediate Filament Formation: In Vitro Measurement and Mathematical Modeling of the Filament Length Distribution during Assembly. *Langmuir* 25, 8817–8823.
- Raghavan, S.R., Douglas, J.F., 2012. The conundrum of gel formation by molecular nanofibers, wormlike micelles, and filamentous proteins: gelation without cross-links? *Soft Matter* 8, 8539–8546.
- Ramaekers, F.C.S., Bosman, F.T., 2004. The cytoskeleton and disease. *J. Pathol.* 204, 351–354.
- Rammensee, S., Janmey, P.A., Bausch, A.R., 2007. Mechanical and structural properties of in vitro neurofilament hydrogels. *Eur. Biophys. J.* 36, 661–668.
- Savin, T., Doyle, P.S., 2005. Static and dynamic errors in particle tracking microrheology. *Biophys. J.* 88, 623–638.
- Schnurr, B., Gittes, F., MacKintosh, F.C., Schmidt, C.F., 1997. Determining microscopic viscoelasticity in flexible and semiflexible polymer networks from thermal fluctuations. *Macromolecules* 30, 7781–7792.
- Schopferer, M., 2010. Rheologische Charakterisierung polymerer Netzwerke mittels mechanischer Hochfrequenzmethoden. Karlsruhe Institute of Technology (KIT).
- Schopferer, M., Bär, H., Hochstein, B., Sharma, S., Mücke, N., Herrmann, H., Willenbacher, N., 2009. Desmin and vimentin intermediate

- filament networks: their viscoelastic properties investigated by mechanical rheometry. *J. Mol. Biol.* 388, 133–143.
- Schweizer, J., Bowden, P.E., Coulombe, P. a, Langbein, L., Lane, E.B., Magin, T.M., Maltais, L., Omary, M.B., Parry, D. a D., Rogers, M. a, Wright, M.W., 2006. New consensus nomenclature for mammalian keratins. *J. Cell Biol.* 174, 169–174.
- scopus, 2013. Elsevier [WWW Document]. Elsevier. URL <http://www.scopus.com> (accessed 8.30.13).
- Semmrich, C., Larsen, R.J., Bausch, A.R., 2008. Nonlinear mechanics of entangled F-actin solutions. *Soft Matter* 4, 1675–1680.
- Semmrich, C., Storz, T., Glaser, J., Merkel, R., Bausch, A.R., Kroy, K., 2007. Glass transition and rheological redundancy in F-actin solutions. *Proc. Natl. Acad. Sci. U. S. A.* 104, 20199–20203.
- Shin, J.H., Gardel, M.L., Mahadevan, L., Matsudaira, P., Weitz, D.A., 2004. Relating microstructure to rheology of a bundled and cross-linked F-actin network in vitro. *Proc. Natl. Acad. Sci. U. S. A.* 101, 9636–9641.
- Smith, E.A., Fuchs, E., 1998. Defining the interactions between intermediate filaments and desmosomes. *J. Cell Biol.* 141, 1229–1241.
- Steinböck, F.A., Wiche, G., 1999. Plectin: A cytolinker by design. *Biol. Chem.* 380, 151–158.
- Steinert, P.M., Idler, W.W., Zimmerman, S.B., 1976. Self-assembly of bovine epidermal keratin filaments in vitro. *J. Mol. Biol.* 108, 547–567.
- Steinmetz, M.O., Stoffler, D., Müller, S.A., Jahn, W., Wolpensinger, B., Goldie, K.N., Engel, A., Faulstich, H., Aebi, U., 1998. Evaluating atomic models of F-actin with an undecagold-tagged phalloidin derivative. *J. Mol. Biol.* 276, 1–6.

- Storm, C., Pastore, J.J., MacKintosh, F.C., Lubensky, T.C., Janmey, P.A., 2005. Nonlinear elasticity in biological gels. *Nature* 435, 191–194.
- Szeverenyi, I., Cassidy, A.J., Chung, C.W., Lee, B.T.K., Common, J.E. a, Ogg, S.C., Chen, H., Sim, S.Y., Goh, W.L.P., Ng, K.W., Simpson, J. a, Chee, L.L., Eng, G.H., Li, B., Lunny, D.P., Chuon, D., Venkatesh, A., Khoo, K.H., McLean, W.H.I., Lim, Y.P., Lane, E.B., 2008. The Human Intermediate Filament Database: comprehensive information on a gene family involved in many human diseases. *Hum. Mutat.* 29, 351–360.
- Tharman, R., Claessens, M.M.A.E., Bausch, A.R., 2007. Viscoelasticity of isotropically cross-linked actin networks. *Phys. Rev. Lett.* 98, 088103.
- Tiller, G.E., Mueller, T.J., Dockter, M.E., Struve, W.G., 1984. Hydrogenation of Triton X-100 eliminates its fluorescence and ultraviolet light absorption while preserving its detergent properties. *Anal. Biochem.* 141, 262–266.
- Treloar, L.R.G., 2009. *The physics of rubber elasticity*, 3. ed., re. ed. Clarendon Pr., Oxford.
- Tseng, Y., Wirtz, D., 2001. Mechanics and multiple-particle tracking microheterogeneity of alpha-actinin-cross-linked actin filament networks. *Biophys. J.* 81, 1643–1656.
- Valentine, M.T., Kaplan, P., Thota, D., Crocker, J.C., Gisler, T., Prud'homme, R.K., Beck, M., Weitz, D.A., 2001. Investigating the microenvironments of inhomogeneous soft materials with multiple particle tracking. *Phys. Rev. E* 64, 15–17.
- Wagner, O.I., Rammensee, S., Korde, N., Wen, Q., Leterrier, J.-F., Janmey, P.A., 2007. Softness, strength and self-repair in intermediate filament networks. *Exp. Cell Res.* 313, 2228–2235.
- Weeds, A., 1982. Actin-binding proteins—regulators of cell architecture and motility. *Nature* 296, 811–815.

- Wen, Q., Janmey, P.A., 2011. Polymer physics of the cytoskeleton. *Curr. Opin. Solid State Mater. Sci.* 15, 177–182.
- Willenbacher, N., Oelschlaeger, C., Schopferer, M., Fischer, P., Cardinaux, F., Scheffold, F., 2007. Broad Bandwidth Optical and Mechanical Rheometry of Wormlike Micelle Solutions. *Phys. Rev. Lett.* 99, 068302.
- Winheim, S., Hieb, A.R., Silbermann, M., Surmann, E.-M., Wedig, T., Herrmann, H., Langowski, J., Mücke, N., 2011. Deconstructing the Late Phase of Vimentin Assembly by Total Internal Reflection Fluorescence Microscopy (TIRFM). *PLoS One* 6, e19202.
- Wolff, L., Fernández, P., Kroy, K., 2010. Inelastic mechanics of sticky biopolymer networks. *New J. Phys.* 12, 053024.
- Yamada, S., Wirtz, D., Coulombe, P.A., 2002. Pairwise assembly determines the intrinsic potential for self-organization and mechanical properties of keratin filaments. *Mol. Biol. Cell* 13, 382–391.
- Yamada, S., Wirtz, D., Coulombe, P.A., 2003. The mechanical properties of simple epithelial keratins 8 and 18: discriminating between interfacial and bulk elasticities. *J. Struct. Biol.* 143, 45–55.

10 Curriculum Vitae

Name: Paul Pawelzyk

Date of Birth: 13.12.1981

Place of Birth: Schwalbach (Saar)

10/2001 – 06/2006 University Hamburg
Chemistry
Thesis: Stability and flow properties of disperse mixtures of aqueous carboxymethyl cellulose and caseinate solutions.

04/2005 – 09/2005 University of Southampton (UK)
Erasmus scholarship

10/2006 – 09/2008 University of Kiel,
Diploma studies in business chemistry
(Dipl.-Wirtschaftschemie)
Thesis: Management of idiosyncratic resources in cooperations between competitors.

04/2009 – 08/2010 Karlsruhe Institute of Technology (KIT)
Postgraduate studies in chemical engineering
Final paper: Analysis of the swelling behavior of polystyrene latexes by ultrasonic absorption.

04/2010 – 09/2013 Karlsruhe Institute of Technology (KIT)
Research associate at the Applied Mechanics Group (AME) at the Institute for Mechanical Process Engineering and Mechanics (MVM)

11 Publications

- P. Pawelzyk, N. Mücke, H. Herrmann and N. Willenbacher 2014.
Attractive interactions among intermediate filaments regulate network mechanics in vitro. PLOS ONE, 10.1371/journal.pone.0093194.
- P. Pawelzyk, H. Herrmann and N. Willenbacher 2013. Mechanics of intermediate filament networks assembled from keratins K8 and K18. *Soft Matter*, 9, 8871-8880.
- P. Pawelzyk, M. L. Toledo and N. Willenbacher 2013. Ultrasonic in-line monitoring of styrene miniemulsion polymerization. *Chem. Eng. J.*, 219, 303-310.
- W. Levason, J. M. Manning, P. Pawelzyk and G. Reid 2006. Synthesis and Properties of Organometallic PtII and PtIV Complexes with cyclic Selenoether and Telluroether Ligands and Selenoether Macrocycles. *Eur. J. Inorg. Chem.*, 21, 4380–4390.

12 Conferences

Presentations:

- International Congress on Rheology, August 2012, Lissabon, Portugal.
- Spring Meeting of the Condensed Matter Section of the DPG, March 2012, Berlin.
- Annual European Rheology Conference, April 2013, Leuven, Belgien.

Posters:

- European Conference on Intermediate Filaments in Health and Disease, Juni 2011, Mykonos, Griechenland.
- Gordon Conference on Intermediate Filaments, Juni 2012, Lewiston, Maine, USA.